RAM ROBOTICS AND MECHATRONICS

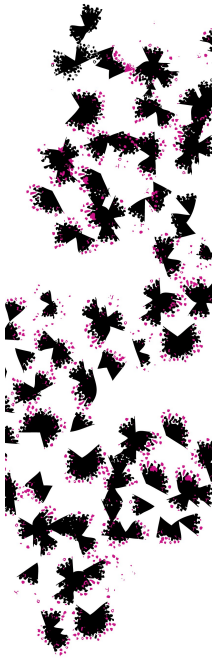

Towards additively manufactured complex robotic systems

M. (Martijn) Schouten

MSc Report

Committee:
Prof.dr.ir. G.J.M. Krijnen
Ing. R.G.P. Sanders
Dr.ir. W. Olthuis
Dr.ir. E.C. Dertien

December 2017

052RAM2017
Robotics and Mechatronics
EE-Math-CS
University of Twente
P.O. Box 217
7500 AE Enschede
The Netherlands

UNIVERSITY OF TWENTE.

MIRA CTIT
BIOMEDICAL TECHNOLOGY AND TECHNICAL MEDICINE

Samenvatting

In deze studie word gepoogd om een stapje te maken in de ontwikkeling van een nieuw fabricage proces voor robotische systemen. In het beoogde fabricage proces wordt het volledige robotische systeem, inclusief actuatoren en sensoren, in een keer geprint.

Terwijl de eerste 3D geprinte sensoren nog maar net zijn gepubliceerd, zal dit werk zich focussen op de ontwikkeling van geprinte actuatoren. Het doel is om te werken naar een actuator die een vergelijkbare rek, energie dichtheid en frequentie heeft als een menselijke spier. Maar het zal blijken dat dit bij lange na nog niet is gehaald.

Het type actuator dat in dit werk gefabriceerd wordt is een diëlektrische elastomeer actuator. Dit is een elektrostatische actuator die bestaat uit dunne lagen van flexibel elektrisch isolerend materiaal tussen twee dunne lagen van een zacht geleidend materiaal.

In de studie wordt gedemonstreerd hoe de te verwachte prestatie van een diëlektrische elastomeer, die geprint kan worden met een standaard consumenten 3D printer, kan worden verbeterd door gebruik te maken van een weekmaker met een hoge diëlektrische constante. Nadeel van deze weekmaker is dat hij niet compatibel is met het op dit moment gebruikte flexibele geleidende filament.

Tot slot, is een actuator gedemonstreerd die in staat is om een strookje materiaal in oscillatie te brengen. Deze oscillatie had een uitwijking van 1.8 µm.

Summary

In this study an attempt is made to make progress towards a new way of fabricating robotic systems. The envisioned fabrication process consist of additive manufacturing of the entire robotic system, including actuators and sensors, in one go.

While the first 3D printed sensors have been published only just recently, this work focuses on the development of printed actuators. The aim is to work towards an actuator that is similar to a human muscle in strain, energy density and operating frequency. However this is something that currently has not yet been achieved.

The type of actuator that is fabricated in this work is a Dielectric Elastomer Actuator. Which is an electrostatic actuator that consists of a thin layer of soft electrically isolating material in between two thin layers of soft conductive material.

It is demonstrated how the expected performance of a dielectric that can be printed using a consumer grade fused deposition modelling 3D printer, can be increased by using a plasticizer with a high dielectric constant. However this plasticizer is incompatible with the currently available flexible conductive filament.

Furthermore, as a proof of concept, an actuator has been fabricated that has shown to be able to bring a cantilever into oscillation. The resulting oscillation showed a deflection of 1.8 µm.

Contents

1 Introduction

This report describes the work done by Martijn Schouten for the final assignment of his master. The goal of the assignment is to 3D print an actuator. The assignment consists of the analysis of different materials, fabrication processes and device designs that can be used to do so. The most interesting of these materials, fabrication processes and designs will be realised and characterised.

1.1 Context

At the moment robotic systems consist of rotary motors with gearboxes that are coupled to hard metal or hard plastic parts. The cost of these robotic systems increases with their complexity and their appearance is very unnatural.

This is a problem in for example bio-mimetic robotics and even more for prosthetics, since these systems require a large number of actuators and sensors and have to appear as natural as possible.

Currently 3D printing processes such as fused deposition and poly jetting are rapidly gaining in maturity. 3D printing allows the production of highly complex systems without increasing their cost and would therefore be suitable for the fabrication of robots with a high complexity.

Printing robotic systems however requires actuators that can be printed. Currently pneumatic actuators already can be 3D printed, however a complex robotic system based on pneumatic actuators would require a large number of pumps or valves, which cannot be printed. On the other hand electrical valves, transistor, already have been printed (Ghaffarzadeh, 2017). A complex robotic system based on electrical actuators therefore might be relatively easily controlled.

1.2 Related work

Risner (2008) looked into the use of Dielectric Elastomer Actuators for printed robotics, by printing support frames for Dielectric Elastomer materials. Coulter (2011) examined the use of artificial muscles as a face muscle protesis. He fabricated an Ionic-polymer metal composite actuator.

Except from the research on printed actuators, there has been a lot of research done on artificial muscles. Furthermore sometimes energy storage systems suffer from an unintentional coupling to the mechanical domain. A more in depth discussion of the available literature can be found in section 2.

1.3 Project goal

The goal of the project is to develop an actuator with the same performance as a human muscle and that can be used in large numbers in complex robotic systems.

1.4 Requirements

The goal that is described above can be translated into the following requirements:

- To make an actuator with a performance that is similar to a human skeletal muscle it should have a power density, energy density and a maximum strain that is comparable. Therefore this research will aim for an actuator with a work density of $8\,\mathrm{kJ\,m^{-3}}$, a strain of 20 % (Mirfakhrai et al., 2007) and an operating frequency range of 0-1 Hz (see section 2 for a more elaborate definition of work density, strain and operating frequency)

- The control of a complex robotics system with many actuators can be a challenging task. However over the past decades much work has been done on the development of electrical control systems and there also has been research done on printing of the most important component of these systems, the transistor (Ghaffarzadeh, 2017). Therefore to make it possible for the actuator to benefit from this knowledge it is required that it can be actuated with an electrical signal.

- From an ethical point of view, it is important that nobody dies by using the actuator. Furthermore for the acceptance of the device it is important that it is not more dangerous as components that are already available in households. The maximum voltage that can be used is therefore set to a 300 V peak voltage for high power AC signals, which similar to the mains voltage in Europe. Furthermore a voltage of 1 kV will be allowed for low power DC signals. The maximum charge that may be stored at voltages above 300 V is set to 25 µC. This is similar to an electric fly swatter. These requirements will also will help to keep the actuation electronics of the muscle small and low cost. The safety argument also restricts the use of chemicals which are likely to cause serious injuries.

- To make sure that the actuator can be used to manufacture complex robotic structures the muscle has to be printable. In this work this will be interpreted as the requirement that the actuator should consist of materials that currently can be printed. It is not required that all materials can be printed currently in the same 3D printer, since it is expected that there soon will be systems available that will combine different printing techniques (Refle, 2017).

- An actuators used in a biometic application should have a weight similar to human muscles. Therefore the cost of materials and techniques per unit weight required to fabricate the actuator should be of such an order that fabrication of an entire muscle is still economically feasible. In this research the aim is to fabricate an actuator below 1 €/g.

1.5 Approach

The challenge of designing the printed actuator will be tackled by using a combination of the engineering and the scientific approach. First the engineering approach will be used to identify the limits of the current state of technology. Next the scientific approach will be used to broaden these limits. This in order to attempt to combine the creativity resulting from the scientific approach with the efficiency of the engineering approach.

1.6 Definitions

When describing the different print directions the coordinate system as shown in figure 1.1 will be used.

1.7 Report structure

Chapter 2 will discuss several concepts of a printed actuator. Chapter 3 will discuss the design of an actuator based on the most promising concept. Chapter 4 discusses the implementation of this design. In Chapter 5 the measurements performed on this actuator will be discussed and in Chapter 6 the results of these measurements are discussed. Chapter 7 concludes the report.

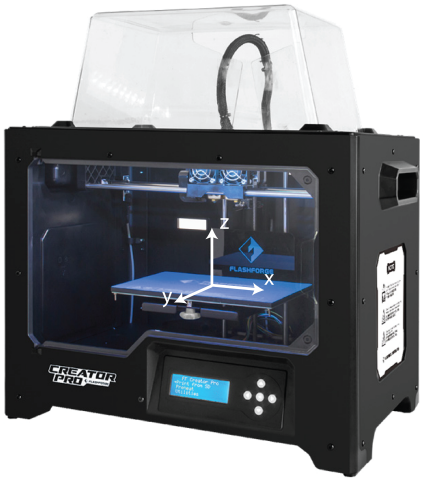

Figure 1.1: The used coordinate system

2 Conceptual design

2.1 Introduction

As described in Section 1.4 the actuator will be designed to have a minimum work density, operating frequency and strain of respectively 8 kJ m^{-3}, 0-1Hz and 20 %. In this section various concepts for 3D printed actuators will be evaluated.

Work density is defined as the amount of work per unit volume that can be extracted from a single stroke. For piezoelectric and dielectric elastomer actuators often the work done in elastically deforming the actuator material is given (Mirfakhrai et al., 2007)

$$W_{\mathrm{d}} = \frac{1}{2} Y \epsilon^2 \tag{2.1}$$

Where ϵ is the strain and Y is the Young's modulus of the material. This is equivalent to the total amount of energy in the form of heat that would have been produced when a very stiff damper would have been connected to the actuator. For a linear elastic material the previous equation is equivalent to:

$$W_{\mathrm{d}} = \frac{1}{2} \sigma \epsilon \tag{2.2}$$

Where σ is the stress exerted on the material by the actuator. Note that the strain, operating frequency and energy density can be changed by including mechanical amplification or a stepping mechanism in the design of the actuator. Both however introduce additional design challenges and constraints, making the design of complex robotic systems with many actuators, even more challenging than it already is. The possibility of using these techniques will therefore be omitted in this analysis.

Another important figure of an actuator and that sometimes will be used to compare the different actuators, is their operating frequency. The operating frequency of the actuator is defined as the frequency at which cycles of contraction and retraction can be completed. The frequency may be limited by the efficiency of the actuator or by the physics of the used actuation principle. The actuation frequency together with the work density of the actuator will determine the power density, which is a performance figure that cannot be modified by a smart design because of the conservation of energy law.

When printing an actuator it is important to have a material that does not require a small layer thickness, since this would require a more expensive printer and a longer printing time. In the same way the layer quality and uniformity of the layer that is required are important. The requirement for a high quality layer often means that the layer has to be build up out of several thinner layers, which would mean that a printer with a lower layer thickness is required.

2.2 The piezoelectric actuator

The dimensions of piezoelectric materials will change when an electric field is applied. The actuator will expand or contract depending on the sign of the voltage that is supplied. Piezoelectric actuators in general are known to be capable of moderate strains of 3.5 %, high work densities of 320 kJ m^{-3} and good efficiencies (Madden et al., 2004).

The required materials can be printed, however they generally necessitates high polarisation and actuation fields, which requires low layer thicknesses and a high layer uniformity and quality. In appendix A the performance of one of the best piezoelectric polymers that is commonly available and that might be printed, PVDF-TrFE, will be estimated for two different layer thicknesses and an actuation voltage of 300 V. The results of this analysis are summarised in Table 2.1.

Table 2.1: Estimate of the performance of PVDF-TrFE

Maximum strain	0.44 %	0.02 %
Work density	13 MJ m^{-3}	600 kJ m^{-3}
Operating frequency	0 Hz - >1 Hz	0 Hz- >1 Hz
Required layer thickness	1-3 µm	5-15 µm
Cost	27 €/g	27 €/g

This analysis shows that even at very small layer thicknesses of 1-3 µm sheet actuators based on one of the best piezoelectric polymers that is commonly available, are not expected to produce enough strain to be useful in printed robotic systems. This makes the sheet actuator based on PVDF-TrFE unsuitable for use in complex robotic systems

Due to the high work and power density of the material, the material could be suitable when used in combination with a stepping mechanism. However this is considered outside of the scope of this work.

2.3 The electro-magnetic actuator

Almost all electrical actuators larger then a few millimetres that are in use today, are electromagnetic actuators. It therefore makes sense to investigate the possibility of printing this type of actuator. Unfortunately magnetic actuators require materials that can be strongly magnetised and conductors that can handle large current densities.

To evaluate the feasibility of this type of actuator, the performance of a voice coil actuator in combination with some 3D printable materials is estimated in appendix B. The expected performance of a voice coil made out of Neofer 25/60p and silver ink can be found in table 2.2.

Table 2.2: Expected properties of a voice coil actuator made from Neofer 25/60p and silver ink

Maximum strain	50 %
Work density	0.8-1.6 kJ m^{-3}
Operating Frequency	0 Hz - >1 Hz
Required layer thickness	>200 µm
Cost	2.5-25 €/g

Based on the expected performance of the Neofer 25/60p and silver ink voice coil actuator it can be concluded that a magnetic actuator with a work density that approaches the work density of a human muscle and a strain that exceeds that of a human muscle, might be printed. However the currently analysed voice coil actuator does still contain moving parts and therefore might not be easily integrated in a printed complex robotic system.

2.4 The dielectric elastomer actuator

A dielectric elastomer actuator (DEA) consists of a compliant material with a high dielectric strength, that is placed in between two electrodes. When a high voltage is applied, Maxwell stresses cause the material to contract. The actuators have been shown to be capable of high work densities, strains and power densities (beyond 1 MJ m^{-3}) (La and Lau, 2013; Brochu and Pei, 2010; Stoyanov et al., 2013; Pelrine et al., 2000). However they often suffer from premature breakdown, require high actuation voltages and often also require prestraining of the material in order to improve the breakdown strength (Brochu and Pei, 2010).

Since additive manufacturing does allow the fabrication of complex systems, the actuation voltage required might be reduced by fabricating a dielectric elastomer that consists of many

small layers. For the same reason the effect of premature breakdown might be reduced by introducing redundancy and fuses.

Prestrain on the other hand cannot easily be added to the material in a printing process. This section therefore will only evaluate the performance of an unstrained dielectric elastomer, which generally means a reduction of one order for the dielectric strength (Risner, 2008).

To analyse the feasibility of printing this type of actuator, an estimate of the performance of a simple type DEA, the sheet actuator, will be evaluated in appendix C. This will be done using an printable elastomer with a high dielectric strength and a relatively low dielectric constant. The results of this performance estimate are summarised in table 2.3

Table 2.3: Estimate of the performance of CN9018

Maximum strain	20 %
Work density	2kJ m^{-3}
Operating Frequency	0 Hz - >1 Hz
Required layer thickness	<3-10µm
Cost	Unknown

Based on this evaluation it is expected that a printed dielectric elastomer sheet actuator can approach the energy density and strain of a human muscle, within the set voltage limit, when printed at layer thicknesses in between 3 and 10 µm.

2.5 The ionic actuator

Ionic actuators have the advantages that they do not require high voltages and small layer thicknesses to generate large strains. However they generally have a low power density and a low efficiency.

2.5.1 The Nafion actuator

A material that can be used in the fabrication of an ionic actuator is sulfonated tetrafluoroethylene. It is sold under the brand name Nafion and a precursor material for Nafion can be bought in the form of beads. The beads were sold in December 2016 for 5,70 euro per gram (Ion Power, 2017). Nafion precursor can be processed into 3D printer filament, as is done in (Carrico et al., 2015). Nafion can be functionalised by soaking it inside a bath of KOH and deionised water after it is printed. There are little requirement to the uniformity and isotropy of the layers.

This same paper describes a 30.5 mm long, 11.5 mm wide and 1 mm thick beam that bends 3 mm at 3 V and 50 mHz. By using standard beam theory, these data can be used to estimate the strain in the material. The performance of the actuator is sumarised in table 2.4

Table 2.4: Properties of the Nafion actuator described in (Carrico et al., 2015)

Maximum strain	0.16 %
Work density	unknown
Operating frequency	0 Hz - <1 Hz
Minimum layer thickness	>200 µm
Cost	6 €/g

2.5.2 The lithium ion actuator

The electrodes of lithium-ion batteries have the tendency to expand when they are charged, due to intercolation of lithium ions. This generally is considered to be a disadvantage of the lithium ion batteries, however this effect makes that li-ion batteries also can be used as an

actuator (Chin et al., 2006). Due to the high energy storage density of li-ion batteries, the work density is limited by the maximum stress the actuator can handle without breaking.

Printing this actuator might be feasible since both carbon black filled filaments (i.e. PI-ETPU) as well as semipermeable membrame filaments (i.e. PORO-LAY LAY-FOMM) that can be filled with an electrolyte are available.

Chin et al. reports an actuator that combined a strain of 1.25 % at a constant load of 10 MPa (Chin et al., 2006), which corresponds to an energy density of $125\,\mathrm{kJ\,m^{-3}}$. The charge and discharge cycles of the battery however both took 2 hours, which results in an operating frequency that is far below the required operating frequency.

Table 2.5: Properties of the li-ion actuator described in (Chin et al., 2006)

Maximum strain	1.25 %
Work density	$125\,\mathrm{kJ\,m^{-3}}$
Operating frequency	0 Hz-140 µHz
Minimum Layer Thickness	Unknown
Cost	1 €/g

2.5.3 Conclusion

The 3D printed ionic actuator based on Nafion described by Carrico et al. does not deform enough to be useful in a complex robotic system. A lithium ion based actuator described by Chin et al. shows more deformation, however this actuator does not meet the operating frequency requirement.

2.6 The electret actuator

An electret is the electrostatic equivalent of the magnetostatic magnet, in that inside the electret there is a fixed electric field. However in contrary to the magnetic domain, there exist monopoles in the electric domain, which in the form of charged particles in the air make that the electric field outside the electret will be cancelled out. However an electret does generally show piezoelectric properties. For a more detailed analysis of electrets and ferroelectrets see Appendix D.

Sborikas et al. have described a screen printed ferroelectret (Sborikas et al., 2014). The ferroelectret is made by screen printing a pattern of polycarbonate ink on a polycarbonate sheet of 50 µm thick. The second time another polycarbonate sheet is placed on the wet polycarbonate layer. By using different formulations of ink, the screen printing resulted in solid material and foam or solid material and air. The total thicknesses of the ferroelectrets were 220 and 230 µm.

Above polarisation voltages of approximately 2 kV the material showed a piezoelectric constant in the order of $25\,\mathrm{pC\,m^{-1}}$. At an actuation voltage of 300 V this would result in a strain of $3.4{\cdot}10^{-5}$ (using Equation A.1).

2.6.1 Conclusion

The ferroelectric material developed by Sborikas et al. might be interesting in the development of sensors, however as an actuator in robotic systems the material is not suitable. Printing a ferroelectret or an electret out of a material with a lower Young's modulus might result in a material with a higher piezoelectric constant.

2.7 The thermal actuator

Some plastics that can be 3D printed have a relatively large thermal expansion coefficient, see Table 2.6. Therefore by combining an electric heating element in a 3D printed structure, the

material can be expanded. When PVDF for example is heated from 20 to a 120 °C, it will observe a strain of 1.9 percent. According to Equation 2.1, this corresponds to a work density

$$\begin{aligned} W_{\mathrm{d}} &= \frac{1}{2} Y \epsilon^2 \\ &= 0.5\,\mathrm{MJ\,m^{-3}} \end{aligned} \tag{2.3}$$

Where Y is the Young's modulus of PVDF (3 GPa (Rajala and Lekkala, 2010)) and ϵ is the strain of the material. The minimum amount of energy required to heat up the plastic from 20 to 120 °C, when there is no conduction, is

$$\begin{aligned} W_{\mathrm{in}} &= C \Delta T \rho \\ &= 202\,\mathrm{MJ\,m^{-3}} \end{aligned} \tag{2.4}$$

Where C is the thermal expansion coefficient of the material ($1120\,\mathrm{J\,K^{-1}\,kg^{-1}}$ for PVDF (makeitfrom, 2017)), Δt is the difference in temperature and ρ is the density of the material ($1800\,\mathrm{kg\,m^{-3}}$ for PVDF(makeitfrom, 2017)). The maximum efficiency of this process therefore is only 0.25 %. It is therefore expected that the actuator will not be able to reach the required maximum operating frequency of 1 Hz, without overheating.

Table 2.6: Linear expansion coefficients of some 3D printable plastics

PVDF	$190\,\mu\mathrm{m\,m^{-1}\,K^{-1}}$ (The Quadrant group, 2017)
ABS	72 - $108\,\mu\mathrm{m\,m^{-1}\,K^{-1}}$(ToolBox, 2017)
PE	108 - $200\,\mu\mathrm{m\,m^{-1}\,K^{-1}}$(ToolBox, 2017)

Table 2.7: Expected properties of a thermal actuator

Maximum strain	< 2 %
Work density	$< 0.5\,\mathrm{MJ\,m^{-3}}$
Operating frequency	0 Hz - <1 Hz
Required layer thickness	>200 µm
Cost	<1.5€/g

2.8 The steam actuator

Miriyev et al. (2017) have shown an a actuator that uses Joule heating to evaporate alcohol encapsulated inside an elastomeric material. This resulted in an actuator with a large work density and a large strain. However the actuator has to be heated and cooled down, which is a slow process that will get slower as the actuator gets bigger, since the surface to volume ratio gets smaller. The performance of this steam actuator is summarised in table 2.8.

This type of actuator is expected to be easily printable by filling printing a conductive filament with pores, and later filling these pores and sealing them.

Table 2.8: Performance of the steam actuator fabricated by Miriyev et al. (2017)

Maximum strain	120 %
Work density	$372\,\mathrm{kJ\,m^{-1}}$
Operating frequency	0 Hz - <0.01 Hz
Required layer thickness	>100 µm
Cost	<1 €/g

Expect from the operating frequency all requirements are met by the steam actuator. Improving the actuation frequency however is expected to be challenging, due to a lack of good thermal conductors that can be printed. Furthermore the efficiency of the actuator will be low.

2.9 The supercapacitor actuator

Super capacitors have a high energy density and some are capable of charging and discharging rates within the required operating frequency of 1 Hz, therefore in case there would be a dependency of the stored energy and the strain of the capacitor, the super capacitor actuator might make a good actuator.

Torop et al. (2011) demonstrated the use of a supercapacitor as an actuator. The performance of this actuator is summarised in table 2.9. This actuator is expected to be printable since filaments filled with high aspect ratio carbon particles and filaments for the construction of semipermeable membranes are already available.

Table 2.9: Performance of a steam actuator fabricated by Miriyev et al. (2017)

Maximum strain	0.071 %
Work density	12 $J m^{-1}$
Operating frequency	0 Hz-1 Hz
Required layer thickness	>100 µm
Cost	unkown

Therefore a super capacitor actuator is interesting as a sensor or as an energy harvester due to it's low voltage requirements. Further improvement of the dependency of the capacitance of the super-capacitor on the strain of the material might make the actuator also suitable as an actuator, however currently the expected performance is lower than the performance of human muscles.

2.10 The electrolysis actuator

Svetovoy et al. have described an actuator that uses the pneumatic energy of hydrogen and oxygen gas generated by hydrolysis (Svetovoy et al., 2011, 2013, 2014, 2016). They discovered that when an AC signal is applied to the electrodes, such that hydrogen and oxygen are generated at the same electrode sequentially, but at fast modulation rates, the bubbles will ignite automatically under certain conditions.

Except from the question if the conditions for automatic ignition can be met in a 3D printed actuator, the efficiency of the actuator might be problematic. The efficiency of the actuator described in (Svetovoy et al., 2013) is very low. This is due to the fact that there is a constant combustion of hydrogen and oxygen, even when the membrane is not expanding, which creates a lot of heat.

Even when the actuator would be driven by a DC signal and the gas would be ignited with a spark, the maximum efficiency of the actuator still is only a few percent, see appendix E. This is since only a small part of the energy involved in the electrolysis process is stored in pneumatic energy instead of in chemical energy.

A very low efficiency would make it likely that the actuator is not able to dissipate enough heat to be able to reach the required power density. This would mean that the actuator either will not be able to reach the required work density or the required operating frequency without destroying itself.

2.11 Conclusion

Based on the data in Table 2.11, one could conclude that there is no actuator that is able to meet all requirements. However the magnetic and the electrostatic approach come close.

However the silver glue material that is required to print the silver glue actuator is very expensive and a printer that can print a traditional DEA at the required layer thicknesses is not available. However a printer that can print the materials required to fabricate a DEA at a larger layer thicknesses is very cheap and available.

Therefore it will be attempted to print a DEA using this printer and to enhance the dielectric constant of the used dielectric such that the performance is not compromised.

Table 2.10: Comparison of the estimated performance of the most promising types of actuators

	Steam	Magnetic	Electrostatic	Thermal
Maximum strain	1.2	0.5	0.2	$< 2 \cdot 10^{-2}$
Work density	$372\,\mathrm{kJ\,m^{-3}}$	$0.8\text{-}1.6\,\mathrm{kJ\,m^{-3}}$	$2\mathrm{kJ\,m^{-3}}$	$< 0.5\,\mathrm{MJ\,m^{-3}}$
Operating frequency	<0.01 Hz	0 Hz - >1 Hz	0 Hz - >1 Hz	0 Hz - <1 Hz
Required layer thickness	>100 µm	>200 µm	<4-12µm	>200 µm
Cost	<1€/g	2.5-25€/g	Unknown	<1.5€/g

Table 2.11: Estimates of the performance of different types of printed actuators

	Steam	Magnetic	Electrostatic	Thermal
Maximum strain	++	+	+	-
Work density	+	-	-	++
Operating frequency	–	+	+	–
Required layer thickness	+	+	- -	+

3 Design

3.1 Introduction

In Chapter 2 it is argued why the DEA concept will be used for the fabrication of the actuator. Generally the design of a DEA can be split in two parts, one is the design of the conductors and the other is the design of the dielectric, see figure 3.1

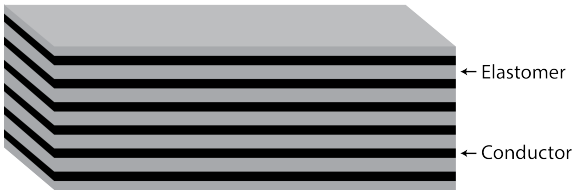

Figure 3.1: The dielectric elastomer actuator (DEA)

3.2 The dielectric

The dielectric of an elastomer has a large influence on the performance of the DEA. In the design of the dielectric first the specifications for the dielectric will be discussed. Next several strategies on how to achieve this will be discussed.

3.2.1 Specifications

For small strains, a linear elastic dielectric and infinitely thin electrodes the strain of the actuator that can be achieved can be approximated using equation C.2:

$$s = \frac{1}{2}\frac{\epsilon_r \epsilon_0 E^2}{Y} \tag{3.1}$$

In case of electrodes with a finite thickness, the stiffness of the electrodes will have an influence on the effective stiffness of the dielectric and the strain will become:

$$s = \frac{\epsilon_r \epsilon_0 E^2}{Y_d^{'}} \tag{3.2}$$

Where Y_d' is the effective Young's modulus of the dielectric with electrodes, see Appendix F. The work density that can be achieved for small strains and a linear elastic dielectric is:

$$\begin{aligned} W_d &= \frac{1}{8} s^2 Y_{tot}^{'} \\ &= \frac{1}{8}\frac{\epsilon_r^2 \epsilon_0^2 E^4 Y_{tot}^{'}}{Y_d^{'2}} \end{aligned} \tag{3.3}$$

Where $Y_{tot}^{'}$ is the effective Youngs modulus of the dielectric and the electrodes, see appendix F.

Young's modulus

In general a lower Young's modulus will result in a larger strain for a given stress. However this does not always mean that a larger energy density can be achieved. As discussed in Appendix G dielectric elastomer actuators can become in-stable. In fact when assuming a linear elastic dielectric and no external forces, the maximum strain before the actuator becomes in-stable is 50 %. When this kind of stability is desired, the maximum energy density that can be achieved increases with increasing effective Young's modulus, see equation 3.3.

To achieve this stability and the work density that this work aims for, the following effective Young's modulus is at least required:

$$\begin{aligned} Y'_{\text{tot}} &= 2\frac{W_{\text{d}}}{s^2} \\ &= 64\,\text{kPa} \end{aligned} \tag{3.4}$$

Electric field

A larger electric field quadratic-ally increases the strain of the actuator and for small strains the power density increases with the 4th power of the electric field. Clearly the applied electric field has a big influence on the performance of the actuator.

There can be two factors that limit the maximum electric field that can be applied. The first one is the dielectric strength of the material. The second limit follows from the maximum safe actuation voltage and the minimum thickness at which a dielectric layer can be printed.

The maximum safe actuation voltage for AC signals is set to 300 V. The minimum thickness at which a dielectric layer can be printed is determined by the minimum layer thickness of the printer and the number of layers that is required to print a layer which quality is high enough to separate the electrodes completely.

The minimum thickness at which a completely separating layer can be printed, depends on the used printing technique, the mechanics of the used printer, how well this printer is fine tuned and also the amount of particles in the air. See section 4.2 for a summary of the available printers and their resolutions.

Dielectric constant

Increasing the dielectric constant of a material makes that at the same electric field and Young's modulus a higher strain and energy density can be achieved. Increasing the dielectric constant of the material would therefore make stronger actuators possible using the same printer and printing techniques.

Resistivity

The presence of moving charged particles inside the dielectric, can have multiple effects on the performance of the actuator. The effect depends on the exact nature of these charged particles and there behaviour at the electrodes. Some of the possible situations and their influence are discussed below. Note that a combination of the situations below is also perfectly possible.

- **Free electrons and transmissive electrodes** will cause a reduction of the efficiency of the actuator, but will not deform the electric field inside the dielectric and therefore will not the change strain or energy density of actuator.
- **Free moving ions and transmissive electrodes** will reduce the efficiency of the actuator and might cause deterioration of the electrodes due to chemical reactions.
- **Free ions or electrons and blocking electrodes** will cause a buildup of charge at the electrodes, that will cancel out the electric field in the dielectric, cancelling out the electrostatic attraction in between the electrodes. This effect however can be prevented by using an AC actuation voltage (Sounart et al., 2005), however this comes at the cost of the efficiency of the actuator since more heat will be generated in the electrodes and the drive electronics.

Since there is no design goal for efficiency of the actuator there also is no specification for the minimum required resistivity. The only requirement is that the heat produced or the chemical reactions occurring do not cause degradation of the actuator or lead to unsafe situations.

Conclusion

The dielectric material should have a low Young's modulus (but the effective Young's modulus should be above 64 kPa), a high dielectric strength, a high dielectric constant and a reasonably high resistivity.

3.2.2 Increasing the dielectric constant

As explained in section 3.2.1 increasing the dielectric constant of the dielectric, will make it possible to fabricate a more powerful actuator at the same layer thickness. In the following sections several ways of increasing the dielectric constant will be discussed.

Spherical particles

Filling an elastomer with particles with a high dielectric constant, i.e. $BaTiO_3$, has been shown to improve the dielectric constant of the material (Zhang et al., 2008). However adding high concentrations of the ceramic powder to the elastomer generally introduces deterioration of the mechanical properties (Huan et al., 2016). For this reason generally only small fractions (0-20%) of powder are added. In this case the dielectric constant of the material follows the Maxwell Garnett formula. The Maxwell Garnett formula describes the effect on the effective dielectric constant of a medium by spherical particles (Sihvola, 2000).

$$\epsilon_{\text{eff}} = \epsilon_m + 3c\epsilon_m \frac{\epsilon_p - \epsilon_m}{\epsilon_p + 2\epsilon_m - c(\epsilon_p - \epsilon_m)} \tag{3.5}$$

Where ϵ_m is the dielectric constant of the elastomer, ϵ_p the dielectric constant of the particles, ϵ_{eff} the effective dielectric constant of the elastomer and c the volume-fraction of the particles. For particles with a dielectric constant that is much larger then the dielectric constant of the liquid the previous equation reduces to:

$$\epsilon_{\text{eff}} = \epsilon_s \frac{1+2c}{1-c} \tag{3.6}$$

This relation is plotted for a volume fraction of 0 to 20 percent in figure 3.2.

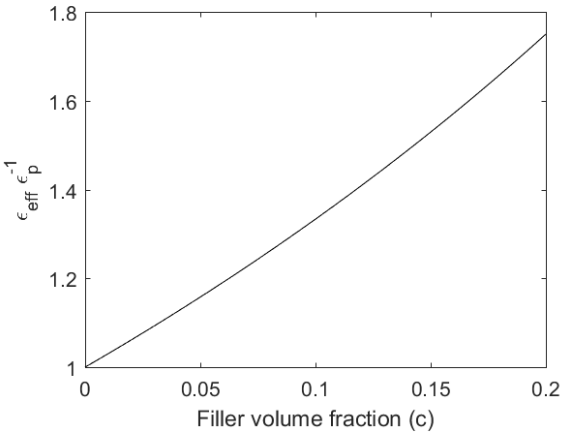

Figure 3.2: The change in dielectric constant for increasing volume fractions

High aspect-ratio particles

Filling an elastomer actuator with particles consisting of a single sheet or platelets of graphene, can improve the dielectric constant of the elastomer with several orders when the filling ratio approaches the percolation threshold (Yuan et al., 2015; Yousefi et al., 2014). Percolation for these particles occurs at several percent and the influence on the mechanical properties is therefore expected to be smaller.

One way to analyse such a composite, with a low concentration of particles, is to take a look at the effective dielectric constant of a media with randomly distributed ellipsoids. In this case the effective dielectric constant can be calculated using the following equation (Sihvola, 2000)

$$\epsilon_{\text{eff}} = \epsilon_m + \epsilon_m \frac{\frac{c}{3}\sum_{j=x,y,z} \frac{\epsilon_p - \epsilon_m}{\epsilon_m + N_j(\epsilon_p - \epsilon_m)}}{1 - \frac{c}{3}\sum_{j=x,y,z} \frac{N_j(\epsilon_p - \epsilon_m)}{\epsilon_m + N_j(\epsilon_p - \epsilon_m)}} \tag{3.7}$$

Where ϵ_m is the dielectric constant of the elastomer, ϵ_p the dielectric constant of the particles, ϵ_{eff} the effective dielectric constant of the elastomer with particles and c the volume of the particles. N_j are the depolarisation factors of the spherical particles that can be calculated using:

$$N_j = \frac{a_x a_y a_z}{2} \int_0^\infty \frac{1}{(k + a_j^2)\sqrt{(s + a_x^2)(s + a_y^2)(s + a_z^2)}} dk \tag{3.8}$$

With $a_x.a_y$ and a_z the length of the semi-axes of the ellipsoid. For example, for a disk shaped particle, $a_x \to \infty, a_y \to \infty$, the depolarisation factors are $N_x = N_y = 0$ and $N_z = 1$ (Landau et al., 1984). The equation can be applied to graphene particles by using that the dielectric constant of a conductive particle goes to infinity.

$$\lim_{\epsilon_i \to \infty} \epsilon_{\text{eff}} = \epsilon_m + \frac{1}{3}\frac{c}{1-c}\left(\frac{1}{N_x} + \frac{1}{N_y} + \frac{1}{N_z}\right)\epsilon_m \tag{3.9}$$

For ellipsoidal particles with with $a_x = a_y$ =12.5 µm and a_z =10 nm the depolarisation factors have been calculated using Matlab. The values that were found were $N_x = N_y = 0.62 \cdot 10^{-3}$ and $Nz = 0.9987$. The effective dielectric constant relative to the dielectric constant of the medium for small loading constant of these particles can be found from figure 3.3.

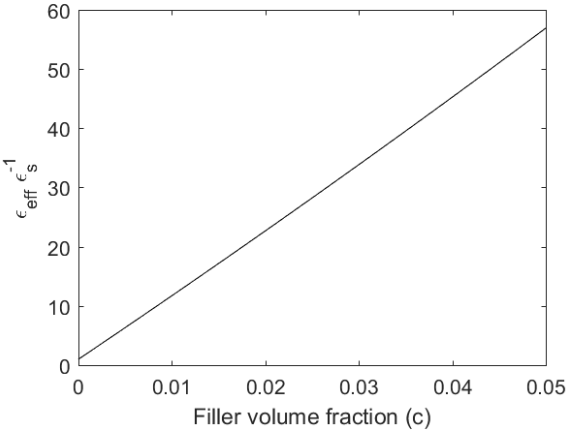

Figure 3.3: The effective dielectric constant relative to the medium with randomly oriented conductive ellipsoidal particles with $a_x = a_y$ =12.5 µm and a_z =10 nm

However since Graphene particles are conductive the dielectric constant might come at the cost of an increase of the conductivity of the material as is seen in (Yuan et al., 2015; Yousefi et al., 2014). A too large reduction of the resistivity of the material might cause the material to melt at high voltages.

Polar liquid composite

Another way to increase the effective dielectric constant of a material,which will only make the material softer, is to print it porous and fill it with a fluid with a high dielectric constant. When this fluid is mixed such that both phases have similar shape and are distributed randomly through the whole system, the effective dielectric constant can be approximated using the Bruggeman symmetrical medium equation (Sihvola, 2000).

$$\frac{c(\epsilon_l - \epsilon_{\text{eff}})}{\epsilon_l + 2\epsilon_{\text{eff}}} + (1-v)\frac{\epsilon_m - \epsilon_{\text{eff}}}{\epsilon_m + 2\epsilon_{\text{eff}}} = 0 \tag{3.10}$$

Where ϵ_l is the dielectric constant of the liquid and ϵ_m is the dielectric constant of the material the porous material is made of. This equation can be rewritten to:

$$\epsilon_{\text{eff}} = -\frac{1-3v}{4}\epsilon_l - \frac{-2+3v}{4}\epsilon_l + \frac{1}{4}\sqrt{8\epsilon_l\epsilon_m + ((1-3v)\epsilon_l + (-2+3v)\epsilon_m)^2} \tag{3.11}$$

Note that this mixing rule is no more than a approximation since the exact geometry of the porous material will have an influence on the exact dielectric constant. However the equation shows that for a random mixture the effective dielectric constant will go to infinity, if the dielectric constant of the fluid will go to infinity, see Figure 3.4.

A disadvantage of high-k liquids is that they are always polar and therefore dissolve salts. However as long as the liquid is aprotic the number of ions in the liquid is finite and as long as this number is low the liquid can be used as a dielectric.

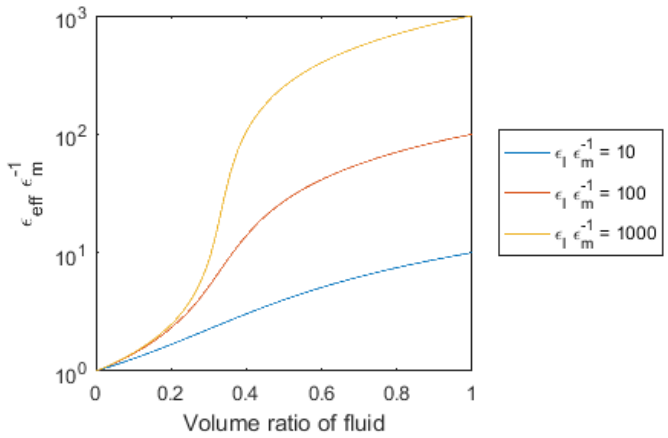

Figure 3.4: The effective dielectric constant for liquids with different dielectric constants.

Suspension composites

The dielectric constant of liquids is practically limited, however their dielectric constant might be increased by suspending particles inside the fluid.

When examining suspensions of high-k particles one should realise that they particles will observe a force that will try to move them to the position which maximises the dielectric constant of the dielectric under influence of an electric field. This is since the energy in the system (real

energy not co-energy) is minimised.

$$\begin{aligned} U &= \frac{1}{2}\frac{q^2}{C} \\ &= \frac{1}{2}\frac{dq^2}{\epsilon A} \end{aligned} \tag{3.12}$$

Where C is the total capacitance of the actuator, q is the charge on the plates, A is the total area of all plates, d is the thickness and ϵ is the dielectric constant of the material.

Furthermore it should be taken into account that at the interface of a particle often an exchange of charge occurs between the particle and the liquid, that results in a potential difference between the particle and the fluid that is known as the Zeta potential. The net charge of the particles makes that they repel each other, therefore a high absolute value of the Zeta potential makes that the suspension is stable (Atkins and Paula, 2006).

Some of the best studied suspensions are electrorheological fluids, fluids that change viscosity under the influence of an electric field. For example Ma et al. (2003) extensively studied the behaviour of coated Barium Titanate particles in a fluid and they found that particles form pillars from on electrode to the other. The particles in these pillars are in a BCT lattice. They also calculated the maximum dielectric constant when the particles are in a BCT lattice, see figure 3.5.

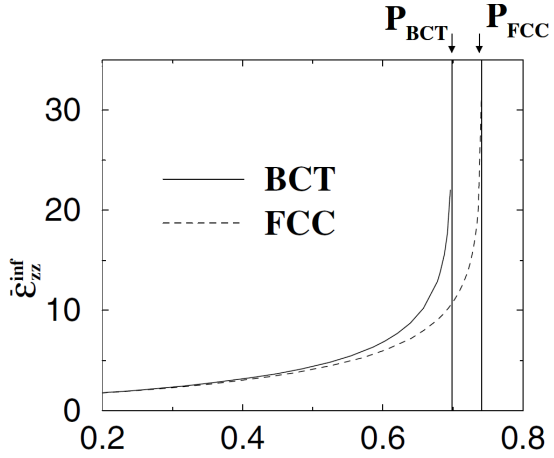

Figure 3.5: The effective dielectric constant for large concentrations of spherical particles in BCT and FCC crystal orientation. Image courtesy of Ma et al. (2003)

Conclusion

The addition of low concentrations of spherical high-k particles to the dielectric will not cause a significant improvement in the dielectric constant. The addition of conductive high aspect ratio particles, such as graphene nanoplatelets, will result in a significant increase of the dielectric constant, but might also cause an unacceptable increase in conductivity. The addition of high-k particles with a high aspect ratio or conductive high aspect ratio particles coated with an insulator however might be able to increase the dielectric constant significantly without increasing the conductivity.

Mixing a polar liquid with the dielectric will results in a decent increase of the dielectric constant. The addition of the same high-k particles to a liquid is expected to have higher influence on the dielectric constant than when they are added to a solid, since the particles will be free to move to the position that maximises the dielectric constant.

3.3 The flexible conductor

The second part of a DEA is it's conductor. The conductive filament will be bought from commercial suppliers. Therefore only a set specifications will have to be made and no further design is necessary.

3.3.1 Specifications

In this section the specifications of the conductor concerning it's Young's modulus and it's resistivity will be discussed.

Young's modulus

Since the dielectric that will be used has a Poisson ratio close to 0.5, the electrodes will have to expand when the actuator contracts. This will have an influence on the stiffness of the dielectric. As derived in appendix F the effective Young's modulus, describing the stiffness of the dielectric with electrodes when there is no external stress working on the actuator is:

$$Y'_{\mathrm{d}} = E_{z,d}\left(1 + \frac{E_{x,c}\,t_c}{E_{x,d}\,t_d}\right) \tag{3.13}$$

Where $E_{z,d}$ is the Young's modulus of the dielectric in the $z-$direction, $E_{x,c}$ and $E_{x,d}$ are the Young's moduli in the $x-$direction of respectively the conductor and the dielectric and t_c and t_d are the thickness of the conductor and the dielectric.

This suggest that the conductor should have a Young's modulus in the $x-$direction that is as low as possible or at least in the order of the Young's modulus of the dielectric. In case of 3D printing the shape of the conductor is not limited to a sheet and electrodes with holes in them can be used to reduce the stiffness of the electrodes in the $x-$direction. However the design and analysis of these shapes is considered outside the scope of this assignment.

It should also be noticed that since the conductor and the dielectric are mechanically coupled and incompressible, the strain in the $x-$ and $z-$direction will be the same in both materials (see also Appendix F). This means that the strain of the electrodes will contribute to the total strain of the actuator.

3.3.2 Thickness

Increasing the thickness of the conductor will decrease the strain and energy density of the actuator, since less volume will be used as an actuator. Therefore a conductor with a thickness as small as possible is desired.

Resistivity

The resistance of the electrodes combined with the capacitance of the actuator will make that it will take a certain time to charge up the actuator. If this RC time becomes too large it will limit the frequency response of the actuator.

As described in section 3.3.2 an electrode as thin as possible is desired. Therefore in this derivation it will be assumed that the conductor sheet has the same thickness as the dielectric sheet, which will be the smallest thickness at which a high quality layer can be printed.

An estimate of the required resistivity can be obtained by calculating the resistivity of one sheet electrode and the capacity of a layer of dielectric. The resistance of a square sheet electrode consisting of a material with a resistivity ρ and a thickness d is

$$R = \frac{\rho}{d} \tag{3.14}$$

The maximum frequency f_{max} that the actuator can be actuated at will be in the order of the cutoff frequency of the RC circuit

$$f_{3\,\mathrm{dB}} = \frac{1}{2\pi RC} \tag{3.15}$$

Combined with the capacitance of a layer printed at the same layer thickness as the electrodes (d) and a relative dielectric constant ϵ_r, this results in the following estimate of the required resistivity.

$$\rho = \frac{1}{2\pi} \frac{d^2}{\epsilon_0 \epsilon_r A f_{3\,\mathrm{dB}}} \tag{3.16}$$

For an dielectric with a thickness of 10 µm, a relative dielectric constant of 30, an area of 1 dm^2 and a operating frequency of 1 Hz, a resistivity of 599 Ω cm would be required. According to equations 3.2, 3.3, F.8 and F.9 this would result in an actuator with a strain of 30 % and a work density of 8.9 kPa, for a dielectric and a conductor with a Young's modulus of 200 kPa.

Conclusion

The Young's modulus of the used electrodes should be similar to the Young's modulus of the dielectric or lower and the electrodes should be as thin as possible. The minimum required conductivity can be calculated using equation 3.16.

3.4 Conclusion

In order to fabricate a dielectric elastomer that is able to reach the required specifications, a dielectric is required with a high dielectric constant and a high dielectric strength. Also a conductor with a conductivity that is large enough to be able to charge and discharge the dielectric elastomer has to be printed. Both the dielectric and the conductor need to be printed at a very low layer thicknesses below 10 µm. The dielectric should be able to withstand the large electric field, therefore no chemical reactions that degrade the dielectric may occur.

To enhance the dielectric constant of the dielectric and increase the minimum required layer thickness, high-k particles with a high aspect ratio or conductive high aspect ratio particles coated with an insulator might be used. Also mixing a polar liquid with the dielectric might increase the dielectric constant.

4 Fabrication

4.1 Introduction

As described in section 3 in order to fabricate a dielectric elastomer, two types of material need to be printed. The first one is a dielectric with a high dielectric constant and dielectric strength. The second one is a conductor with a conductivity that is large enough to charge the electrodes at a rate of 1 Hz. Both materials should be as soft as possible and it should be possible to print them at a layer thicknesses below 10 µm.

In section 3.2 the inclusion of high aspect ratio particles also is discussed. However since both the particles as the equipment to make custom filaments were not available, it was not possible to fabricate these dielectrics.

4.2 Printer

As described in section 3.2 in order to fabricate a powerfull actuator, a very thin dielectric layer that still completely separates two conductors, has to be fabricated. This section will discuss the most promising printers that were available at the research group RAM and their capabilities of printing a very thin layer in between two conductors.

4.2.1 Objet Eden 260 Connex 3

The Objet Eden 260 Connex 3 is a polyjet printer from Stratasys. A polyjet printer consists of a inkjet head that prints UV curable material (Stratasys, 2017), see figure 4.1. The printer is capable of printing layers as thin as 16 µm. The printer is capable of printing materials with a low Young's modulus and combining multiple materials. However as far as known to the author no conductive materials are available for this printer.

Previously conductors have been embedded in poly-jetted prints by printing a dis-solvable material on the location where the conductor has to be placed Welleweerd (2017). After printing this material is dissolved and conductive ink is injected. The time of filling such a channel however increases when the aspect ratio of the channel increases, which in this case is very large. Furthermore the structure requires two separated conductors, which further complicates the fabrication process.

Figure 4.1: An Objet printer, image courtesy of (3DPrinterClassifieds.com, 2017)

Flashforge Creator Pro

The Flashforge Creator Pro(Flashforge, 2017) is a consumer grade FDM printer, see figure 4.2. A Fused Deposition Modelling printer prints by melting the to be deposited thermoplast using an extruder. The dual flexion extruder (Engineering, 2017) made by Diabase Engineering that is placed on this printer makes that the printer is capable of printing flexible materials. Both conductive flexible materials and insulation flexible materials are available.

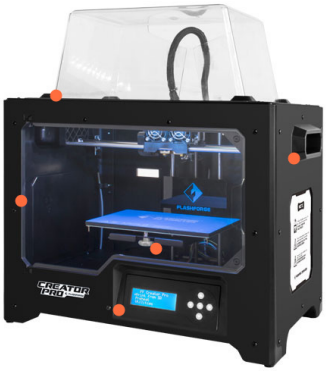

Figure 4.2: An flash-forge creator pro, image courtesy of (Flashforge, 2017)

The minimum layer thickness of the Flashforge is specified to be 100 µm. However this is not a hard limit, since the step size in the $z-$direction is lower. An estimate of the step size, based on the assumption of a 1.8° Nema 17 stepper motor, is 20 µm since the pitch of the thread on the z-axis is 4 mm. Note that most stepper motor drivers also feature micro steps, which are not taken into account in this calculation.

4.2.2 Conclusion

The Flashforge Creator Pro is the only printer of the two available printers that is capable of printing both conductive flexible materials as dielectric flexible materials. Therefore this is the printer of choice, although this printer is not specified to print at a layer thickness anywhere near the required minimum layer thickness.

4.3 Conductor

For the fabrication of the conductor several conductive filaments were available, which will be discussed in this section.

The resistivities specified in this section are the resistivities as specified by the manufacturers, which generally is the resistivity of the filament. The resistivity of the 3D printed material usually depends on the print settings and the geometry of the printed object.

4.3.1 Blackmagic conductive TPU

Blackmagic conductive TPU (Graphene Labs, 2017) by Black Magic 3D, a company owned by Graphene 3D lab, is specified to have a conductivity of less than 1.25 Ω cm. It consists of TPU filled with Carbon black. The material is with a shore hardness of 90A also quite flexible. However since April 2017 this material is not sold in Filament form any more. Furthermore the material has been found to degrade after several months of shelf-live, making the material so brittle that it breaks inside the feeding tube. The source of this degradation is unknown. The settings used to print this material can be found in table K.1.

4.3.2 PI-ETPU 95-250

After April 2017 the only flexible conductor that was available was PI-ETPU 95-250 from Palmiga Innovations (Palmiga Innovations, 2017). The material consists of TPU filled with carbon black. According to the manufacturer the unprinted filament has a resistivity of 300 Ω cm, a shore hardness of 95A and can be extended up to 250 % strain. However the printed material has a much higher resistivity. There have been no signs of degradation with this filament. Some settings used to print this material can be found in table K.2.

4.3.3 PI-ETPU 85-700+

In August 2017 Palmiga Innovations kindly supplied their unreleased PI-ETPU 85-700+ filament. The conductivity of the unprinted filament is 80 Ω cm (2 wire measurement using a UNI-T UT10A multimeter). The shore hardness as reported by the manufacturer is 85A and maximum extension is more than 700 %. Like the previous PI-ETPU the resistivity of the printed filament reduces when the filament is placed in an oven at 150C for 1 hour. There also have been no signs of degradation. Some settings used to print this material can be found in Table K.2.

4.3.4 Electrifi filament

Electrifi filament from Multi3D (Multi3D LLC., 2017) is a filament that consists of a polyester filled with copper particles. According to the manufacturer the material can have a resisitivity as low as 0.01 Ω cm, however during tests with pieces of material with a thickness of less than 1 mm, inconsistent resistivities were measured ranging from 0.01 Ω cm for a piece of 1 mmx4.2 mmx30 mm(4-wire) to more than 10 MΩ cm for a piece of 0.4 mmx5 mmx30 mm (2-wire).

According to the manufacturer this could be because "the conductive copper particles used in the composite lost their contacts to each other in certain parts" when the material was stretched while taking it of the heatbed. This would make the material unsuitable for use in applications where a large strain is required. The settings used to print this material can be found in material can be found in table K.3.

4.3.5 Proto Pasta Conductive Filament

Proto Pasta is Polylactic acid (PLA) filled with carbon black particles. The material is decently conductive and has not shown any signs of degradation. According to the manufacturer the resistivity of a moulded part is 15 Ω cm. The material prints nice however since the material is based on PLA the material is much stiffer than the other materials. Some of the print settings used to print proto pasta can be found in table K.4

4.3.6 Conclusion

Blackmagic filament is not an option since it is not available in filament form any more. Electrifi is not an option since it's resistivity increases sharply and irreversible when it is strained to much. Of both PI-ETPU's and Proto Pasta, 85-700+ PI-ETPU is the most suitable since it has the lowest shore hardness and the lowest resistivity.

4.4 Dielectric

This section decribes the avaliable dielectrics and their print settings. Note that for printing layers under 100 µm fine tuning of the bed (using the screws underneath the bed) and the relative nozzle height (mechanically and in software using Global G-code Offsets) is necessary.

4.4.1 Ninjaflex

Ninjaflex by Ninjatek is a flexible filament made of Themoplastic Poly-Urethane (TPU). The material has a shore hardness of 85A and a tensile modulus of 12 MPa(Ninjatek, 2017). The material is printed at 100 µm and 50 µm using the settings in table K.5. For measurements of the dielectric constant of the material see 6.2.1. For measurements of the Young's modulus of this material, see 6.3.1.

4.4.2 X60 Ultra-Flexible Filament

X60 Ultra-Flexible Filament - White made by Makerspace, is a very flexible rubber with a shore hardness of 60A(Diabase Engineering, 2017) that is available since June 2017. The material is printed using the parameters in Table K.6. For measurements of the dielectric constant of the material see 6.2.1. For measurements of the Young's modulus of this material, see 6.3.1.

4.4.3 PORO-LAY LAY-FOMM 40 Porous Filament

PORO-LAY LAY-FOMM 40 Porous Filament from Lay Filaments is a filament that consists of a mix of about 50 % Polyvinyl alcohol (PVA) and 50 % TPU. The material can absorb water and then becomes very soft, the shore hardness according to the manufacturer is 40A(Matter Hackers, 2017b). The settings used to print this filament can be found in table K.7.

The PVA can be removed from the material by boiling the material in a pan with plenty of water and some dishwasher soap. This is done in the following process:

1. First the samples are dried in an oven at 60 °C for one night. This is done in order to be able to measure the dry weight of the samples with PVA, such that afterwards the weight loss can be examined. At this point in time also the impedance of the samples is determined to check if their fabrication was successful.
2. Next the samples are boiled in a water and soap mixture.
3. After this the samples are cleaned by placing them in demineralised water.
4. Then they are again dried in an oven at 60 °C overnight and their weight is measured again.

Some results obtained using this process are summarised in table 4.1.

Table 4.1: Resulting mass change of LAY FOMM 40 due to boiling

Dimension	Boiling time	Weight loss
10x40x0.3 mm	5 h	45 %
10x40x0.5 mm	9 h	15 %
10x40x2 mm	9 h	2 %

4.4.4 PORO-LAY GEL-LAY Porous Filament

PORO-LAY GEL-LAY Porous Filament is another porous filament from Lay Filaments (Matter Hackers, 2017a). The material consist for about 50 % of a poly-amide and for the remaining 50 % of PVA. The shore hardness of the material is unknown. Again the PVA can be dissolved by boiling the material in a pan with plenty of water and some dishwasher soap. The settings used to print this filament can be found in table K.8.

Conclusion

Although LAY FOMM 40 has the lowest shore hardness and might allow free moving particles inside it's pores, it is unpractical as a dielectric, since the material is only flexible in case it is filled with water or all the PVA is removed, which is a time consuming process. X60 is a more practical dielectric since it does not require any post processing before it can be used as dielectric. Furthermore as shown in Chapter 6, X60 can be plasticised using Propylene Carbonate which further decreases the Young's modulus and increases the dielectric constant of the material.

4.4.5 Filling liquid

In case the dielectric and the conductor are printed with an infill less than 100 %, a filling fluid can be used to fill up air void inside the material that arise due to the printing process. These voids are undesired since they could break down under the influence of large fields, increasing the field in the remaining dielectric. Furthermore the fluid can be used to enhance the dielectric constant of the material.

Polarity

The most common liquids with high dielectric strengths are a-polar liquids (i.e. mineral oil), since their breakdown voltage is high and their attraction to ions, and therefore their conductivity, is low. However these materials all have a relatively low dielectric constant due to the absence of polar groups. Therefore the used liquid should be a polar liquid.

Protic or aprotic

Protic liquids (i.e. water) are liquids that contain an ionizable proton in the molecule. Therefore a small part of the molecules will naturally decompose into ions and even when all impurities are removed the liquid still will have a finite conductivity. Since the liquid should have a low conductivity an a-protic liquids should be used.

Purity

The reduction in Gibbs energy when an ion dissolves in a liquid is described by the Born equation (Atkins and Paula, 2006).

$$\Delta_{\text{solv}} G^{\theta} = -\frac{z_i^2 e^2 N_A}{8\pi\epsilon_0 r_i}\left(1 - \frac{1}{\epsilon_r}\right) \tag{4.1}$$

Where z_i is the charge number of the ion, r_i is the radius of the ion and ϵ_r is the dielectric constant of the ion. Since the used liquid will have a high dielectric constant, the reduction in Gibbs energy when ions are dissolved will be larger. Therefore ions will be able to more easily dissolve in the liquid. In practice that will mean that if no special precautions are taken there will be a significant amount of ions from the environment that dissolve in the liquid.

This will lead to a higher ionic conductivity of the liquid, and therefore to more loss. However in an aprotic liquid as soon as the ions are removed the liquid the conductivity will decrease again. Therefore if a DC voltage is applied to the liquid the number of ions in the liquid can be reduced, since the ions will react at the electrodes.

Boiling point

Of course the liquid should stay inside the porous material and therefore should not evaporate. This can be done by sealing of the actuator afterwards. To keep the liquid inside the material before it is sealed off the it helps to use a liquid with a high boiling point. This is since generally these liquids will have a lower vapour pressure at room temperature.

It should be noted that it is not always true that a liquid with a higher boiling point has a lower vapor pressure at room temperature. However since the liquid follows the Antoine equation (Thomson, 1946) and the boiling point of the liquid is defined as the point at which the vapor pressure is equal to the atmospheric pressure (Nave, 2017), the boiling point can be used as a rough estimation of the vapor pressure at room temperature.

Plasticizer

Some liquids will enter a polymer and will stay in between strains of the polymer, reducing the Young's modulus of the polymer. This will allow for a further reduction of the Young's modulus of the material and is therefore considered beneficial. Since no information could be found

in literature on the plasticising effect of the examined chemicals on the used dielectrics, this property is not taken into account.

Options

A list of polar aprotic liquids can be found in table 4.2 together with their boiling point, dielectric constant and HMIS health hazard indication number.

Table 4.2: Different polar aprotic liquids

	Dielectric Constant	Boiling Point	HMIS health Hazard (Sciencelab, 2017)
Propylene carbonate (PC) (Bartnikas, 1994)	64.9	241.7	1
Dimethyl sulfoxide (DMSO) (LibreTexts, 2017)	47	189	1
Dimethylformamide (LibreTexts, 2017)	38	153	2
Acetonnitrile (AN) (LibreTexts, 2017)	37.5	81.6	2
Acetone (LibreTexts, 2017)	21	56.5	2
Nitrobenzene (NB_z) (Bartnikas, 1994)	34.82	210.8	3

Conclusion

Propylene carbonate appears to be the most suitable liquid since it has the largest dielectric constant and the highest boiling point of all liquids that have been taking into consideration. Furthermore the liquid is part of HMIS health hazard class 1, meaning that it will only cause "Irritation or minor reversible injury" (Interactive Learning Paradigms Incorporated, 2016).

4.5 Test prints

In order to verify the performance of the most promising materials some test prints have been made. In this section the fabrication process of these samples will be described. Note that any dimensions in this section are the dimensions given to the test structures in the CAD files from which the structures were printed, except when explicitly stated otherwise. This is since due to the roughness of the 3D printed samples the actual thickness could not be measured accurately.

4.5.1 Impedance spectroscopy test pieces

Samples including electrodes

To test the performance of the PC filled Lay Fomm in the impedance and voltametry tests, a test sample which consists of a thin sheet of Lay Fomm in between two PI-ETPU 85-700+ electrodes is printed.

The electrodes are printed on the sample in order to reduce the influence of the chemical reactions of steel electrodes on the measurements. The electrodes are printed with an infill percentage of 72 % in order to speed up the rate at which the PVA can be dissolved.

Two types of test samples have been produced one with a 100 µm thick dielectric and one with a 50 µm thick dielectric. The 100 µm thick dielectric was printed using the 50 µm layer height print settings described in section 4.4.3, while the 50 µm thick dielectric was made using the 12.5 µm process.

See figure 4.3 for a picture of a 50 µm sample after this process

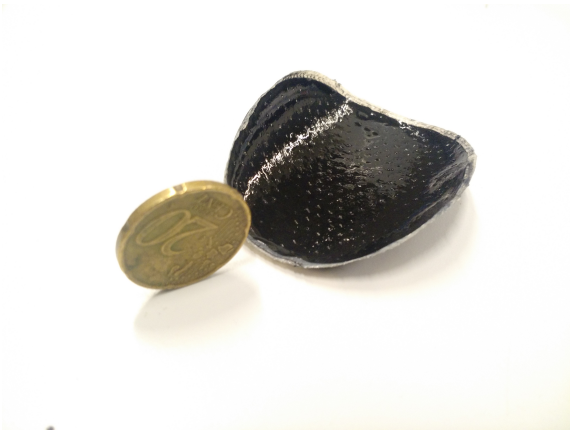

Figure 4.3: A PC filled Lay Fomm disk with a 50 µm thick dielectric

5 samples have been made of both the 100 µm and 50 µm samples. To get an indication of the thickness of the dielectric after printing, the capacitance and the electrode resistance of the dried samples were measured at 1 kHz by placing them in the modified resistivity adapter, see section 5.2.1.

To check if the fabrication process was successfull also the resistance in between the electrodes at 10 V was measured while the sample was in the modified resitivity adapter using a Keithley 2410 Source measurement unit. Samples with a dielectric resistance below 1 MΩ have been discarded. The properties of the various samples can be found in tables 4.3 and 4.4.

Note that due to the fact that the used marker was removed by the boiling process, the numbering given to samples was lost in this process. Therefore data on specific samples before the boiling step cannot be related to a specific sample after the boiling process.

Table 4.3: Properties of the 100 µm samples, after drying

before/after cooking	Property	Value	Standard deviation
before	Weight	962.3 mg	6 mg
before	Dielectric resistance	2 GΩ	1 GΩ
before	Electrode resistance	5.04 kΩ	91 Ω
before	Capacitance	1.24 nF	16 pF
after	Weight	709.5 mg	11 mg

Table 4.4: Properties of the 50 µm samples, after drying

before/after cooking	Property	Value	Standard deviation
before	Weight	517.5 mg	11 mg
before	Dielectric resistance	300 MΩ	102 MΩ
before	Electrode resistance (in z)	2.9 kΩ	270 Ω
before	Capacitance	2.07 nF	129 pF
after	Weight	343.0 mg	7 mg

After being placed in Propylene Carbonate the resistance of the electrodes increased dramatically, to more than 100 MΩ from one end of the electrode to the other (in the $y-$direction). This was unexpected and was the reason for further investigation of the influence of PC on the material properties of the electrodes and dielectrics.

Samples without electrodes

Since the electrodes stopped conducting under the influence of Propylene Carbonate further experiments have been performed using samples without electrodes. For the impedance spectroscopy tests it is practical to use a thicker piece of material, since the thickness of such a piece can be measured more accurately and print effects that occur on the bottom layer are less dominant. A thicker piece of material is also mechanically more robust. Therefore in this test a cylinder with a diameter of 52 mm and a thickness of 500 µm is used, see figure 4.4.

For each material two electrodes have been fabricated. For each of them the mass is measured using a scale and the thickness and diameter are measured using a caliper. This is done before and after they were plasticised using PC. Based on these parameters the change in volume and mass have been calculated and listed in Table 4.5. The figures given for the PI-ETPU 85-700+ material are the values obtained after baking the material for 1 day at 150 °C.

Table 4.5: The average increase of mass and volume after plasticising using PC

	Volume Increase	Mass Increase
X60	32 %	52 %
Ninjaflex Water	43 %	71 %
PI-ETPU 85-700+	26 %	38 %

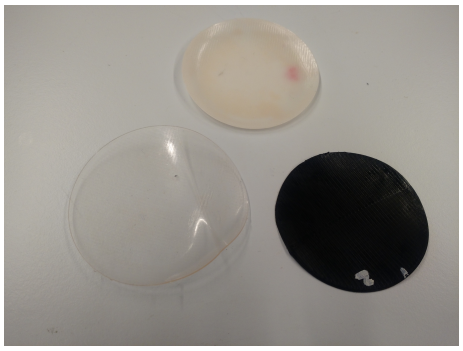

Figure 4.4: The samples after they were plasticised

4.5.2 Young's modulus test pieces

The test pieces used to test the Young's modulus of the used materials, consist of a block of 40 mmx10 mmx2 mm, see figure 4.5. The block is printed in PI-ETPU 85-700+, X60, Ninjaflex Lava ("orange") and Lay Fomm 40, using their 100 µm processes and a rectilinear infill with a 45° and −45° Infill Angle Offset. All pieces have been tested before and after they were soaked in Propylene carbonate for one night, except for the Lay Fomm 40 sample which has been boiled in water with soap for 3 hours instead.

The shape of the test pieces is a beam instead of the more complex shape of the ASTM D638 norm, to make sure the slicer is following a predictable pattern. An FEM simulation of the expected error, which is explained in more detail in Appendix I, shows that the expected error is less than 1 %.

Figure 4.5: The samples after plasticising with PC

4.5.3 Cantilever

As a prove of principle a cantilever has been fabricated. A cantilever structure is used because it easy to manufacture and still has a relatively large displacement at the tip of the actuator, especially when driven at the resonance frequency.

As a dielectric X60 is used, since this material can be used as a dielectric without post processing and the material is more flexible than Ninjaflex.

As the electrode material both PI-ETPU and Proto Pasta have been tried. Neither of these materials was compatible with the plasticizer PC. PI-ETPU was plasticised and stopped conducting, as discussed in section 6.2.3 and section 6.2.1. Proto pasta's resistance did not increase as dramatically, however the X60 and Proto pasta layer separated. This is expected to be due to the large stress generated at the interface of X60 and the much stiffer Proto Pasta when the X60 is expanded by the plasticizer. Therefore the cantilever has not been plasticised and PI-ETPU is used since it has the lowest stiffness and therefore has the highest potential for being used in the final actuator.

The cantilever was baked at 150 °C in the centre of an oven on a borosilicate glass plate, with the very flat bottom of the sample stuck to the glass plate. The dimensions of the cantilever can be found in Figure 4.6. A picture of the cantilever can be found in Figure 4.7. It should be noticed that after the baking step the sample is still slightly curved along the x and the y axes.

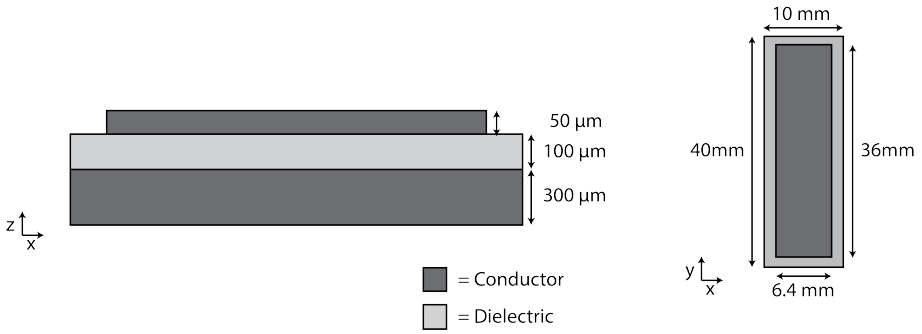

Figure 4.6: A drawing of the cantilever

Figure 4.7: A picture of the cantilever

4.6 Conclusion

The available fabrication techniques do not have the capabilities to print at the minimum layer thickness required for the fabrication of an actuator with the specified strain and work density. However it is possible to fabricate a dielectric elastomer actuator at larger layer thicknesses. The resulting actuator will not have the required strain or work density, but can serve as a proof of concept.

Furthermore it might be possible to increase the dielectric constant and decrease the Young's modulus of the dielectric by using a polar aprotic filling fluid. This would improve the strain and work density that can be achieved using this dielectric.

5 Measurements

5.1 Introduction

As discussed in section 3, the important electric properties of the dielectric are the materials dielectric constant, dielectric strength and the presence of charged particles and chemical reactions that can degrade the dielectric. Furthermore the most important electric property of the conductor is it electrical resistance. For both the dielectric and the conductor their Young's modulus is the most important mechanical property.

Since the final device is a proof of concept to show that a 3D printed dielectric elastomer actuator actually deforms, the deflection of a multi-morph cantilever will be measured.

5.2 Electrical characterisation

To measure the dielectric constant of the material, the concentration of free moving ions inside the material and the presence of chemical reactions, impedance spectroscopy will be used. To get a better idea about the nature of the chemical reactions a Cyclic voltametry experiment will be performed. To see if the resistance of the conductor is low enough a resistance measurement will be performed.

The dielectric strength is not measured, since with the current layer thickness the voltage required for these experiments is above the maximum voltage of the voltage sources that were available.

5.2.1 Impedance spectroscopy

A powerful tool to analyse both solid state and liquid dielectrics is impedance spectroscopy. In impedance spectroscopy the impedance of a material is determined over a wide range of frequencies.

Background

The goal of the impedance spectroscopy experiment is to identify:

- The dielectric constant of the material.
- The concentration of free moving ions in the dielectric.
- The presence of chemical reactions at the electrodes.

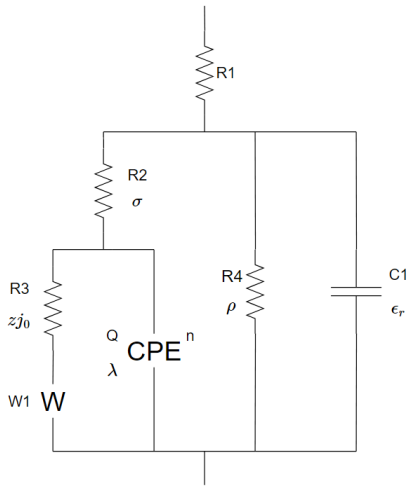

Figure 5.1: The model used to fit the analysed structures. The cursive letters in this Figure denote geometry independent parameters.

To do so the transfer function of the circuit in figure 5.1, which is based on the commonly used Randles circuit, is fit to the measured spectrum. This circuit does only model the AC behaviour of the system and the double layer in the Randles circuit is replaced with CPE element since this resulted in a better fit. In this circuit:

- **R1** represents the resistance of the electrodes. This resistor is only relevant in case PI-ETPU electrodes are used.
- **R2** represents the resistance due to ionic conductance. The resistance is dependent on the conductivity of the dielectric via:

$$R2 = \frac{A}{d\sigma} \tag{5.1}$$

Where A is the total area of the electrodes, d is the thickness of the dielectric and σ is the conductivity. According to the Kohlrausch's law of the independent migration (Atkins and Paula, 2006), for low concentrations of ions the conductivity depends on the concentration of ions and the limiting molar ionic conductivity of these ions in the media they are dissolved in, via

$$\sigma = \sum_i \nu_i c_i \tag{5.2}$$

Where ν_i is the limiting molar ionic conductivity of the ion species i and c_i is the concentration of the ion species i. Therefore an estimate of the concentration of ions in the dielectric can be derived from an estimate of the limiting molar conductivity of the ions in the material. For propylene carbonate for example the limiting molar conductivity varies between $8.3\,\Omega^{-1}\,\mathrm{cm}^2\,\mathrm{mol}^{-1}$ and $25.7\,\Omega^{-1}\,\mathrm{cm}^2\,\mathrm{mol}^{-1}$ (Matsuda, 1981).

The limiting molar conductivity is related to the ionic mobility of the ions via (Atkins and Paula, 2006).

$$\nu_i = z_i \mu_i F \tag{5.3}$$

Where F is Faradays constant, z_i is the charge number and μ_i is the mobility of ion species i. Note that also the drift velocity of the ions is related to the limiting molar ionic conductivity of the ions, since according to Griffiths (1999a)

$$v_{\mathrm{d},i} = \frac{J_i}{n_i q_i} \tag{5.4}$$

Where $v_{\mathrm{d},i}$ is the drift velocity of the ion species i, J_i is the ionic current density, n_i is the number of ions per unit volume, q_i is the charge per ion for ion species i in Coulomb. And this current density of course is related to the conductivity and the electric field

$$J_i = \sigma_i E \tag{5.5}$$

Where σ_i is the conductivity due to a specific ion species and E is the electric field. Now when equation 5.2, 5.4 and 5.5 are combined and the molar concentration is rewritten to the number of ions per volume the following relation can be obtained

$$\begin{aligned} v_{\mathrm{d,i}} &= \frac{\nu_i c_i E}{n_i q_i} \\ &= \frac{\nu_i n_i E}{A_g n_i q_i} \\ &= \frac{\nu_i}{A_g q_i} E \end{aligned} \tag{5.6}$$

Where $v_{\mathrm{d,i}}$ is the drift velocity of the ions, ν_i is the limiting molar ionic conductivity, A_g is Avogadros constant, q_i is the charge per ion in coulomb and E is the electric field. This relation can be used to get a qualitative understanding of the movement of the ions.

- **R3** is the resistance due to charge transfer (with the unit Ω). The resistance is due to the energy loss of the chemical reactions that occurs at the electrode.

  The charge transfer resistance R_c(with the unit $\Omega\,\mathrm{m}^2$) is defined as the resistance due to charge transfer (with the unit Ω) times the electrode area.

  $$R_c = R3A \tag{5.7}$$

  Where R_C is the charge transfer resistance and A is the electrode area. In case the overpotential over the electrode is very small and the reaction is at equilibrium, the charge transfer resistance can be calculated using (Gamry Instruments, 2017; Horvai, 1991):

  $$R_c = \frac{RT}{zF j_0} \tag{5.8}$$

  Where R_c is the charge transfer resistance, R is the gas constant, T is the absolute temperature, z is the charge of the ion, F is Faradays constant and j_0 is the exchange current density. Therefore the exchange current density combined with the charge of the ion $z j_0$ can be determined, which gives an indication of the rate at which the chemical reactions occur at the electrodes when no potential is applied (Atkins and Paula, 2006). This value is expected to depend on the used electrodes and the chemical reactions occurring at these electrodes.

- **R4** can be finite in case the electrodes are touching.

- **C1** is the geometrical capacitance which follows from the macroscopic Maxwell equations and which is related to the dielectric constant of the dielectric and the exact geometry of the device. In our situation the capacitance can be approximated using the parallel plate approximation.

  $$C = \frac{\epsilon_r \epsilon_0 A}{d} \tag{5.9}$$

  Therefore if the geometry of the sample is known the dielectric constant of the material can be calculated.

- The **CPE** (Constant Phase Element) is a model of the double layer capacitance. In practice the double layer is not a pure capacitance but an element with a constant phase. The impedance of a CPE element is described using:

$$Z_{\text{CPE}} = \frac{1}{Q}(i\omega)^{-n} \tag{5.10}$$

With Q and n real positive constants. The reason for deviation of the double layer form a real capacitor might be that the electrode is shaped like a fractal (Liu et al., 1986). The CPE element can therefore also be seen as a frequency dependent resistance in series with a frequency dependent capacitance, with:

$$\begin{aligned} R(\omega) &= \frac{1}{Q\omega^n}\cos\left(\frac{\pi}{2}ni\right) \\ C(\omega) &= \frac{Q}{\omega^{1-n}\sin\left(\frac{\pi}{2}ni\right)} \end{aligned} \tag{5.11}$$

An estimate of the impedance of the double layer can be obtained by using a parallel plate approximation and the Debye length as an estimate of the thickness of the double layer. The Debye length can be calculated using the following equation (Russel et al., 1989).

$$\lambda = \sqrt{\frac{\epsilon_r \epsilon_0 k_{\text{B}} T}{2 N_A e^2 I}} \tag{5.12}$$

Where ϵ_r is the relative dielectric constant of the medium, ϵ_0 is the vacuum permittivity, k_{B} is the boltzmann constant, T is the absolute temperature, N_A is Avogadro's constant, e is the electron charge and I is the ionic strength of the medium defined as:

$$I = \tfrac{1}{2}\sum_{i=1}^{n} c_i z_i^2 \tag{5.13}$$

With c_i the concentration and z_i the charge of ion species i. Therefore also an estimate of the concentration of ions in the liquid can be made based on the imaginary part of the double layer at a certain frequency.

- The **W1** is a Warburg element that models the diffusion to and from an electrode (Bondarenko and Ragoisha, 2008). A Warburg element is a constant phase element with a phase of $-\frac{\pi}{2}$. The impedance can be described using the following equation:

$$Z_{\text{W}} = \frac{W}{\sqrt{\omega}} - \frac{W}{\sqrt{\omega}}i \tag{5.14}$$

Methods and Materials

To measure the impedance of the materials, the samples described in section 4.5.1 are placed in the modified resistivity adaptor shown in figure 5.2 and 5.3.

This resistivity adaptor is located in a metal case and is connected to a HP4284A LCR meter, using four coaxial cables. The two shielded BNC cables of the low and the high side are joined using a BNC T splitter on the coax connector of the resistivity adaptor.

Figure 5.2: A picture of the modified resistivity adaptor

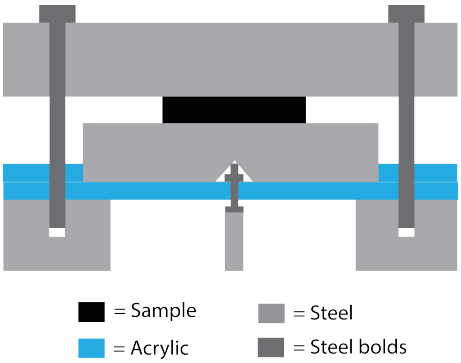

Figure 5.3: A drawing of the modified resistivity adaptor

The thickness of the samples is measured using a digital caliper. In the calculations the average thickness of all samples of a specific material is used. Note that the thickness of the material cannot be measured after the material has been placed inside the modified resistivity adaptor. However due to the high friction coefficient of the rubber like materials on the steel of the adaptor and the incompressibility of the materials, the thickness of the materials is not expected to change when they are placed in the adaptor.

Data analysis

The model has to be fit to the measured spectrum and has to be verified. In this section the methods used to do so are described.

KK check Before the model is fit to the measured data the quality of the data has to be checked. This is done by performing several consecutive measurements and by applying the KK check.

The mathematical basis for the KK check are the Kronig-Kramers relations which give a relation between the real and the imaginary parts the impedance of the sample for a causal, linear, stable and finite system.

$$\begin{aligned} Z_{re}(\omega) &= R_\infty + \frac{2}{\pi}\int_0^\infty \frac{xZ_{im}(x) - \omega Z_{im}(\omega)}{x^2 - \omega^2} dx \\ Z_{im}(\omega) &= \frac{2\omega}{\pi}\int_0^\infty \frac{Z_{re}(x) - Z_{re}(\omega)}{x^2 - \omega^2} dx \end{aligned} \tag{5.15}$$

To verify this, however requires the real and the imaginary part to be known at all frequencies. Boukamp (1995) therefore proposed a more practical check that involves fitting a circuit consisting of capacitor-resistor pairs with a fixed -3 dB frequency and one resistor in series (see

figure 5.4) to either the imaginary or the real part of the measured data. The −3 dB frequencies are chosen such that they are evenly distributed over the fitted frequency spectrum.

The part of the measured data that is not fitted to the circuit is then compared with the spectrum of the circuit. If there is only a random error in between the two spectra then the spectrum passes the KK-check and is expected to be causal, linear,stable and finite.

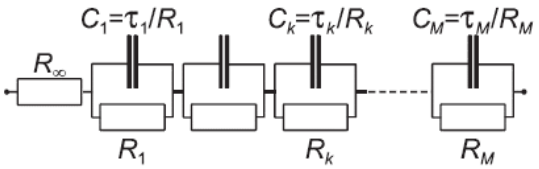

Figure 5.4: The schematic used for the kk-check, image courtesy of Boukamp (1995)

As described by Schonleber et al. (2014) the number of RC-elements that is used to fit in the model has a large influence on if the data passes the test. When to few element are used the data cannot be fitted correctly. When too many elements are used the data is fitted perfectly to one part of the spectrum. However in this case also the noise in this spectrum is fitted and this makes that the other part does never fit the model. This results in false negatives. They therefore propose a set of criteria to select the correct number of elements. These criteria are implemented in the LIN-KK tool (Karlsruhe Institute of Technology, 2017) and therefore this tool is used for the analysis.

Data fitting The data is fit using Matlab's "lsqnonlin" function using the trust-region-reflective algorithm. This function determines the parameters that minimise the output of a function. In order to use this fitting algorithm, a function that calculates the error is required. The error returned by this function should be independent of the magnitude of the signal. The function used in this analysis consists of error functions for the real and the imaginary parts.

$$\begin{aligned} f_{\mathrm{Re}}(\mathbf{p},\omega_n) &= \left|\log\frac{\mathrm{Re}(Z(\omega_n))}{\mathrm{Re}(Z_{\mathrm{m}}(\mathbf{p},\omega_n))}\right| \\ f_{\mathrm{Im}}(\mathbf{p},\omega_n) &= \left|\log\frac{\mathrm{Im}(Z(\omega_n))}{\mathrm{Im}(Z_{\mathrm{m}}(\mathbf{p},\omega_n))}\right| \end{aligned} \tag{5.16}$$

Where $Z(\omega_n)$ is the measured spectrum at the radial frequency ω_n and $Z_m(\mathbf{p},\omega_n)$ is the impedance calculated using the parameters $\mathbf{p}$ and radial frequency ω_n. The total function returns a vector which consists of a combination of the real and the imaginary parts.

$$\mathbf{f}(\mathbf{p},\boldsymbol{\omega}) = \begin{bmatrix} f_{\mathrm{Re}}(\mathbf{p},\omega_1) \\ f_{\mathrm{Re}}(\mathbf{p},\omega_2) \\ \cdots \\ f_{\mathrm{Re}}(\mathbf{p},\omega_n) \\ f_{\mathrm{Im}}(\mathbf{p},\omega_1) \\ f_{\mathrm{Im}}(\mathbf{p},\omega_2) \\ \cdots \\ f_{\mathrm{Im}}(\mathbf{p},\omega_n) \end{bmatrix} \tag{5.17}$$

The co-variance matrix describing the error in the parameters and their correlation is obtained using the following equation (Kutner et al., 2004).

$$\sigma^2 = \mathrm{MSE}\,(J^T J)^{-1} \tag{5.18}$$

Where σ^2 is the co-variance matrix and J is the Jacobi-matrix of the function f in equation 5.17 to parameters p. Jacobi-matrix is defined as.

$$J = \begin{bmatrix} \frac{\partial f_1}{\partial p_1} & \frac{\partial f_1}{\partial p_2} & \cdots & \frac{\partial f_1}{\partial p_m} \\ \frac{\partial f_2}{\partial p_1} & \frac{\partial f_2}{\partial p_2} & \cdots & \frac{\partial f_2}{\partial p_m} \\ \vdots & \vdots & \ddots & \vdots \\ \frac{\partial f_n}{\partial p_1} & \frac{\partial f_n}{\partial p_2} & \cdots & \frac{\partial f_n}{\partial p_m} \end{bmatrix} \tag{5.19}$$

Where f_n is the n-th element of f and p_m the m-th parameter. While the mean squared error (MSE) is defined as the squared sum of the residual and the residual is equal to the value of f in equation 5.17 at the fitted parameters p_{fit}

$$MSE = \sum_{1}^{n} f_n(\mathbf{p}_{\text{fit}}, \omega_n)^2 \tag{5.20}$$

At last, the standard deviation in the parameters can found by taking the square root of the variance of the parameters that can be found at the diagonal of the co-variance matrix.

5.2.2 Cyclic voltammetry

A way to analyse the electrochemical properties of a material is by cyclic voltammetry experiments. In this experiment a low frequent triangle shaped voltage is applied to the sample.

Background

Many chemical process only occur above a certain voltage, therefore a nonlinear shape of the curve will indicate a chemical reaction. Furthermore if the reaction is due to a limited number of impurities in the material, the current will reduce after all these impurities have reacted. The fact that the experiment is cyclic makes that the repeatability of the experiment can easily be evaluated.

Methods and Materials

In this experiment a sample is placed in the modified resistivity adaptor (see figure 5.2) and a low frequent triangle wave (see figure 5.5) is applied using a Keithley 2410 Source Measurement Unit.

The experiment will be performed using steel electrodes since the printed electrodes were incompatible with the used plasticizer as described in Section 4.5.1. Different reactions might occur when different electrodes are used.

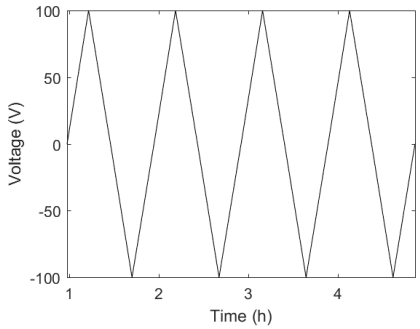

Figure 5.5: An example of the applied low frequent triangle wave

5.2.3 Electrode resistance measurement

During the fabrication of the test samples it was noticed that the resistance of the used PI-ETPU 85-700+ changed during the process. This was the reason for a separate investigation of the change in electrode resistance due to baking and plasticising.

Methods and Materials

The experiment is performed on disks that were 500 µm thick, 52 mm in diameter and which were described in section 4.5.1. The resistance is measured on the top side (the side that was not on the print bed) along six lines through the centre of the circle, see figure 5.6.

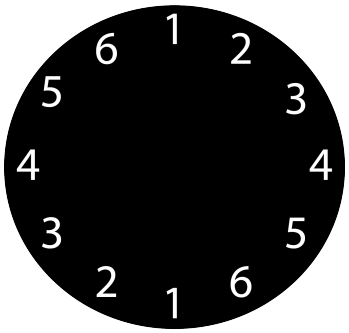

Figure 5.6: The 6 six locations on the sample in between which resistance measurements were performed

The measurement was performed using the auto resistance mode of a Keithley 2410 Source Measurement Unit in 2-wire mode. The measurement was performed using banana cables.

The reason for using a 2 wire measurement is that the resistivity of the material is not expected to be isotropic or uniform. Therefore also a 4-wire measurement would not give enough information to calculate the resistivity distribution of the material and therefore the additional complexity of this measurement does not outweigh the benefit.

The samples are baked by placing them on a borosilicate glass plate in the center of an oven at 150 °C. The samples were plasticized by placing them in a glass beaker with Propylene Carbonate for one night. The process used to the samples rest consisted of placing the samples on a table under a normal atmosphere and at room temperature.

5.3 Mechanical characterisation

In this section the mechanical characterisation of the conductor and the dielectric will be described. The mechanical characterisation will consist a measurement of the elasticity of the materials, which has an influence on the total strain of the actuator.

5.3.1 Elasticity measurement

An important parameter of the used dielectrics and conductors is their Young's modulus. In this section a measurement of the Young's modulus of the material when compressed in the $z-$direction and when extended in the $y-$direction is described.

Background

3D printed materials generally don't show the same properties in all directions, they are anisotropic, as a result of the printing process. The elasticity therefore should be described using the following matrix (Code Aster, 2017):

$$\begin{bmatrix} \epsilon_{xx} \\ \epsilon_{yy} \\ \epsilon_{zz} \\ 2\epsilon_{xy} \\ 2\epsilon_{xz} \\ 2\epsilon_{yz} \end{bmatrix} = \begin{bmatrix} \frac{1}{E_x} & -\frac{\nu_{yx}}{E_y} & -\frac{\nu_{zx}}{E_z} & 0 & 0 & 0 \\ -\frac{\nu_{xy}}{E_x} & \frac{1}{E_y} & -\frac{\nu_{zy}}{E_z} & 0 & 0 & 0 \\ -\frac{\nu_{xz}}{E_x} & -\frac{\nu_{yz}}{E_y} & \frac{1}{E_z} & 0 & 0 & 0 \\ 0 & 0 & 0 & \frac{1}{G_{xy}} & 0 & 0 \\ 0 & 0 & 0 & 0 & \frac{1}{G_{xz}} & 0 \\ 0 & 0 & 0 & 0 & 0 & \frac{1}{G_{yz}} \end{bmatrix} \begin{bmatrix} \sigma_{xx} \\ \sigma_{yy} \\ \sigma_{zz} \\ \sigma_{xy} \\ \sigma_{xz} \\ \sigma_{yz} \end{bmatrix} \tag{5.21}$$

Where:

- ϵ_{uu} is the strain in the $u-$direction
- ϵ_{uv} is the shear strain on the plane perpendicular to u in the $v-$direction
- E_u is the Youngs modulus in the direction u
- G_{uv} is the modulus of rigidity in the plane (u, v)
- ν_{uv} is the poisson ratio in the plane (u, v)
- σ_{uu} is the stress in the $u-$direction
- σ_{uv} is the shear stress on the plane perpendicular to u in the direction v

The soft materials used in this work generally have a Poison's ratio that is close to 0.5. Therefore in order to only measure the Young's modulus in the $z-$direction, care should be taken such that only a σ_{zz} stress is applied such that the third row in the matrix can be reduced. This can be done by making sure the stress in the $x-$ and the $y-$direction is negligible. In this case:

$$\begin{aligned} \epsilon_{zz} &= -\frac{\nu_{xz}}{E_x}\sigma_{xx} - \frac{\nu_{yz}}{E_y}\sigma_{yy} + \frac{1}{E_z}\sigma_{zz} \\ &= \frac{\sigma_{zz}}{E_z} \end{aligned} \tag{5.22}$$

For the same reason when measuring the Young's modulus in the $y-$direction, the stress in the $y-$ and the $z-$direction should be negligible for the measured stiffness to be exclusively dependent on the Young's modulus in the $y-$direction.

$$\begin{aligned} \epsilon_{yy} &= -\frac{\nu_{xz}}{E_x}\sigma_{xx} + \frac{\nu_{yz}}{E_y}\sigma_{yy} - \frac{1}{E_z}\sigma_{zz} \\ &= \frac{\sigma_{yy}}{E_y} \end{aligned} \tag{5.23}$$

Furthermore the behaviour of the material will be evaluated at different frequencies in order to be able to see if the Young's modulus is frequency dependent in the used frequency range. To evaluate the material at different frequencies a sinusoidal excitation with 10 different frequencies will be applied for a total of 40 periods.

Methods and Materials

Since PC was found to act as a plasticizer to the TPU based materials, the Young's modulus of the materials is also tested after the materials have been soaked in PC

$y-$direction setup To measure the Young's modulus in the $y-$direction the Young's modulus test piece (see section 4.5.2), is stretched in the y print direction, which is the direction in which the sample is 40 mm long. To stretch the sample, a linear actuator (SMAC LCA25-050-15F) is used. The mass of the axis of the actuator is 131 g. The maximum displacement d is 2 mm, and the highest frequency is 2 Hz. The maximum force exerted by the inertia of the axis can be calculated using the following relation:

$$\begin{aligned} F &= ma \\ &= m\frac{\partial^2}{\partial t^2}(d\cos(2\pi f t) \\ &= -md(2\pi f)^2\cos(2\pi f t) \end{aligned} \tag{5.24}$$

Where m is the mass of the axis and f is the oscillation frequency. Therefore the maximum force exerted by the inertia is 41 mg, which is much smaller as the applied force of 3 N. Also manual movement of the actuator axis gave the impression that there is no significant friction. Therefore influence of friction on the measurements will be neglected as well as the influence of the inertia of the axis of the actuator.

The sample is clamped at both ends. A schematic drawing of the setup can be found in figure 5.8. A picture of the actual setup can be found in Figure 5.10.

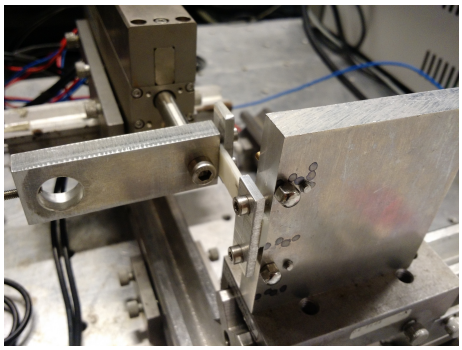

Figure 5.7: A picture of the used setup

Figure 5.8: A schematic image of the used setup

$z-$direction setup To measure the Young's modulus in the $z-$direction a well defined force is applied to the Young's modulus test pieces using a linear actuator (SMAC LCA25-050-15F), see figure 5.9. The applied force and the displacement as measured by the SMAC actuator are used.

The piece of material is placed in between Teflon sheets greased with silicone oil in order to reduce the friction of the material with the actuator tip and the table. This is done to make sure

that there is no stress in the $x-$ an $y-$direction, such that the simplification of equation 5.22 holds. Since the weight (98 g) and the displacement of the moving axis of the actuator are even lower in this measurement, the inertia of the axis also can be neglected in this measurement .

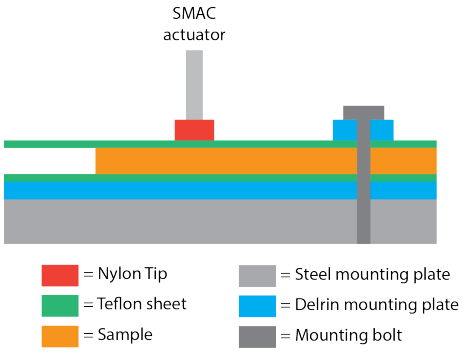

Figure 5.9: A schematic image of the used setup

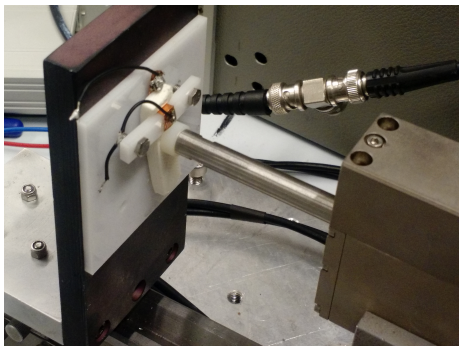

Figure 5.10: A picture of the used setup

This test is only applied to the most flexible materials (X60 and Lay Fomm 40) since only for these materials the displacement is large enough to measure with the encoder of the SMAC actuator, which has a resolution of 5 µm

Data analysis

During the measurement a sinusoidal force and displacement is measured. To calculate the Young's modulus of the material, the RMS values of the force and the displacement should be determined. Furthermore the phase shift in between the force and displacement signal will be determined, since this could give information about the losses in the material.

The data generated by the measurement does not have a uniform sampling time. Therefore the data is interpolated using a linear interpolation on a timescale with a sampling time which is thirty times smaller than the average sampling time of the measurement.

This data is Fourier transformed using a Fast Fourier Transform using a rectangular windowing function. The signal is filtered by only keeping the bins corresponding to the excitation frequency and the 5 bins closest to this frequency.

To calculate the Young's modulus of the material, the Fourier transform of the filtered signals is back transformed using an inverse Fast Fourier transform. Next the RMS value of the filtered force signal is divided by the RMS value of the measured displacement signal.

The phase difference in between the force and the position signal is computed using a cross correlation of both signals. The cross correlation of the signals is computed by using the fol-

lowing relation, since it allows the cross correlation to be computed much faster as by using Matlab's "xcov" function (Weisstein, 2017a).

$$f \star g = \mathscr{F}\left[\bar{F}G\right] \tag{5.25}$$

Where $\star$ is used for the cross correlation, $\mathscr{F}$ is used for the Fourier transform, G is the Fourier transform of $g$and $\bar{F}$ is the complex conjugate of the Fourier transform of f. Using this relation the cyclic cross correlation can be calculated using a Fourier Transform of a product of the filtered Fourier transforms. The phase difference between the signal is determined by finding the time shift that corresponds to the maximum value in the cross correlation, for the part of the cross correlation where the time shift is smaller as one period of the signal. This since it is expected that the system is causal and that the phase shift is smaller than 2π.

5.4 Device characterisation

As a proof of concept a cantilever shaped actuator was made. To prove that this proof of concept is working the deflection of the cantilever will be measured using a laser Doppler vibrometer. To get the largest deflection the cantilever will be driven at it's oscillation frequency.

5.4.1 Laser Doppler vibrometer measurement

The cantilever described in section 4.5.3 will be exited with a sinusoidal voltage with an amplitude of 50 V and a DC offset of 50 V. This is the largest signal that could be generated using the available amplifier. The displacement of the cantilever will be measured using the Polytec MSA-400 scanning laser-doppler vibrometer. The position measurement was performed at a single spot on the tip of the cantilever. At this spot an Edding 751 paint marker will be used to paint a cross on the cantilever to increase the reflection of the sample. A schematic drawing of the setup can be found in Figure 5.11, a picture of the setup can be found in figure 5.12.

The measurement consists of two parts. First the oscillation frequency of the sample will be determined by applying a chirp signal to the sample. A chirp signal is a sinusoidal of which the frequency is increased. The Fourier transform of the measured signal will therefore contain the response to a wide range of frequencies. The second part consists of a measurement of the response when the sample is excited using a sinusoidal excitation at the oscillation frequency.

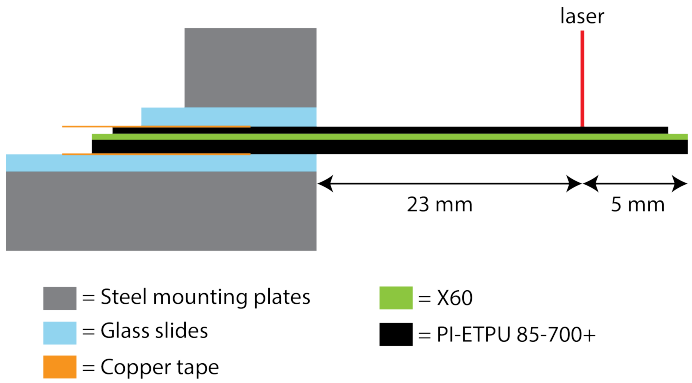

Figure 5.11: A drawing of the setup in which the cantilever movement is measured

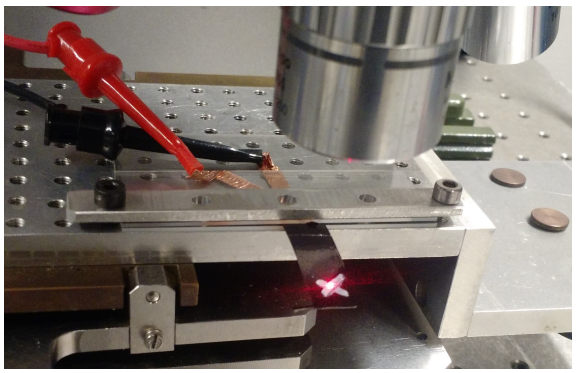

Figure 5.12: A picture of the setup in which the cantilever movement is measured

Expected oscillation Frequency

The neutral axis of the cantilever can be calculated using equation H.3, the geometry described in section 4.5.3 and by using a Young's modulus for PI-ETPU of 20 MPa and 6 MPa for X60 (see section 6.3.1). In this case the neutral axis is located at 191 µm from the bottom of the sample ($y_0 = 191\,\mu m$).

As described in Appendix H the lowest resonance frequency for an undamped cantilever can be calculated using the following equation.

$$f_1 = \frac{1}{2\pi}\sqrt{1.875^4 \frac{S}{\lambda L^4}} \tag{5.26}$$

Where S is the total moment per curvature (see equation H.5) and λ is the mass per unit of length. S can be calculated using equation H.5. With E_i the Young's modulus of material i and I the second moment of area of the material, relative to the neutral axis. When using the same Young's moduli for PI-ETPU and X60 as before and the previously calculated neutral axis, the moment per unit curvature for this cantilever is $1.06\,\mu N\,m^2$.

The mass per unit length, λ, can be calculated using equation H.7. In this calculation an estimate of the density of PI-ETPU 85-700+ based on the density of PI-ETPU 95-250, which is $1300\,kg\,m^{-3}$ (Palmiga Innovations, 2017) will be used. The density of X60 will be based on the density of Ninjaflex, which is $1200\,kg\,m^{-3}$ (Ninjatek, 2017). Using these densities and the geometry described in section 4.5.3 a mass per unit length of $5.5\,g\,m^{-1}$ is obtained.

This results in an estimate for the first eigen frequency of 9.9 Hz.

5.5 Conclusion

The described measurements are expected to be able to measure the dielectric constant, Young's modulus and the ion concentration of the tested materials. Also the presence of chemical reaction and how long they continue will be measured, however the voltametry experiment will be performed using stainless steel electrodes since the printed electrodes were incompatible with the used plasticizer as described in Section 4.5.1. This may result in different reactions as when 3D printed electrodes are used. Furthermore the resistance of the conductor will be determined. The dielectric strength of the materials will not be determined. At last the deflection of the proof of concept actuator will be determined using the laser Doppler vibrometer experiment.

6 Results

6.1 Introduction

In this section the results of the measurements described in section 5 will be discussed. The goal of the measurements is to measure the dielectric constant, Young's modulus and ion concentration of several dielectrics. An attempt will be made to measure the presence of chemical reactions and how long they will continue when the dielectrics are placed in between stainless steel electrodes. Also the resistance of the 3D printed conductive material will be discussed. At last the measured deflection of the proof of concept cantilever-actuator will be discussed.

6.2 Electrical characterisation

6.2.1 Impedance spectroscopy

In this section the results of the impedance spectroscopy experiment described in Section 5.2.1 on the samples described in Section 4.5.1 are described. For every material the spectrum has been measured using multiple frequency sweeps. The last of these sweeps is checked for time independence using a kk-check and is fitted to the model in Figure 5.1.

The spectrum of each material is measured before and after the material is plasticised by PC. The plasticised material is measured both with and without a DC offset in the applied signal.

For example the spectra measured on X60 plasticised using PC without using a DC offset can be found in Figure 6.1. The result of the kk-check on the last measurement can be found in Figure 6.2. The fit on the last measurement is shown in Figure 6.3 and the difference in between the fit and the measurement is shown in Figure 6.4. Similar figures have been made for each fit and these figures can be found in Appendix L.

The dielectric constant, Ionic Conductivity, Exchange current density and Ionic strength are calculated using the equations described in Section 5.2.1, the values in Table L.1, the average thickness of the samples and the macroscopic area of the electrodes. The Debye length and the Ionic strength are estimated based on the equivalent series capacitance of the CPE at 1 mHz. In the estimation of the Ionic strength the fitted relative dielectric constant is used.

The physical meaning of the different elements is summarised in Table 6.1. The physical meaning of the geometrically independent parameters can be found in Table 6.2. The average thickness of the different samples that are used in the calculation of the geometry independent variables can be found in Table 6.3.

Table 6.1: Physical meaning of the fitted parameters

Parameter	Physical Meaning
R1	Electrode resistance
R2	Ionic resistance
R3	Resistance due to charge transfer
R4	Electronic resistance
C1	Geometrical capacitance
Q	Double layer impedance
n	Double layer impedance
W	Diffusion

Table 6.2: Physical meaning of the geometry independent parameters

Symbol	Physical Meaning
ρ	Electronic resistivity
σ	Ionic conductivity
zj_0	Exchange Current density
ϵ_r	Dielectric Constant
λ	Debye Length
I	Ionic strength

Table 6.3: Average thickness of the different samples

Material	Without PC	With PC
X60	430 µm	500 µm
Ninjaflex	490 µm	590 µm
PI-ETPU 85-700+	480 µm	540 µm

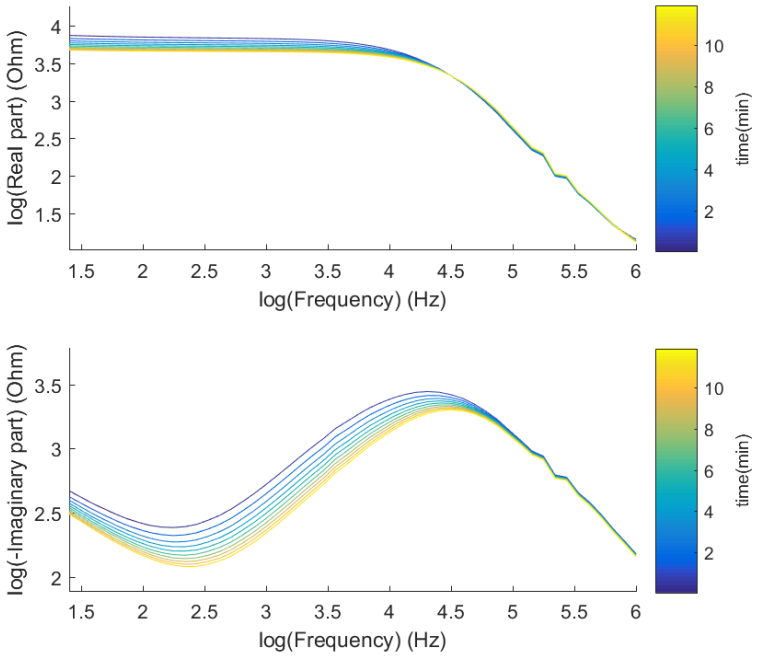

Figure 6.1: Drift in the measured spectrum on X60 without offset and PC

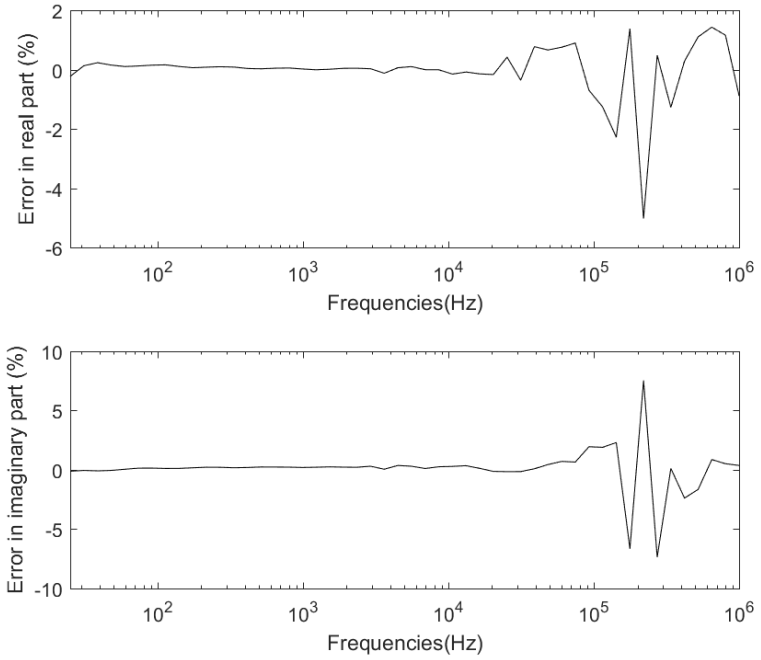

Figure 6.2: kk-check on the last measured spectrum on X60 without offset and PC

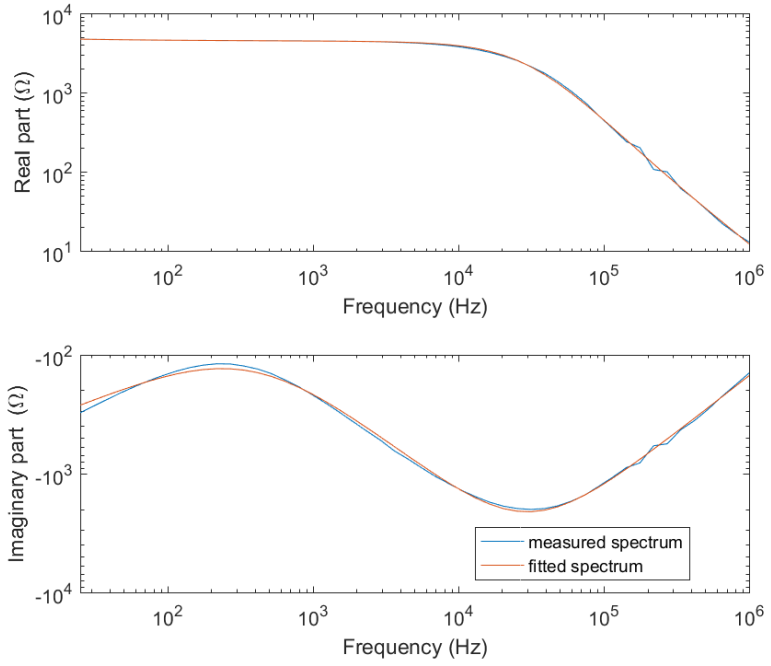

Figure 6.3: Last spectrum measured on X60 without offset and PC and the spectrum that was fitted to it

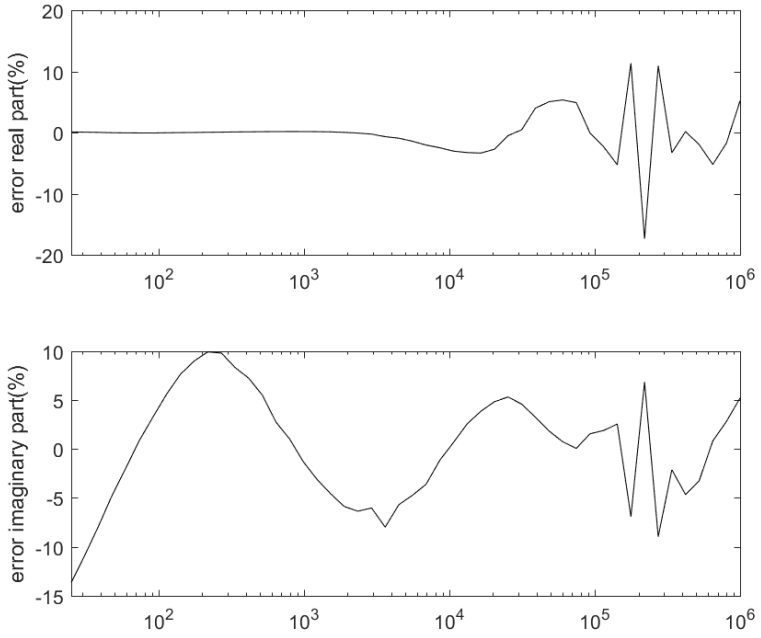

Figure 6.4: Error in between the measured and fitted spectrum of X60 without offset and PC

X60

The parameters fitted to the spectra of X60 can be found in Table 6.4. Some geometry independent variables derived from these parameters can be found in figure 6.5. More information relating the fitting process can be found in appendix L.

The not plasticised material has a relative dielectric constant of around 5. The material has a real part that corresponds to a Randles circuit with a double layer with a thickness of around 900 µm and a ionic conductivity of 1.3 $m\Omega\,m^{-1}$. There is no significant difference in between the response of the material when an offset is applied and when no offset is applied.

The plasticised material has a higher relative dielectric constant of around 30. The plasticizer did also increase the resistive loss, which made that the part fitted better to a Randles circuit with a smaller double layer and a larger exchange current density. The double layer thickness however increases and the exchange current density decreases when an offset is applied to the measurement signal.

Table 6.4: parameters used to fit spectra of X60

Symbol	No Offset No PC	With Offset No PC	No Offset With PC	With Offset With PC
R1	0 Ω	0 Ω	0 Ω	0 Ω
R2	3.6 kΩ	3.68 kΩ	1 kΩ	3.14 kΩ
R3	62.4 MΩ	48.1 MΩ	3.47 kΩ	220 kΩ
R4	∞ Ω	∞ Ω	∞ Ω	∞ Ω
C1	200 pF	233 pF	1.01 nF	1.1 nF
Q	80.1 $p\Omega^{-1}rad^{-n}s^{n}$	88 $p\Omega^{-1}rad^{-n}s^{n}$	4.35 $n\Omega^{-1}rad^{-n}s^{n}$	4.05 $n\Omega^{-1}rad^{-n}s^{n}$
n	959 m	950 m	789 m	1×10^3 m
W	0 $\Omega rad^{-\frac{1}{2}}s^{-\frac{1}{2}}$	0 $\Omega rad^{-\frac{1}{2}}s^{-\frac{1}{2}}$	3.28 $k\Omega rad^{-\frac{1}{2}}s^{-\frac{1}{2}}$	2.18 $M\Omega rad^{-\frac{1}{2}}s^{-\frac{1}{2}}$

Table 6.5: Geometry independent parameters for X60

Symbol	No Offset No PC	With Offset No PC	No Offset With PC	With Offset With PC
ρ	$\infty\,\Omega\,m$	$\infty\,\Omega\,m$	$\infty\,\Omega\,m$	$\infty\,\Omega\,m$
σ	$1.31\,m\Omega\,m^{-1}$	$1.28\,m\Omega\,m^{-1}$	$4.05\,m\Omega\,m^{-1}$	$1.29\,m\Omega\,m^{-1}$
zj_0	$0\,A\,m^{-2}$	$0\,A\,m^{-2}$	$7.29\,\mu A\,m^{-2}$	$115\,nA\,m^{-2}$
ϵ_r	4.79	5.59	28	30.6
λ	$868\,\mu m$	$881\,\mu m$	$37.6\,\mu m$	$136\,\mu m$
I	$7.35\,pmol\,m^{-3}$	$8.34\,pmol\,m^{-3}$	$23\,nmol\,m^{-3}$	$1.93\,nmol\,m^{-3}$

PI-ETPU 85-700+

The parameters fitted to the spectra of PI-ETPU 85-700+ can be found in Table 6.6. Some geometry independent variables derived from these parameters can be found in figure 6.7. More information relating the fitting process can be found in appendix L.

The not plasticised material has a relative dielectric constant of 176 and a electronic resistivity of 7.43 Ω m. The plasticised material has a dielectric constant around 30 and can be modelled without using an electronic conductance, by using a Randles circuit with a double layer element with a low constant phase around 0.6.

Table 6.6: parameters used to fit spectra of PI-ETPU 85-700+

Symbol	No Offset No PC	No Offset With PC	With Offset With PC
R1	$0\,\Omega$	$0\,\Omega$	$0\,\Omega$
R2	$\infty\,\Omega$	$69.3\,\Omega$	$105\,\Omega$
R3	$\infty\,\Omega$	$26.4\,k\Omega$	$39.2\,k\Omega$
R4	$176\,\Omega$	$\infty\,\Omega$	$\infty\,\Omega$
C1	5.07 nF	977 pF	1.09 nF
Q	$\infty\,\Omega^{-1}rad^{-n}s^{n}$	$120\,n\Omega^{-1}rad^{-n}s^{n}$	$64.3\,n\Omega^{-1}rad^{-n}s^{n}$
n	1	576 m	683 m
W	$\infty\,\Omega rad^{-\frac{1}{2}}s^{-\frac{1}{2}}$	$8.04\,k\Omega rad^{-\frac{1}{2}}s^{-\frac{1}{2}}$	$1.62\,M\Omega rad^{-\frac{1}{2}}s^{-\frac{1}{2}}$

Table 6.7: Geometry independent parameters for PI-ETPU 85-700+

Symbol	No Offset No PC	No Offset With PC	With Offset With PC
ρ	$743\,\Omega\,m$	$\infty\,\Omega\,m$	$\infty\,\Omega\,m$
σ	$0\,\Omega^{-1}\,m^{-1}$	$58.5\,m\Omega\,m^{-1}$	$38.4\,m\Omega\,m^{-1}$
zj_0	$0\,A\,m^{-2}$	$958\,nA\,m^{-2}$	$645\,nA\,m^{-2}$
ϵ_r	136	27.2	30.3
λ	$\infty\,m$	372 nm	$1.49\,\mu m$
I	$0\,mol\,m^{-3}$	$228\,\mu mol\,m^{-3}$	$15.8\,\mu mol\,m^{-3}$

Ninjaflex

The parameters fitted to the spectra of Ninjaflex can be found in Table 6.6. Some geometry independent variables derived from these parameters can be found in figure 6.7. More information relating the fitting process can be found in appendix L.

The not plasticised material has a relative dielectric constant of about 5, the real part of the impedance of the material can be modelled using a Randles circuit with a thick double layer, much larger than the thickness of the sample.

The plasticised material has a dielectric constant around 20. When no offset is applied to the measurement signal, the material can be modelled using a Randles circuit with a double layer with a constant phase of 0.8. When an offset is applied the material can be modelled with a double layer with a constant phase around 0.6 and a much lower Exchange current density.

Table 6.8: parameters used to fit spectra of Ninjaflex

Symbol	No Offset No PC	No Offset With PC	With Offset With PC
R1	$0\,\Omega$	$0\,\Omega$	$0\,\Omega$
R2	$10.7\,k\Omega$	$1.01\,k\Omega$	$340\,\Omega$
R3	$242\,M\Omega$	$15.8\,k\Omega$	$1.25\,M\Omega$
R4	$\infty\,\Omega$	$\infty\,\Omega$	$\infty\,\Omega$
C1	$177\,pF$	$608\,pF$	$642\,pF$
Q	$67.5\,p\Omega^{-1}rad^{-n}s^{n}$	$1.1\,n\Omega^{-1}rad^{-n}s^{n}$	$25.9\,n\Omega^{-1}rad^{-n}s^{n}$
n	$937\,m$	$839\,m$	$600\,m$
W	$0\,\Omega rad^{-\frac{1}{2}}s^{-\frac{1}{2}}$	$6.81\,k\Omega rad^{-\frac{1}{2}}s^{-\frac{1}{2}}$	$116\,\Omega rad^{-\frac{1}{2}}s^{-\frac{1}{2}}$

Table 6.9: Geometry independent parameters for Ninjaflex

Symbol	No Offset No PC	No Offset With PC	With Offset With PC
ρ	$\infty\,\Omega m$	$\infty\,\Omega m$	$\infty\,\Omega m$
σ	$386\,\mu\Omega\,m^{-1}$	$3.42\,m\Omega\,m^{-1}$	$10.1\,m\Omega\,m^{-1}$
zj_0	$\infty\,A m^{-2}$	$1.6\,\mu A m^{-2}$	$20.2\,nA m^{-2}$
ϵ_r	4.85	20	21.1
λ	$931\,\mu m$	$139\,\mu m$	$1.56\,\mu m$
I	$6.48\,pmol\,m^{-3}$	$1.2\,nmol\,m^{-3}$	$10.1\,\mu mol\,m^{-3}$

Conclusion

The relative dielectric constant of X60 and Ninjaflex is around 5. The relative dielectric constant of PI-ETPU 85-700+ is above 100. After plasticising with propylene carbonate the relative dielectric constant of X60 and PI-ETPU changed to around 30 and the relative dielectric constant of Ninjaflex increased to around 20.

It was found that for the not plasticised dielectrics X60 and Ninjaflex the Randles circuit gives a good estimate of the dielectric loss with large double layer thicknesses in the order of 1 mm and conductivities in the order of $1\,m\Omega^{-1}\,m^{-1}$. The ionic conductivity of the dielectrics with and without propylene carbonate varies from $1\,m\Omega^{-1}\,m^{-1}$-$10\,m\Omega^{-1}\,m^{-1}$. However it should be noted that the error in the ionic resistance, based on the fit sometimes is large.

The plasticised materials can also be modelled using a Randles circuit. After applying an offset to the plasticised dielectrics X60 and PI-ETPU, the Exchange Current density in the fitted models decreased, implying that fewer chemical reactions took place at the electrodes. The exchange current density in PI-ETPU is relatively low in both the situation with and without an offset.

The electronic resistivity of PI-ETPU changes from $7.43\,\Omega cm$, to an immeasurable high value after being plasticised with Propylene carbonate.

The physical meaning of the fitted circuits remains unclear, since the Ion concentration following from Ionic conductivity and the limiting molar conductivity of some ions in Propylene Carbonate (Matsuda, 1981) is in between 0.15 $\mathrm{mol\,m^{-3}}$ and 70.5 $\mathrm{mol\,m^{-3}}$. While the Ion concentration that corresponds to the measured double layer thicknesses is in between 6.5 $\mathrm{pmol\,m^{-3}}$ and 228 $\mathrm{\mu mol\,m^{-3}}$.

6.2.2 Cyclic voltametry

This chapter contains the results obtained in the cyclic voltamery experiment described in section 5.2.2.

PI-ETPU 85-700+

A voltammogram of PI-ETPU plasticised using PC made at a speed of 22.7 $\mathrm{mV\,s^{-1}}$ up till 20 V is shown in figure 6.5. The first two cycles have not been plotted.

The current flowing through the sample when increasing the voltage over the sample appears to be larger than the current when the voltage is decreasing. Furthermore after increasing the voltage above 15 V the material stops behaving ohmic and the current starts to decrease. This behaviour can be seen at both the negative and the positive voltages and is repeatable.

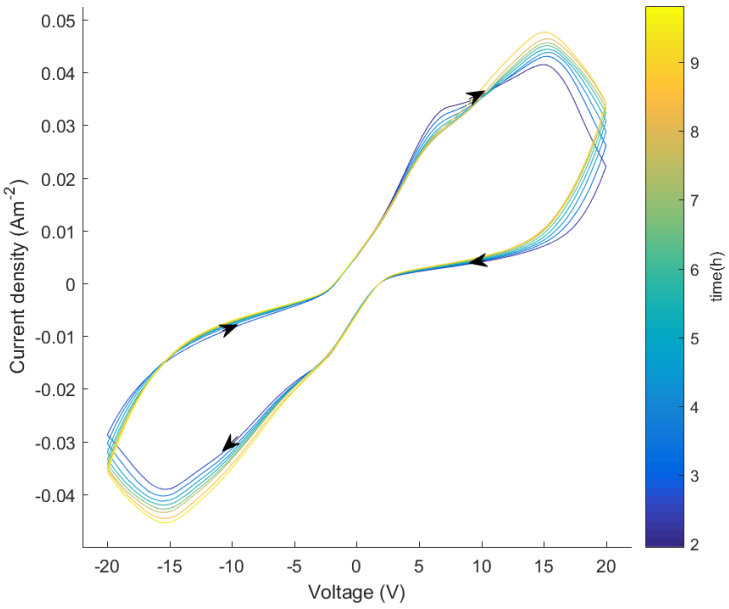

Figure 6.5: A cyclic voltammogram of PI-ETPU 85-700+ at 22.7 $\mathrm{mV\,s^{-1}}$

X60

A voltammogram of X60 made at a speed of 11.3 $\mathrm{mV\,s^{-1}}$ up till 30 V is shown in figure 6.7. The speed is reduced in attempt to get to get to a speed, where the assumption of an infinitely slow measurement holds. The first cycle has not been plotted. Again the current when increasing the voltage over the sample appears to be larger than the current when the voltage is decreased. This time the current stops following a Ohmic relationship after 11 V.

A voltammogram of X60 plasticised using PC made at a speed of 114.3 $\mathrm{mV\,s^{-1}}$ up till 100 V is shown in Figure 6.7, again the first cycle has not been plotted. The maximum voltage in this measurement has been increased in order to check that reduction in current measured in the previous experiment would continue at higher voltages

Again the current when increasing the voltage over the sample appears to be larger than the current when the voltage is decreased. When increasing the voltage the current stops following an ohmic relation above 8 V. This time however the current does not only decrease but shows a second peak around 55 V.

After the measurement the sample had changed colour from being completely white to white with orange spots. See figure 6.8

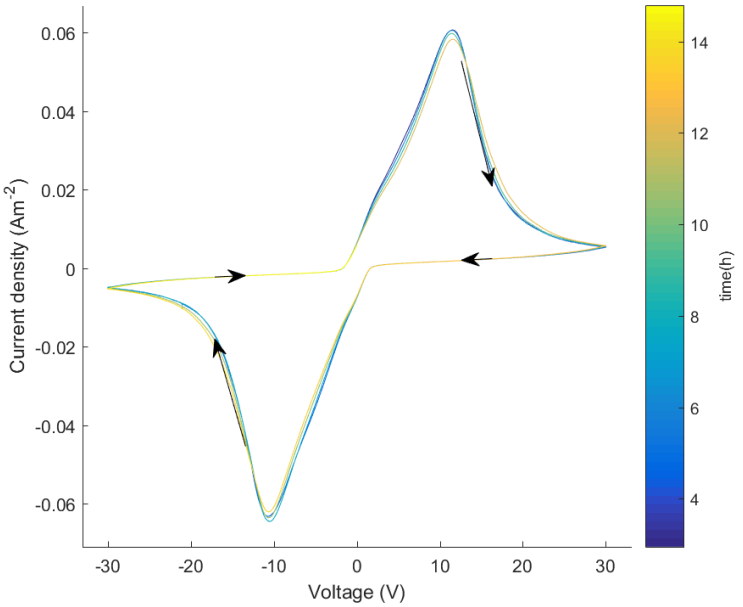

Figure 6.6: A cyclic voltammogram of X60 at 11.3 mVs^{-1}

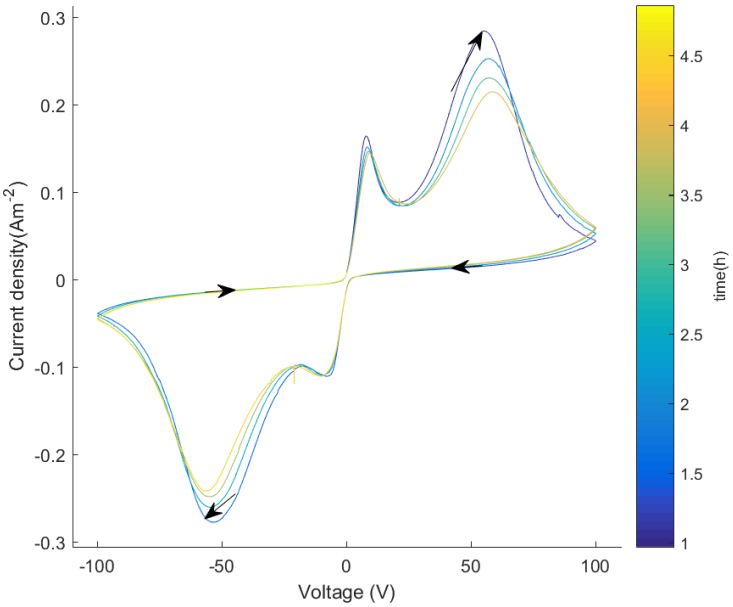

Figure 6.7: A cyclic voltammogram of X60 at 114.3 mVs^{-1}

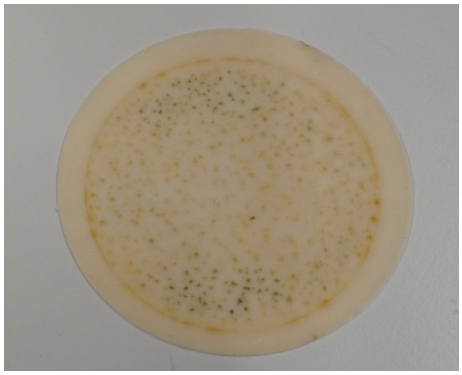

Figure 6.8: The colour change of the sample

Ninjaflex

A voltammogram of Ninjaflex plasticised using PC made at a speed of 11.3 mVs^{-1} up till 30 V is shown in figure 6.9. The first cycle has not been plotted. Again the current when increasing the voltage over the sample appears to be larger than the current when the voltage is decreased. When increasing the voltage the current stops following an ohmic relation above 4 V. There is a second increase in current around 25 V.

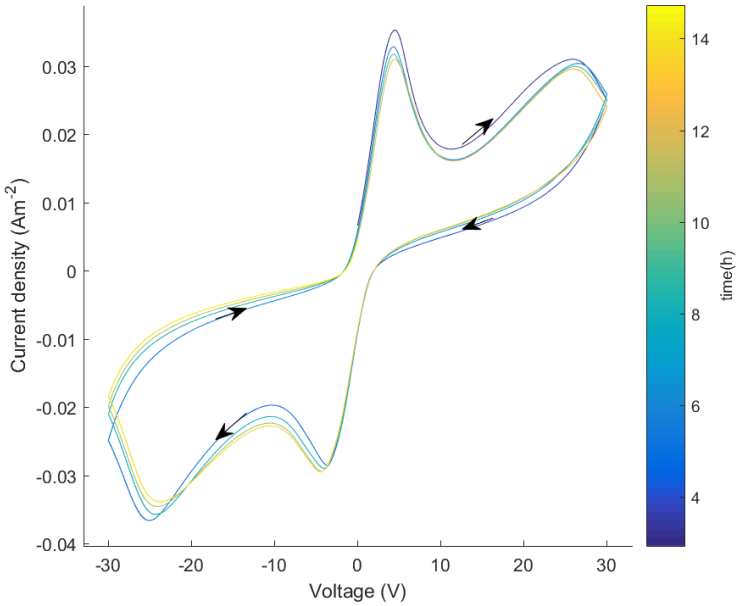

Figure 6.9: A cyclic voltammogram of Ninjaflex at 11.3 mVs^{-1}

Conclusion

All plots show a decrease in current for higher voltages. This might be since the ions that were present inside the material have now reacted at the electrodes. The repeatability of the measurements may be caused by these ions reacting back into the material when a reverse voltage is applied.

If this is the case, the material can be used in a dielectric elastomer actuator, as long as the material is polarised first and the voltage over the actuator is not reversed.

The double peak in Figure 6.6 and 6.9 may indicate that there is more than one reaction occurring. The second reaction might be corrosion of the electrodes, this may be checked by using

electrodes that do not corrode and are compatible with PC instead. This will require further research.

6.2.3 Resistance Measurement

In this section the results of the resistance measurement described in section 5.2.3 will be described. The average resistance and the standard deviation in the measured resistance after different treatments can be found in Table 6.10. The described treatments have been performed sequentially and are additional

Table 6.10: PI-ETPU 85-700+ resistance after different treatments for example baking at 150 °C and resting at room temperature

Treatment	number of samples	Resistance	standard deviation
Printing	3	49 kΩ	8 kΩ
16 h resting	3	40 kΩ	3.5 kΩ
30 min baking	3	12.6 kΩ	3.5 kΩ
30 min baking	3	9.3 kΩ	2.9 kΩ
120 min baking	3	5.2 kΩ	1.5 kΩ
16 h baking	3	580 Ω	220 Ω
8 h baking	3	410 Ω	180 Ω
16 h resting	2	420 Ω	89 Ω
plasticising	1	144 MΩ	13 MΩ
1 week resting	1	560 Ω	128 Ω

The resistance of the PI-ETPU sample appears to decrease over 2 decades when the material is baked at 150 °C. The resistance of the material does increase more than 5 orders when the material is plasticised. After the material is left to rest for a week the resistance returns to a resistance close to the value after baking.

Conclusion

It can be concluded that the resistance of the PI-ETPU sample decreases when placed in an oven at 150 °C and that the resistance increases when the material is plasticised. However, it is unclear if this is a change in the bulk resistivity of the material or if it is due to a change in the surface resistance. Further research is necessary to determine this.

6.3 Mechanical characterisation

6.3.1 Youngs modulus measurement

The Young's modulus of the samples described in section 4.5.2 has been measured for tensile strain in the $y-$direction and compressive strain in the $z-$direction as described in section 5.3.1.

Tensile Young's modulus in the $y-$direction

The tensile Young's modulus in $y-$direction for X60, PIETPU and Ninjaflex with and without plasticizer has been plotted in figure 6.10. Also the Young's modulus of LAY FOMM 40 when filled with water is plotted. The phase difference between the applied force and the measured position is plotted in figure 6.11.

The Young's moduli of not plasticised PI-ETPU and Ninjaflex, as well as the Young's modulus of LAY FOMM 40 filled with water, appears to increase for increasing Young's modulus. The increase in Young's modulus in this frequency range however is not more than 20 %.

There appears to be a decrease in the phase for higher frequencies, however the measured phase in this frequency range is always above -0.25 radians.

Compressive Young's modulus in the $z-$direction

The compressive Young's modulus in $z-$direction for different materials is plotted in figure 6.12. The phase difference between the applied force and the measured position is plotted in figure 6.13.

The Young's modulus of X60 appears to be much lower in the $y-$than in the $z-$direction, more than a factor 5. The difference is less for X60 plasticised with PC and LAY FOMM with water, but still the Young's modulus is a factor 2 smaller in the $z-$direction.

There appears to be a decrease in the phase for higher frequencies, however the measured phase in this frequency range is always above -0.35 radians.

Conclusion

The tensile Young's modulus in the $y-$ and the compressive Young's modulus in the $z-$direction for different 3d printed material has been determined, before and after they were plasticised.

There is a large difference between the measured tensile Young's modulus in $y-$direction and the compressive Young's modulus in the $z-$direction. This might be partly due to the fact that stress applied in both situations is different; a dynamic stress of 38 kPa is applied in the $z-$direction while a dynamic stress of 150 kPa is applied to most materials in $y-$direction.

There appears to be a small increase in Young's modulus with frequency for certain materials. However a measurement over a wider frequency range with a better phase measurement and a larger variation in stiffness is required in order to be able to say something about the underlying physics.

6.4 Device characterisation

6.4.1 Laser doppler vibrometer results

In this section the results of the measurement described in section 5.4.1 on the sample described in section 4.5.3 will be discussed. The mechanical response to the chirp signal with an amplitude of 50 V and an offset of 50 V can be found in Figure 6.14. This signal is filtered using a moving average filter with a width of 30 bins can also be found in this figure.

Using the laser Doppler vibrometer's software the resoneance frequency has been determined to be 16.4 Hz with a Q factor of 7.8. The phase plotted in this figure is the phase difference between the applied signal and the measured displacement.

The response to a sinusoidal signal at 15.9 Hz can be found in figure 6.15. The amplitude at the excitation frequency is 1.76 µm. The cantilever is not exited exactly at the resonance frequency since the oscillation frequency used in this measurement was determined by visual inspection of the graph instead of a numerical calculation.

In a static situation a deflection of the cantilever of 1.76 µm would store 0.7 pJ of mechanical energy in the cantilever. For a cantilever of 28 mm x 10 mm x 450 mm this corresponds to a work density of 5 µJ m^{-3}.

6.4.2 Conclusion

The laser Doppler vibrometer measurement shows that the cantilever has an eigenfrequency of 16.4 Hz. This is different from the expected eigenfrequency of 9.9 Hz. This deviation might be caused by some residual stress inside the cantilever due to the printing process, which was still noticeable after baking of the cantilever. This stress caused the cantilever to curl up slightly in both the $x-$ as the $y-$directions, increasing the stiffness of the cantilever. The deflection of the

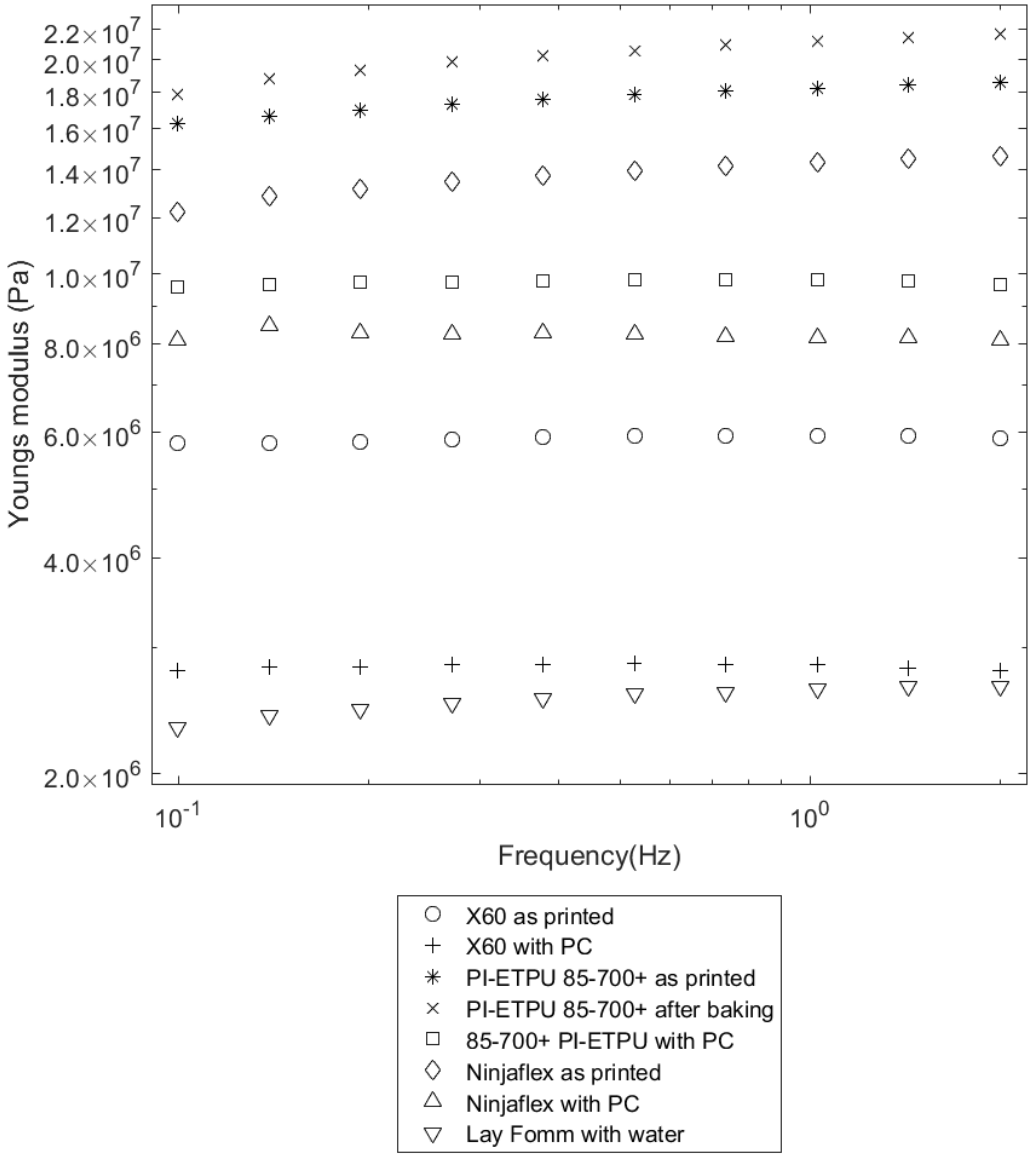

Figure 6.10: The tensile Young's modulus in the $y-$direction

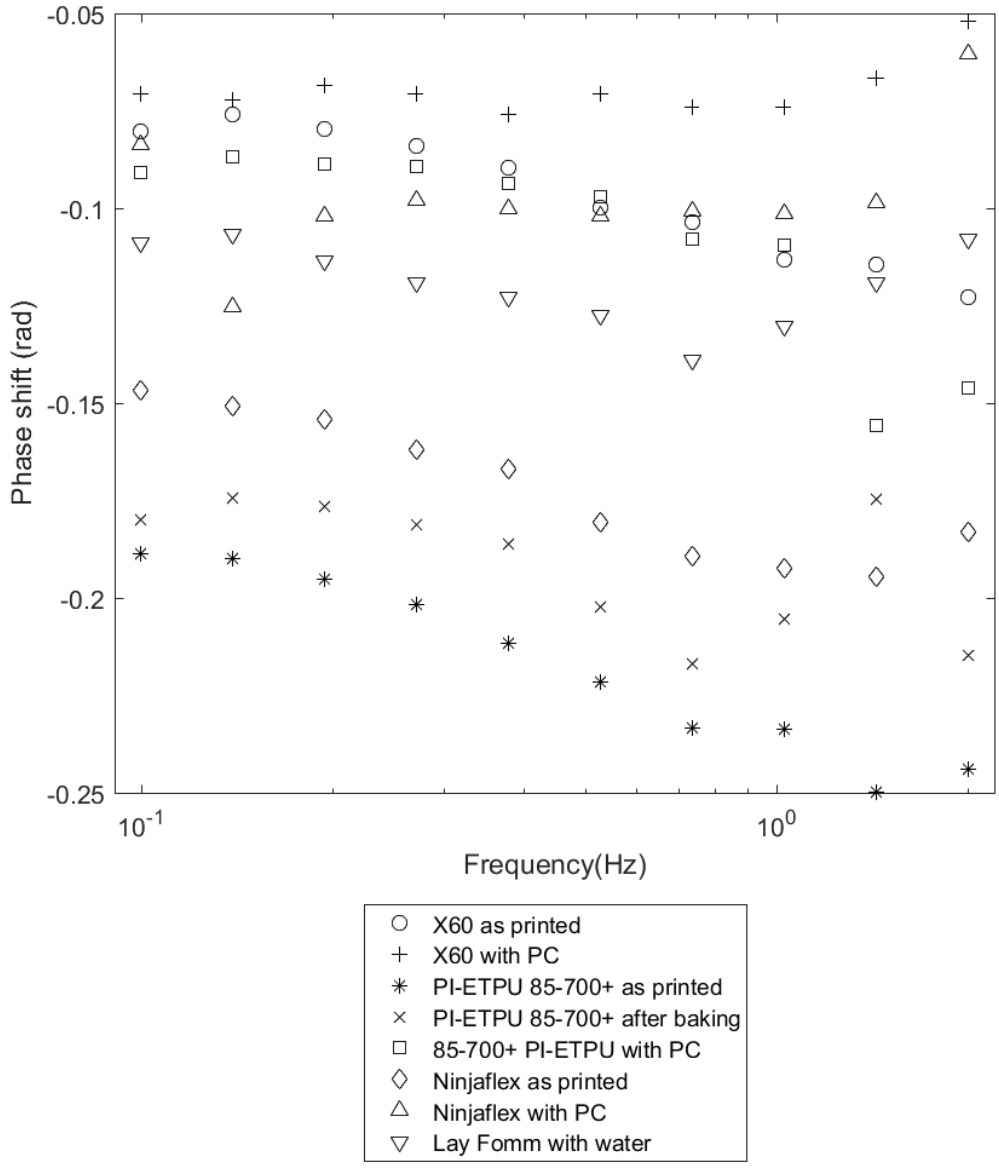

Figure 6.11: The phase shift of the position and the force in the tensile Young's modulus measurement in the $y-$direction

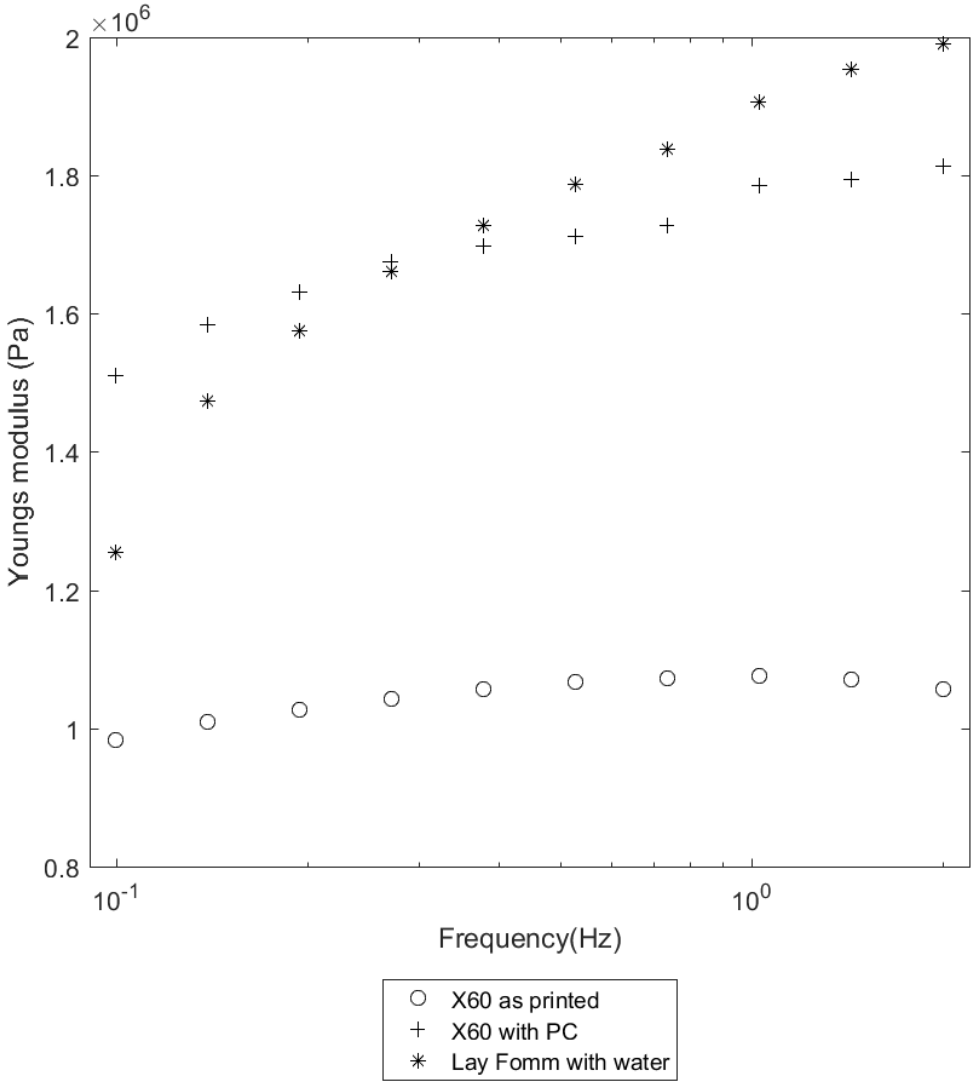

Figure 6.12: The compressive Young's modulus in the $z-$direction

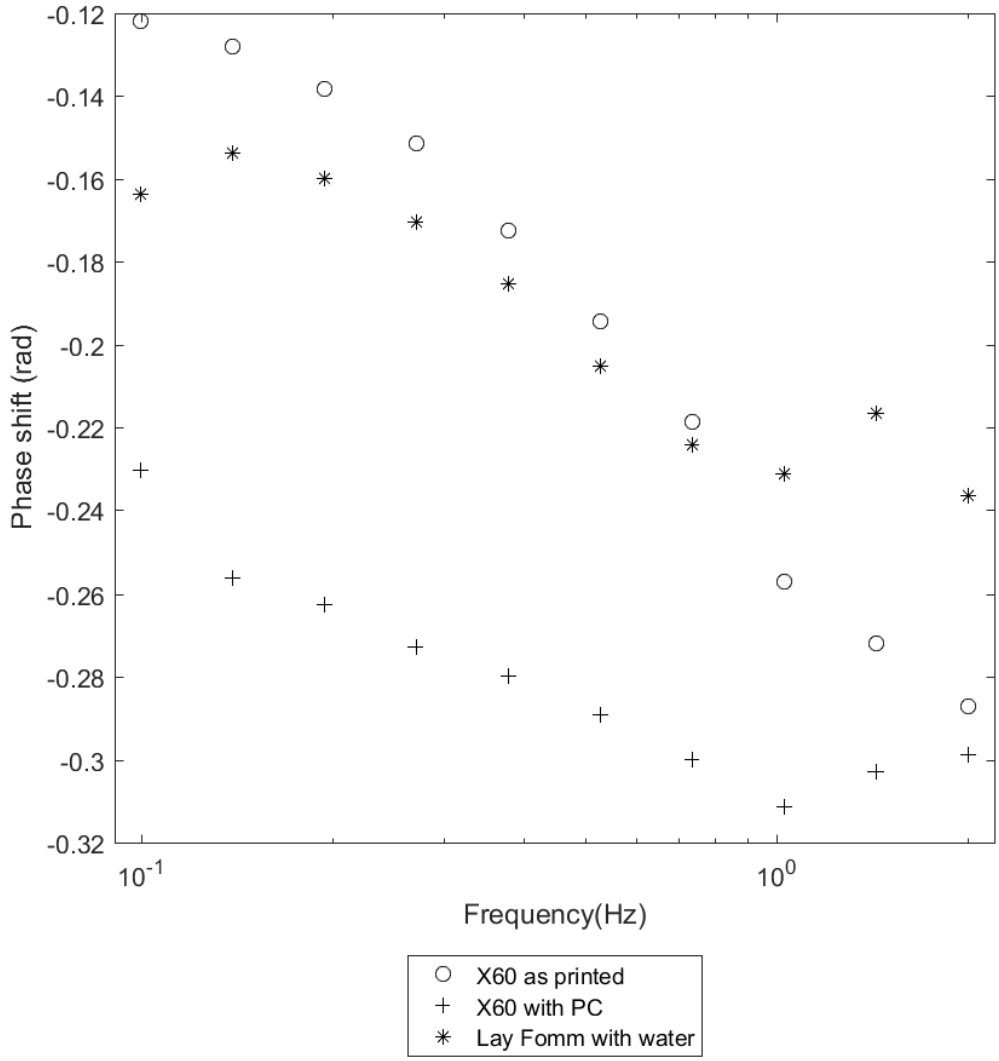

Figure 6.13: The phase shift of the position and the force in the compressive Young's modulus measurement in the $z-$direction

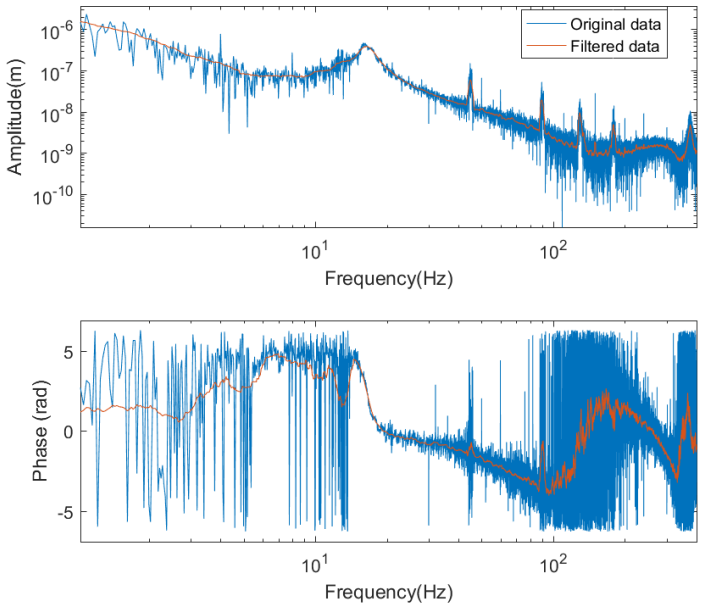

Figure 6.14: The response to a chirp input signal

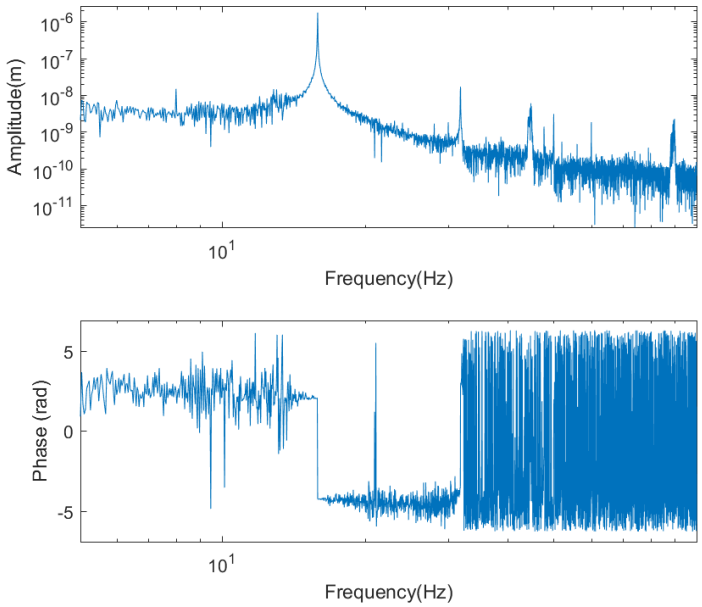

Figure 6.15: The response to a sinusoidal input signal at 15.9 Hz

cantilever at the oscillation frequency, after excitation with a signal with an amplitude of 50 V, is 1.76 µm.

6.5 Conclusion

The dielectric constant and young's modulus of several dielectrics have been determined. Also two conflicting estimates of the number of ions present in the dielectrics have been made, which will need further investigation. During the voltammetric experiment behaviour was observed that suggest that chemical reactions that reduce the number of ions in the dielectric occur at the electrodes. At last it was shown that the proof of concept actuator actually moves.

7 Conclusion and Discussion

To be able to additively manufacture complex robotic systems, first an actuator that can be printed has to be developed. This actuator should be electrical, have a price per gram that makes it economically viable to print parts that have weight in the order of kilograms and should be safe in the sense that no excessively high voltages are required.

Many different types of printable actuators have been studied with the conclusion that with the printers currently available at the research group RAM, printing an electrostatic actuator is the most viable.

The analysis of the dielectric of such an actuator lead to the requirements of a high dielectric constant, a high breakdown field and a thin minimum layer thickness. The conductor should have a resistance that is low enough to charge and discharge the dielectric at the required operating frequency. The total effective Young's modulus of the conductor and the dielectric should be as low as possible but for a linear dielectric the total effective Young's modulus should be above 64 kPa.

In this work it has been shown that plasticising a dielectric with a plasticizer with a high dielectric constant can improve the performance of printable elastic materials by increasing the materials dielectric constant and decreasing the materials Young's modulus. However long term degradation of the material and breakdown characteristics still have to be determined. Furthermore the used plasticizer turned out to be incompatible with the available flexible conductors.

The most promising dielectric is plasticised X60, which has a relative dielectric constant around 30 and a compressive Young's modulus of 1.8 MPa. It is expected to reach the required strain of 20 % when printed at a layer thickness of 6 µm and an actuation voltage of 300 V. This is in case of infinitely thin electrodes and has a corresponding expected work density of 30 kJ m^{-3}.

The required minimum layer thickness might be increased by further increasing the dielectric constant of the dielectric by adding conductive particles or particles with a high dielectric constant.

With the currently available technology, which consists of printing insulating layers of X60 at layer thicknesses of 100 µm, a 3D printed cantilever shaped actuator has been fabricated. This cantilever showed a deflection of 1.76 µm at it's resonance frequency of 16.4 Hz. Furthermore it was shown that the currently available technology can be used to fabricate capacitive sensors.

Bibliography

3DPrinterClassifieds.com (2017), 3d printer classifieds, http://www.3dprinterclassifieds.com/3d-printers-classifieds/wp-content/uploads/2015/10/328080-500x457.jpg.

Acoustics, K. E. (2017), dielectric constant chart, https://www.kabusa.com/Dilectric-Constants.pdf.

Atkins, P. and d. J. Paula (2006), *Physical Chemistry*, W. H. Freeman and Company, 8 edition, ISBN 0-7167-8759-8.

Balachandran, B. and E. B. Magrab (2009), *Vibrations*, Cengage Learning, 2 edition, ISBN 9780534552060.

Bartnikas, R. (1994), *Electrical Insulating Liquids (Engineering Dielectrics, Vol 3) (v. 3)*, Astm Intl, ISBN 0803120559.

Bondarenko, A. S. and G. A. Ragoisha (2008), Equivalent Circuit Elements and Parameters, http://www.abc.chemistry.bsu.by/vi/analyser/parameters.html.

Boukamp, B. (1995), A linear Kronig-Kramers transform test for immittance data validation, **vol. 142**, no.6, pp. 1885–1894, doi: 10.1149/1.2044210.

Brochu, P. and Q. Pei (2010), Advances in dielectric elastomers for actuators and artificial muscles, **vol. 31**, no.1, pp. 10–36, ISSN 10221336, doi: 10.1002/marc.200900425.

Carrico, J. D., N. W. Traeden, M. Aureli and K. K. Leang (2015), Fused filament 3D printing of ionic polymer-metal composites (IPMCs), **vol. 24**, no.12, p. 125021, ISSN 0964-1726, doi: 10.1088/0964-1726/24/12/125021.

Chaplin, M. (2017), water electrolysis, http://www1.lsbu.ac.uk/water/electrolysis.html.

Chin, T. E., U. Rhyner, Y. Koyama, S. R. Hall and Y.-m. Chiang (2006), Lithium Rechargeable Batteries as Electromechanical Actuators, *Electrochemical and Solid-State Letters*, pp. 134–138, doi: 10.1149/1.2161523.

Code Aster (2017), Anisotropic elasticity, https://www.code-aster.org/V2/doc/v12/en/man_r/r4/r4.01.02.pdf.

Coulter, F. B. (2011), Master thesis: The Fabrication of Artificial Facial Muscles, http://www.neonfleacircus.com/thesis_FINAL.pdf.

Damjanovic, D. (1998), Ferroelectric, dielectric and piezoelectric properties of ferroelectric thin films and ceramics, **vol. 61**, no.9, p. 1267, doi: 10.1088/0034-4885/61/9/002.

Diabase Engineering (2017), X60 Ultra-Flexible Filament âĂŞ White, https://flexionextruder.com/shop/x60-ultra-flexible-filament-white/.

Duduta, M., R. J. Wood and D. R. Clarke (2016), Multilayer Dielectric Elastomers for Fast, Programmable Actuation without Prestretch, **vol. 28**, no.36, pp. 8058–8063, ISSN 15214095, doi: 10.1002/adma.201601842.

Engineering, D. (2017), Flexion Extruder, https://flexionextruder.com.

Feynman, R., R. Leighton and M. Sands (1963a), *The Feynman Lectures on Physics*, number v. 2 in The Feynman Lectures on Physics, Addison-Wesley.
http://www.feynmanlectures.caltech.edu/II_14.html

Feynman, R., R. Leighton and M. Sands (1963b), *The Feynman Lectures on Physics*, number v. 2 in The Feynman Lectures on Physics, Addison-Wesley.
http://www.feynmanlectures.caltech.edu/II_19.html

Flashforge (2017), NEW CREATOR PRO 3D PRINTER(2016), http://www.flashforge.com/creator-pro-3d-printer/.

Gamry Instruments (2017), Basics of Electrochemical Impedance Spectroscopy, https://www.gamry.com/application-notes/EIS/basics-of-electrochemical-impedance-spectroscopy/.

Ghaffarzadeh, K. (2017), Where is the printed thin film transistor technology now?, http://www.printedelectronicsworld.com/articles/5115/where-is-the-printed-thin-film-transistor-technology-now.

Gramoll, K. (2017), Composite beams, http://www.ecourses.ou.edu/cgi-bin/ebook.cgi?topic=me&chap_sec=06.1&page=theory.

Graphene Labs (2017), Conductive TPU Pellets 500g, https://graphene-supermarket.com/Conductive-TPU-Pellets.html.

Griffiths, D. J. (1999a), *Introduction to Electrodynamics*, Prentice Hall, 3 edition, ISBN 0-13-805326-x, equation 7.6. http://www.physicspages.com/2013/04/18/force-between-current-loops-newtons-third-law/

Griffiths, D. J. (1999b), *Introduction to Electrodynamics*, Prentice Hall, 3 edition, ISBN 978-8120316010.

Griffiths, D. J. (2007), *Introduction to Electrodynamics*, Prentice Hall, 3 edition, ISBN 978-8120316010, problem 5.49. http://www.physicspages.com/2013/04/18/force-between-current-loops-newtons-third-law/

Gutmann, F. (1948), The Electret, *Rev. Mod. Phys.*, **vol. 20**, pp. 457–472, doi: 10.1103/RevModPhys.20.457. https://link.aps.org/doi/10.1103/RevModPhys.20.457

Horvai, G. (1991), Relationship between Charge Transfer Resistance and Exchange Current Density of Ion Transfer at the Interface of Two Immiscible Electrolyte Solutions, *Electroanalysis*, **vol. 3**, pp. 673–675, doi: 10.1002/elan.1140030713.

Hrabovcova, J. P. T. J. V. (2009), *Design of Rotating Electrical Machines*, John Wiley and Sons, ISBN 0-470-69516-1. https://books.google.nl/books?id=_y3LSh1XTJYC

Huan, T. D., S. Boggs, G. Teyssedre, C. Laurent, M. Cakmak, S. Kumar and R. Ramprasad (2016), Advanced polymeric dielectrics for high energy density applications, *Progress in Materials Science*, **vol. 83**, pp. 236–269, ISSN 00796425, doi: 10.1016/j.pmatsci.2016.05.001.

Huber, C., C. Abert, F. Bruckner, M. Groenefeld, O. Muthsam, S. Schuschnigg, K. Sirak, R. Thanhoffer, I. Teliban, C. Vogler, R. Windl and D. Suess (2016), 3D print of polymeer bonded rare-earth magnets, and 3D magnetic field scanning with an end-user 3D printer, **vol. 109**, no.16, ISSN 00036951, doi: 10.1063/1.4964856.

Interactive Learning Paradigms Incorporated (2016), HMISÂő - Hazardous Materials Identification System, http://www.ilpi.com/msds/ref/hmis.html.

Ion Power (2017), Nafion beads, http://www.nafionstore.com/store/products/194/Nafion-NR50-1100-EW-Polymer-Beads.

Karlsruhe Institute of Technology (2017), Kramers-Kronig Validity Test Lin-KK for Impedance Spectra, https://www.iam.kit.edu/wet/english/Lin-KK.php.

Kutner, M., C. Nachtsheim, N. J. and L. W. (2004), *Applied Linear Statistical Models*, McGraw-Hill/Irwin, 5 edition, ISBN 978-0073108742, equation 13.31 and 13.32. http://fac.ksu.edu.sa/sites/default/files/kut86916_ch13.pdf

La, T. G. and G. K. Lau (2013), Very high dielectric strength for dielectric elastomer actuators in liquid dielectric immersion, **vol. 102**, no.19, ISSN 00036951, doi: 10.1063/1.4806976.

Landau, L., L. P. Pitaevskii and E. Lifshitz (1984), *Electrodynamics of continuous media*, Pergamon Press, 2 edition, ISBN 978-0750626347, chapter 4.

LibreTexts (2017), Polar Protic and Aprotic Solvents, `https://chem.libretexts.org/Core/Organic_Chemistry/Fundamentals/Intermolecular_Forces/Polar_Protic_and_Aprotic_Solvents`.

Link, C. (2017), Permanent Magnets Explained by Magnetic Surface Currents, `https://www.physicsforums.com/insights/permanent-magnets-ferromagnetism-magnetic-surface-currents/`.

Liu, S., T. Kaplan and L. Gray (1986), AC response of fractal interfaces, **vol. 18**, no.Part 1, pp. 65 – 71, ISSN 0167-2738, doi: 10.1016/0167-2738(86)90090-1.

Ma, H., W. Wen, W. Y. Tam and P. Sheng (2003), Dielectric electrorheological fluids: Theory and experiment, **vol. 52**, no.4, pp. 343–383, doi: 10.1080/0001873021000059987.

Madden, J. D. W., N. A. Vandesteeg, P. A. Anquetil, P. G. A. Madden, A. Takshi, R. Z. Pytel, S. R. Lafontaine, P. A. Wieringa and I. W. Hunter (2004), Artificial muscle technology: physical principles and naval prospects, **vol. 29**, no.3, pp. 706–728, ISSN 0364-9059, doi: 10.1109/JOE.2004.833135.

Magnetfabrik Bonn (2017), Neofer 25/60p, `http://www.magnetfabrik.de/magnetfabrik_en/download_pdf.php?id=20`.

makeitfrom (2017), Polyvinylidene Fluoride (PVDF), `http://www.makeitfrom.com/material-properties/Polyvinylidene-Fluoride-PVDF`.

Matsuda, Y. (1981), Behavior of Some Ions in Mixed Organic Electrolytes of High Energy Density Batteries, **vol. 128**, no.12, p. 2552, doi: 10.1149/1.2127289.

Matter Hackers (2017a), PORO-LAY GEL-LAY Porous Filament, `https://www.matterhackers.com/store/3d-printer-filament/poro-lay-gel-lay-porous-filament-175mm`.

Matter Hackers (2017b), PORO-LAY LAY-FOMM 40 Porous Filament, `https://www.matterhackers.com/store/3d-printer-filament/poro-lay-lay-fomm-filament-175mm`.

Mellinger, A., M. Wegener, W. Wirges, R. R. Mallepally and R. Gerhard-Multhaupt (2006), Thermal and Temporal Stability of Ferroelectret Films Made from Cellular Polypropylene/Air Composites, **vol. 331**, no.1, pp. 189–199, doi: 10.1080/00150190600737933.

Minteer, T. M. (2014), Electrostatic stress: insightful analysis and manipulation of Maxwell's stress equation for electrostatics, **vol. 21**, no.1, pp. 64–73, ISSN 1070-9878, doi: 10.1109/TDEI.2013.003840.

Mirfakhrai, T., J. D. Madden and R. H. Baughman (2007), Polymer artificial muscles, **vol. 10**, no.4, pp. 30 – 38, ISSN 1369-7021, doi: 10.1016/S1369-7021(07)70048-2.

Miriyev, A., K. Stack and H. Lipson (2017), Soft material for soft actuators, *Nature Communications*, pp. 1–8, ISSN 2041-1723, doi: 10.1038/s41467-017-00685-3.

Multi3D LLC. (2017), Electrifi FAQ, `https://www.multi3dllc.com/faqs/`.

Nave, R. (2017), Saturated Vapor Pressure, `http://hyperphysics.phy-astr.gsu.edu/hbase/Kinetic/vappre.html`.

Ninjatek (2017), Ninjaflex 3D printing filament, `https://ninjatek.com/wp-content/uploads/2016/05/NinjaFlex-TDS.pdf`.

Palmiga Innovations (2017), Rubber 3d printing, `http://rubber3dprinting.com`.

Pelrine, R., R. Kornbluh, J. Joseph, R. Heydt, Q. Pei and S. Chiba (2000), High-field deformation of elastomeric dielectrics for actuators, **vol. 11**, no.2, pp. 89 – 100, ISSN 0928-4931, doi: 10.1016/S0928-4931(00)00128-4.

Rajala, S. and J. Lekkala (2010), PVDF and EMFi sensor materials - A comparative study, *Procedia Engineering*, **vol. 5**, pp. 862–865, ISSN 18777058, doi: 10.1016/j.proeng.2010.09.245.

Refle, O. (2017), NextFactory - the Solution, `http://www.nextfactory-project.eu/page/about-nextfactory/solution.php`.

Risner, J. (2008), *Investigation of Dielectric Elastomer Actuation for Printable Mechatronics*, University of California, Berkeley with the University of California, San Francisco. `http://oskicat.berkeley.edu/record=b21326756~S1`

Russel, W., D. Saville and W. Schowalter (1989), *Colloidal Dispersions*, Cambridge Monographs on Mechanics, Cambridge University Press, ISBN 9780521426008. `https://books.google.nl/books?id=3shp8Kl6YoUC`

Sborikas, M., X. Qiu, W. Wirges, R. Gerhard, W. Jenninger and D. Lovera (2014), Screen printing for producing ferroelectret systems with polymer-electret films and well-defined cavities, **vol. 114**, no.2, pp. 515–520, ISSN 09478396, doi: 10.1007/s00339-013-7998-3.

Schonleber, M., D. Klotz and E. Ivers-TiffÃl'e (2014), A Method for Improving the Robustness of linear Kramers-Kronig Validity Tests, **vol. 131**, no.Complete, pp. 20–27, doi: 10.1016/j.electacta.2014.01.034.

Schouten, M. (2017), *Optimisation of a printable piezoelectric sensor fabrication process*, unpublished.

Sciencelab (2017), Material Safety Data Sheet Listing, `https://www.sciencelab.com/msdsList.php`.

Sihvola, A. (2000), Mixing Rules with Complex Dielectric Coefficients, **vol. 1**, no.4, pp. 393–415, ISSN 1573-9317, doi: 10.1023/A:1026511515005.

Solvay (2017), Solvene 250 EAP inks, `http://www.solvay.com/en/binaries/Solvene-250-EAP-Inks_EN-231084.pdf`.

Sounart, T. L., T. A. Michalske and K. R. Zavadil (2005), Frequency-dependent electrostatic actuation in microfluidic MEMS, **vol. 14**, no.1, pp. 125–133, ISSN 1057-7157, doi: 10.1109/JMEMS.2004.839006.

Stoyanov, H., P. Brochu, X. Niu, C. Lai, S. Yun and Q. Pei (2013), Long lifetime, fault-tolerant freestanding actuators based on a silicone dielectric elastomer and self-clearing carbon nanotube compliant electrodes, *RSC Adv.*, **vol. 3**, pp. 2272–2278, doi: 10.1039/C2RA22380E.

Stratasys (2017), Objet260 Connex3, `http://www.stratasys.com/3d-printers/objet260-connex3`.

Svetovoy, V. B., R. G. P. Sanders and M. C. Elwenspoek (2013), Transient Nanobubbles in Short-Time Electrolysis., **vol. 25**, no.18, p. 184002, ISSN 1361-648X, doi: 10.1088/0953-8984/25/18/184002.

Svetovoy, V. B., R. G. P. Sanders, T. S. J. Lammerink and M. C. Elwenspoek (2011), Combustion of hydrogen-oxygen mixture in electrochemically generated nanobubbles, **vol. 84**, no.3, pp. 3–6, doi: 10.1103/PhysRevE.84.035302.

Svetovoy, V. B., R. G. P. Sanders, K. Ma and M. C. Elwenspoek (2014), New type of microengine using internal combustion of hydrogen and oxygen., *Scientific reports*, **vol. 4**, p. 4296, doi: 10.1038/srep04296.

Svetovoy, V. B., I. V. Uvarov, A. V. Postnikov, R. G. P. Sanders and G. Krijnen (2016), Electrochemical actuator with a short response time: A new actuation regime, *Sensors and Actuators, A: Physical*, **vol. 243**, pp. 1–6, doi: 10.1016/j.sna.2016.03.002.

The Quadrant group (2017), PVDF technical data sheet, https://www.theplasticshop.co.uk/plastic_technical_data_sheets/pvdf_technical_data_sheet.pdf.

Thomson, G. W. (1946), The Antoine Equation for Vapor-pressure Data., **vol. 38**, no.1, pp. 1–39, doi: 10.1021/cr60119a001, pMID: 21016992.

ToolBox, T. E. (2017), Coefficients of Linear Thermal Expansion, http://www.engineeringtoolbox.com/linear-expansion-coefficients-d_95.html.

Torop, J., V. Palmre, M. Arulepp, T. Sugino, K. Asaka and A. Aabloo (2011), Flexible supercapacitor-like actuator with carbide-derived carbon electrodes, **vol. 49**, no.9, pp. 3113 – 3119, ISSN 0008-6223, doi: 10.1016/j.carbon.2011.03.034.

Voxel8 (2017a), Breaking barriers in multi-material 3d printing, http://www.voxel8.com/printer/.

Voxel8 (2017b), Technical datasheet, https://p4.zdassets.com/hc/theme_assets/638849/200059206/Silver_Ink_Standard_TDS.pdf.

Weisstein, E. W. (2017a), Cross-Correlation Theorem, http://mathworld.wolfram.com/Cross-CorrelationTheorem.html.

Weisstein, E. W. (2017b), Laplace Transform, http://mathworld.wolfram.com/LaplaceTransform.html.

Welleweerd, M. (2017), *3D printing a three degree of freedom force sensor*, unpublished.

Whitney, S. (1999), Vibrations of Cantilever Beams: Deflection, Frequency, and Research Uses, http://emweb.unl.edu/Mechanics-Pages/Scott-Whitney/325hweb/Beams.htm.

Yousefi, N., X. Sun, X. Lin, X. Shen, J. Jia, B. Zhang, B. Tang, M. Chan and J. K. Kim (2014), Highly aligned graphene/polymer nanocomposites with excellent dielectric properties for high-performance electromagnetic interference shielding, **vol. 26**, no.31, pp. 5480–5487, ISSN 15214095, doi: 10.1002/adma.201305293.

Yuan, J., A. Luna, W. Neri, C. Zakri, T. Schilling, A. Colin and P. Poulin (2015), Graphene liquid crystal retarded percolation for new high-k materials, **vol. 6**, no.May, p. 8700, ISSN 2041-1723, doi: 10.1038/ncomms9700.

Zhang, Z., L. Liu, J. Fan, K. Yu, Y. Liu, L. Shi and J. Leng (2008), New silicone dielectric elastomers with high dielectric constant, **vol. 6926**, no.2008, pp. 692610–692610–8, ISSN 0277786X, doi: 10.1117/12.775989.

A Performance estimate of printed piezoelectric actuators

In this appendix the performance of an sheet actuator made from high performance piezoelectric PVDF-TrFE ink will be estimated.

A.1 Sheet actuator

The most simple actuator that can be printed is an actuator that consists of layers of PVDF-TrFE with a thin conductor in between, see figure A.1. Note that due to the high efficiency of the actuator and the high voltage used, the electrodes can have a relatively high resistance without limiting the power density of the material.

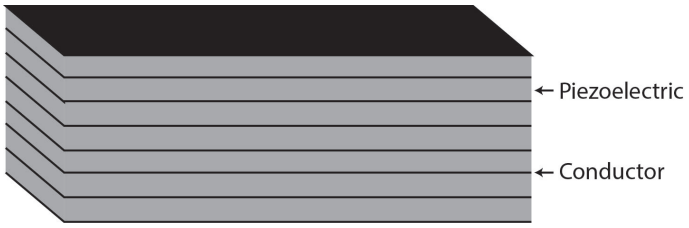

Figure A.1: A sheet actuator

The strain of a sheet actuator depends on the piezoelectric constant in the 33 direction (d_{33}) and the maximum electric field that can be applied. When actuated at the maximum peak voltage and when assuming that the actuator is unconstrained in the 1 and 2 direction, the total strain is (Damjanovic, 1998)

$$\epsilon = \frac{d_{33} V}{t} \tag{A.1}$$

Where V is the applied voltage and t is the thickness of the sheets. When the strain of the material is combined with the Young's modulus of the material the work density of the actuator can be calculated using Equation 2.1

$$\begin{aligned} W_\mathrm{d} &= \frac{1}{2} Y \epsilon^2 \\ &= \frac{1}{2} Y \frac{d_{33}^2 V^2}{t^2} \end{aligned} \tag{A.2}$$

Where Y is the Young's modulus of the material and W_d is the work density. However a piezoelectric actuator can be made to contract and to expand. The actuator will contract or expand depending on the sign of the applied voltage. Therefore the the actual strain and work density that can be achieved without exceeding the voltage limit of 300 V, is twice as high

$$\begin{aligned} \epsilon &= 2\frac{d_{33} V}{t} \\ W_\mathrm{d} &= Y \frac{d_{33}^2 V^2}{t^2} \end{aligned} \tag{A.3}$$

A.2 Sheet actuator with Solvene EAP ink

PVDF is commercially available from Solvay as an ink with TrFE as a co-polymer, see figure A.2. The TrFE co-polymer makes that more of the material will be in the piezoelectric β phase.

In August 2015 a bottle containing 100 g of the casting solution containing 25 % solid content, could be purchased for 675 euro. This results in a price of 27 euro per gram.

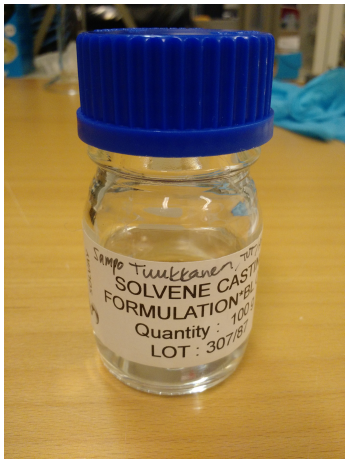

Figure A.2: Solvene casting formulation

The Young's modulus of the material is not known, therefore a rough estimate of 3 GPa based on the Young's modulus of PVDF (Rajala and Lekkala, 2010) will be used.

The piezoelectric constant of the PVDF-TrFE that is supplied by the manufacturer is -22 pC per meter and the breakdown voltage is 250 $\mathrm{MV\,m^{-1}}$ Solvay (2017). This would suggest that an actuation voltage of 100 $\mathrm{MV\,m^{-1}}$ might be possible which results in a strain of 0.0044 and a work density of 13.2 $\mathrm{MJ\,m^{-3}}$. Printing a sheet actuator that uses a "safe" voltage of 300 V however would require a layer thickness of at least 3 µm and probably even less due to the high layer requirements.

Results for blade coating the ink outside a cleanroom indicate that at a thickness of approximately 6 µm a polarisation voltage of 35 $\mathrm{MV\,m^{-1}}$ and 5 $\mathrm{pC\,N^{-1}}$ can be achieved (Schouten, 2017). This indicates that an actuation voltage of 20 $\mathrm{MV\,m^{-1}}$ might be used. This would result in a strain of $2 \cdot 10^{-4}$ and a work density of 600 $\mathrm{kJ\,m^{-1}}$. These result suggest that making an actuator that can be used below 300 volt would require a printer that has a minimum layer thickness of at less than 15 µm

The post processing required is annealing and polarising of the material. The required uniformity and purity of the layers is high, since the material has to be polarised close to the breakdown voltage to obtain a high piezoelectric constant. It is therefore expected that one film will have to be printed out of several smaller layers in order to reach the required layer quality and uniformity.

Table A.1: Estimate of the performance of PVDF-TrFE

Maximum strain	$4.4 \cdot 10^{-3}$	$2 \cdot 10^{-4}$
Work density	13 $\mathrm{MJ\,m^{-3}}$	600 $\mathrm{kJ\,m^{-3}}$
Operating frequency	0 Hz - >1 Hz	0 Hz- >1 Hz
Required layer thickness	1-3 µm	5-15 µm
Cost	27 €/g	27 €/g

B Performance estimate of printed magnetic actuators

Almost all electrical actuators larger then a few millimetre that are in use today, are magnetic actuators. It therefore makes sense to investigate the possibility of printing this type of actuator. To evaluate the feasibility of this type of actuator, the performance of a voice coil actuator in combination with some 3D printable materials will be estimated.

B.1 Materials

Traditional magnetic actuators use both material with a large remanent magnetisation (1 - 1.3 T (Hrabovcova, 2009)) as well as materials which can handle a large current density due to their low resistivity ($1.68 \cdot 10^{-8} \Omega$m for copper). This section will list some of the most conductive and 3D printable material that are available today. Also one material with a high remanent magnetisation will be discussed.

B.1.1 Neofer 25/60p

Neofer 25/60p is a compound of NdFeB grains with uniaxial magnetocrystalline anisotropy inside a PA11 matrix from the Magnetfabrik Bonn GmbH (Magnetfabrik Bonn, 2017), see Figure B.1. It can be printed using a fused deposition printer and has a remanent magnetisation of 310 mT (Huber et al., 2016). The costs of the Neofer 25/60p filament are unknown since the material is not sold as raw material.

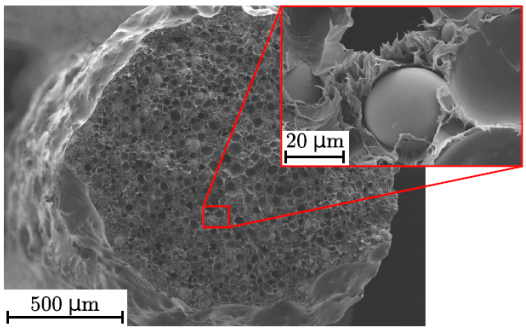

Figure B.1: A SEM image of neofer 25/60p. Image courtesy of (Huber et al., 2016)

Electrify filament

Electrify filament is a conductive metal-polymer composite form Multi3D LLC(Multi3D LLC., 2017). It is available in the form of standard 3D printer filament (Figure B.2) and it has a resistivity of 61 µΩm(Multi3D LLC., 2017). The price of 100g of 1.75mm filament was 94 euro in March 2017, which results in a price 1 euro per gram.

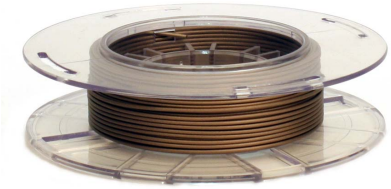

Figure B.2: A spool of electrifi filament. Image courtesy of (Multi3D LLC., 2017)

B.1.2 Silver ink

By combining a fused deposition extruder with a syringe extruder (Figure B.3), it is possible to print objects which contain wires made out of silver ink. A commercially available printer that does this is the Voxel8 (Voxel8, 2017a). The bulk resistivity of the ink is 0.3 µΩ m(Voxel8, 2017b). The silver ink costs 75 euro per barrel of 3 mL. The price per millilitre therefore is 25 euro.

Figure B.3: A barrel of voxel8 ink. Image courtesy of (Voxel8, 2017b)

B.2 Voice coil actuator

A typical magnetic actuator is a voice coil actuator, which consists of a cylindrical solenoid and a magnet, see figure B.4. The force generated by this actuator can be calculated by combining the Biot-Savart law, Lorentz force law and the notion that a piece of magnetised material can be thought of as a structure with a certain current density along the surface(Griffiths, 2007). The surface current per unit length along the edge of the magnetised piece of material can be calculated using the Equation (Link, 2017):

$$\boldsymbol{K}_{\mathrm{m}} = \frac{1}{\mu_0} \boldsymbol{M} \times \hat{\boldsymbol{n}} \tag{B.1}$$

where $\boldsymbol{K}_{\mathbf{m}}$ is a vector representing the surface current per unit length, $\boldsymbol{M}$ is a vector representing the magnetisation of the magnet, μ_0 is vacuum permittivity and $\hat{\boldsymbol{n}}$ is a unit vector normal to the magnets surface.

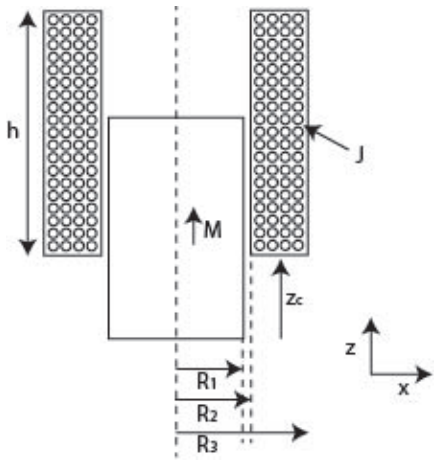

Figure B.4: A voice coil actuator

For a cylindrical magnet magnetised in the $z-$direction, as in Figure B.4, the cross product of the magnetisation and vector normal to the surface is zero on the flat surface. On the round surface the normal vector of the surface is always orthonormal to the magnetisation vector and the resulting cross product points in the $\phi-$direction. The magnet therefore can be perfectly described by a coil with one layer of very thin wires. Furthermore the current on the round surface can easily be calculated:

$$\begin{aligned} \boldsymbol{K}_{\mathrm{m}} &= \frac{1}{\mu_0}\begin{bmatrix} 0 \\ 0 \\ M \end{bmatrix} \times \begin{bmatrix} \cos(x) \\ \sin(x) \\ 0 \end{bmatrix} \\ &= \frac{M}{\mu_0}\begin{bmatrix} -\sin(x) \\ \cos(x) \\ 0 \end{bmatrix} \end{aligned} \tag{B.2}$$

For this known current density distribution the law of Biot-Savart gives a description of the generated magnetic field (Feynman et al., 1963a).

$$\boldsymbol{B} = \frac{\mu_0}{4\pi}\int \frac{\boldsymbol{J} \times \boldsymbol{r}_{12}}{|\boldsymbol{r}_{12}|^3} dV \tag{B.3}$$

Where **B** is the magnetic field, $\boldsymbol{J}$ the current density distribution at certain point and $\boldsymbol{r}_{12}$ is the distance vector in between this point and the point in which the magnetic field is calculated. For a cylindrical magnet magnetised in the $z-$direction, as in Figure B.4, there only exists a current on the round surface of the cylindrical magnet.

$$\boldsymbol{B} = \frac{\mu_0}{4\pi}\int \frac{\boldsymbol{K}_{\mathbf{m}} \times \boldsymbol{r}_{12}}{|\boldsymbol{r}_{12}|^3} dS \tag{B.4}$$

For a magnet with the dimension as in Table B.1 the magnetic field that follows from this equation is calculated using the matlab script called "voicecoil.m". The result is plotted in Figure B.5 and B.6.

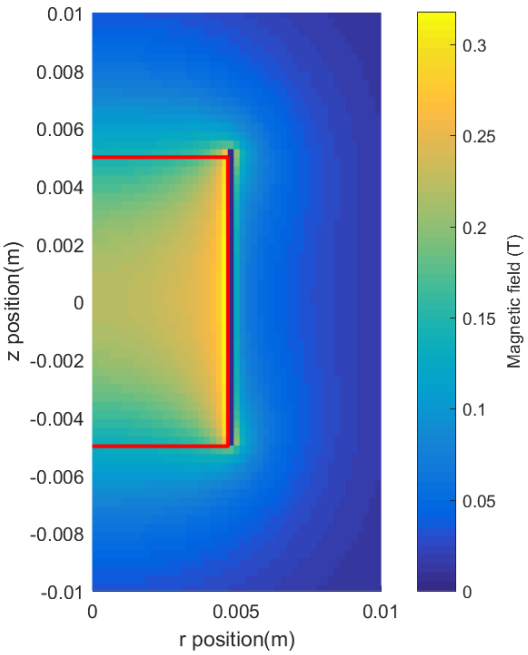

Figure B.5: The magnetic field of a cylindrical magnet. The red lines indicate the location of the magnet.

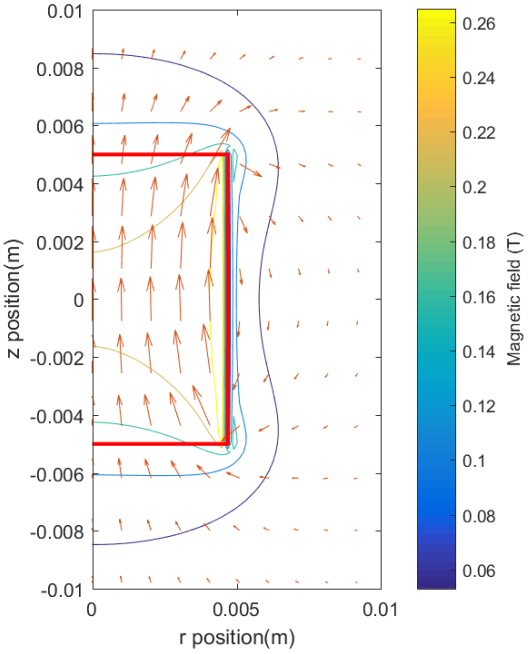

Figure B.6: The magnetic field of a cylindrical magnet. The red lines indicate the location of the magnet.

As a reference the magnetic field by a magnet with the same dimensions is also calculated using a 2D axisymmetric magneto-static simulation in Comsol multiphysics, by using a magnetisation relation. The simulation used a circular boundary with a radius of 200mm. The file containing this simulation is named "magneticField.mph". The resulting magnetic field is plotted in figure B.7.

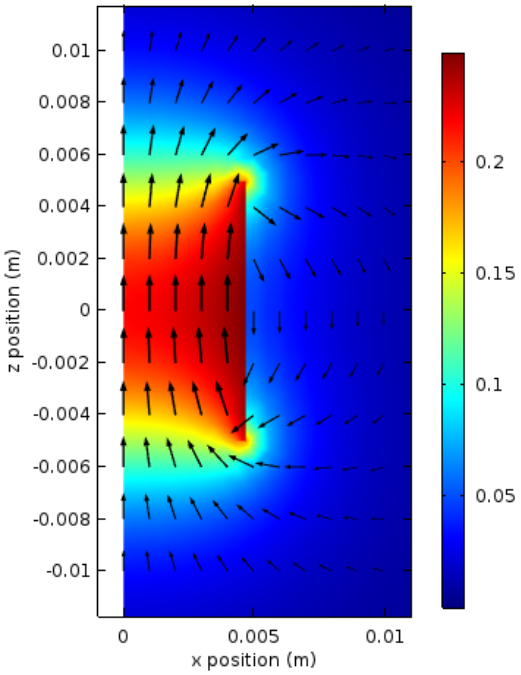

Figure B.7: The magnetic field of a cylindrical magnet, calculated using Comsol

Table B.1: Dimensions of the simulated voice coil

h	Magnet and coil height	10 mm
M	Magnetisation	0.3 T
R_1	Magnet outer diameter	4.7 mm
R_2	Coil inner diameter	5 mm
R_3	Coil outer diameter	7 mm

Next the force on the coil generated by the magnetic field will be calculated using the Lorentz force law, using the assumption that the electrostatic forces are negligible.(Griffiths, 1999b)

$$\begin{aligned} \boldsymbol{f} &= \rho \boldsymbol{E} + \boldsymbol{J} \times \boldsymbol{B} \\ &= \boldsymbol{J} \times \boldsymbol{B} \end{aligned} \tag{B.5}$$

Where $\boldsymbol{f}$ is the force density generated by the current density $\boldsymbol{J}$ and the magnetic field $\boldsymbol{B}$. To calculate the total force exerted on the coil the previous equation is integrated over the volume of the coil.

$$\boldsymbol{F} = \int \boldsymbol{J} \times \boldsymbol{B} dV \tag{B.6}$$

B.3 Neofer 25/60p and Electrify voice coil actuator

In case Electrify filament is used as a conductor, the maximum current density that can be reached depends on the ratio in between the surface and the volume of the coil (Multi3D LLC., 2017). This is since this ratio will determine the cooling rate of the material. In this case the ratio is:

$$\begin{aligned}\frac{S}{V} &= \frac{2(\pi R_3^2 - \pi R_2^2) + 2\pi R_2 h + 2\pi R_3 h}{\pi R_3^2 h - \pi R_2^2 h} \\ &= 1.2\,\mathrm{mm}^{-1}\end{aligned} \tag{B.7}$$

In this case the maximum current density is (Multi3D LLC., 2017):

$$\begin{aligned}J_{\max} &= 55 * \frac{S}{V} + 34 \\ &= 66\,\mathrm{kA\,m}^{-2}\end{aligned} \tag{B.8}$$

The total force that the actuator exerts, using a current density of $50\,\mathrm{kA\,m}^{-2}$ and Equation B.6, is calculated both in Matlab and in Comsol. The resulting force is calculated as a function of the position of the coil relative to the magnet z_c, see Figure B.4. The result can be found in figure B.8.

In the Comsol simulation the standard force calculation option is used, which integrates the maxwell stress tensor.

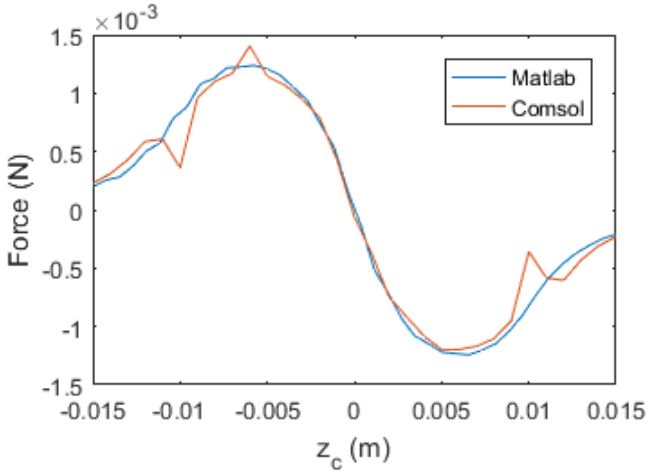

Figure B.8: The force exerted on the coil, calculated using Matlab and Comsol

Integration of the force calculated by Matlab from $-5\,\mathrm{mm}$ to $5\,\mathrm{mm}$, combined with the total volume required for the moving coil indicates a work density of:

$$\begin{aligned}W_d &= \frac{\int_{-5\cdot10^{-3}}^{5\cdot10^{-3}} F\,dz}{\pi R_3^2 2h} \\ &= 8.3\,\mathrm{J\,m}^{-3}\end{aligned} \tag{B.9}$$

Table B.2: Expected properties of a voice coil actuator made from Neofer 25/60p and Electrify

Maximum strain	0.5
Work density	$8.3\,\mathrm{J\,m}^{-3}$
Operating Frequency	0 Hz - >1 Hz
Required layer thickness	>100 µm
Cost	1€/g

B.4 Neofer 25/60p and silver ink voice coil actuator

For the Silver ink of the Voxel8 no current densities are given. However a rough estimate of the maximum current density that can be achieved, can be made by making the assumption that the thermal properties of the silver ink will be similar to the properties of the Electrify filament. This would imply the assumption that both electrify and silver ink can handle the same amount of joule heating and that since the conductivity of the silver ink is 200 times higher, the maximum current density of silver filament can be 200 times higher.

It should be taken into account that the resistivity of silver ink is so low that it is likely that multiple windings are necessary in order to get a practical current, so the current density likely will not be 100-200 times higher than the electrify's current density.

Because of the linear dependence of the actuation force on the current density this would increase the energy density of the actuator to 0.8 $kJ\,m^{-3}$ to 1.6 $kJ\,m^{-3}$.

Table B.3: Expected properties of a voice coil actuator made from Neofer 25/60p and silver ink

Maximum strain	0.5
Work density	0.8-1.6 $kJ\,m^{-3}$
Operating Frequency	0 Hz - >1 Hz
Required layer thickness	>20 µm
Cost	2.5-25 €/g

C Performance estimate of Dielectric Elastomer Actuators

In this appendix an estimate of the perforance of a printed dielectric elaster actuator at low actuation voltages will be made.

C.1 Sheet actuator

A simple type of DEA is an actuator which consists of alternating layers of non conducting elastomer and a thin layer of conductive elastic material, see Figure C.1. Note that due to the high efficiency of the actuator and the high voltage used for the actuation, the power density of the actuator can be relatively high even if the the conductivity of the conductive elastomer is low.

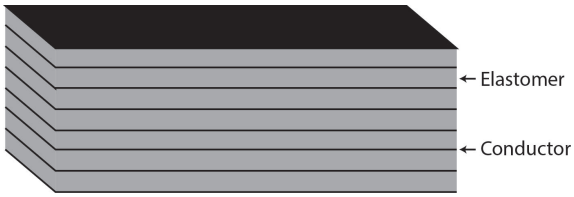

Figure C.1: A sheet actuator

In case the material and the electrodes consist of sheets, a parallel plate approximation can be used to calculate the behaviour of the actuator for small strains. In a parallel plate approximation the electric field is orthogonal to the plates everywhere and the Maxwell stress on the electrodes can be calculated using (Minteer, 2014)

$$\sigma = \frac{1}{2}\epsilon_r \epsilon_0 E^2. \tag{C.1}$$

Where ϵ_r is the dielectric constant of the material, ϵ_0 is vacuum permittivity and E is the magnitude of the electric field. Next the strain of the elastomer can be estimated if a linear elastic dielectric is assumed using the Young's modulus of the material

$$\begin{aligned} s &= \frac{\sigma}{Y} \\ &= \frac{1}{2}\frac{\epsilon_r \epsilon_0 E^2}{Y} \end{aligned} \tag{C.2}$$

Where s is the strain of the elastomer and Y is the Young's modulus of the material. Using Equation 2.2 the total power density of the actuator can be estimated

$$\begin{aligned} W_d &= \frac{1}{2}\sigma s \\ &= \frac{1}{8}\frac{\epsilon_r^2 \epsilon_0^2 E^4}{Y} \end{aligned} \tag{C.3}$$

C.2 Sheet actuator with Urethane Acrylate Oligomer

Dudata et al. fabricated a multilayer DEA based on Urethane Acrylate Oligomer (CN9018) which was spin coated in layers of 40 µm (Duduta et al., 2016). This material is capable of handling relatively high voltages of 100 $MV m^{-1}$ without prestretching. They measured the Young's modulus of the material to be in the order of 100 kPa. The cost of the material is unknown.

The dielectric constant of the material is not specified, an estimate based on the dielectric constant of acrylic resin and polyurethane resin results in a dielectric constant in between 3 and 7 (Acoustics, 2017). Therefore the electric field that is required to obtain a strain of 20 % is (see Equation C.2)

$$\begin{aligned} E &= \frac{sY}{\epsilon_0 \epsilon_r} \\ &= 25 - 39 \text{ MV m}^{-1} \end{aligned} \tag{C.4}$$

At the maximum high power voltage that is considered safe, which is 300 V, this would result in a required minimum layer thickness of 8-12 µm. However the required layer quality and uniformity is high, therefore it might be necessary to build up every layer out of several thinner layers.

Table C.1: Estimate of the performance of CN9018

Maximum strain	0.2
Work density	2kJ m^{-3}
Operating Frequency	0 Hz - >1 Hz
Required layer thickness	<4 µm-12 µm
Cost	Unknown

D Mechanism behind the (ferro)electret

In this appendix the mechanisms behind a traditional electret and ferroelectret transducer will be discussed.

D.1 The traditional electret

The traditional electret consists of a liquid material that solidifies under the influence of an electric field (Gutmann, 1948). When there are charged particles or dipoles present, they will distribute such that they generate a field that cancels out the applied electric field. When the material solidifies and the charges cannot move any more, this field will remain inside the material.

A build in electric field that is much larger as the applied electric field will result in a material that has a piezoelectric constant. To understand this, we will analyse a sheet of electret with electrodes coated on both sides. When a connection in between both electrodes is made a charge distribution will arise on both electrodes that will cancel out the fixed electric field inside the electret. When the electric field is orthogonal to the electrodes, the Maxwell stress generated by this charge is (Minteer, 2014):

$$\sigma = \frac{1}{2}\epsilon_0 \epsilon_r E_{\text{pol}}^2 \tag{D.1}$$

where E_{pol} is the polarisation electric field. When an actuation voltage is applied to the electret, this electric field will add to the already applied electric field

$$\begin{aligned} \sigma &= \frac{1}{2}\epsilon_0 \epsilon_r (E_{\text{pol}} + E_{\text{act}})^2 \\ &= \frac{1}{2}\epsilon_0 \epsilon_r (E_{\text{pol}}^2 + 2E_{\text{pol}}E_{\text{act}} + E_{\text{act}}^2) \end{aligned} \tag{D.2}$$

where E_{act} is the electric field applied in order to actuate the actuator. When the actuation electric field is small relative to the polarisation voltage($E_{\text{act}} << E_{\text{pol}}$), the strain after polarisation of the material is

$$\sigma = \epsilon_0 \epsilon_r E_{\text{pol}} E_{\text{act}} \tag{D.3}$$

Combined with Hookes law this results in the following expression for the strain as a function of the actuation electric field

$$s = \frac{\epsilon_0 \epsilon_r E_{\text{pol}} E_{\text{act}}}{Y} \tag{D.4}$$

Where Y is the Young's modulus of the material. When the previous equation is compared with Equation A.1 it can be concluded that

$$d_{33} = \frac{\epsilon_0 \epsilon_r E_{\text{pol}}}{Y} \tag{D.5}$$

D.2 The ferroelectret

A ferroelectret is a material that usually consists of a polymer with air voids (Mellinger et al., 2006). After polarisation there remains an electric field inside the material. This electric field makes the material piezoelectric as described in section D.1.

Mechanism

The mechanism which is expected to be responsible for the ferroelectric behaviour of the ferroelectret is a dielectric barrier discharge (Sborikas et al., 2014). When the ferroelectret is polarised below the dielectric strength of the air, which is the weakest material in terms of dielectric strength, there is no charge inside the material (figure D.1 a). However when electric field inside the air exceeds the breakdown field of air, the air is decomposed and charge accumulates on inside the material (Sborikas et al., 2014) (figure D.1 b).

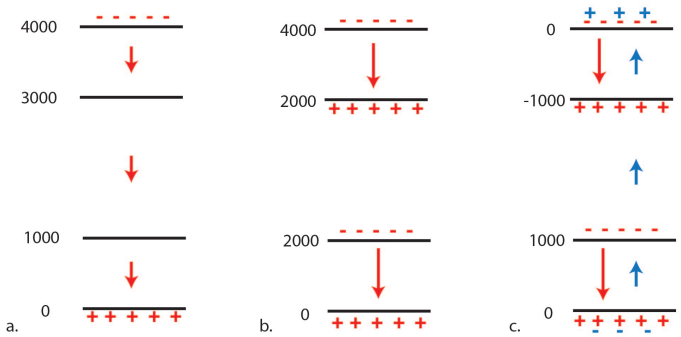

Figure D.1: Distribution of charge, electric field and voltage in the ferroelectret (a) during polarisation, before breakdown (b) during polarisation, after breakdown (c) when short circuited after polarisation

This charge stays at this interface semi permanently and makes that there are electric fields inside the material even when the voltage over the material is zero volt (figure D.1 c). The piezoelectricity of the material can be explained by the fact that the charge that is needed to compensate this field is dependent on the thickness of the material and therefore via the stiffness of the material on the force working on the material. See figure D.2 b and c for a schematic representation.

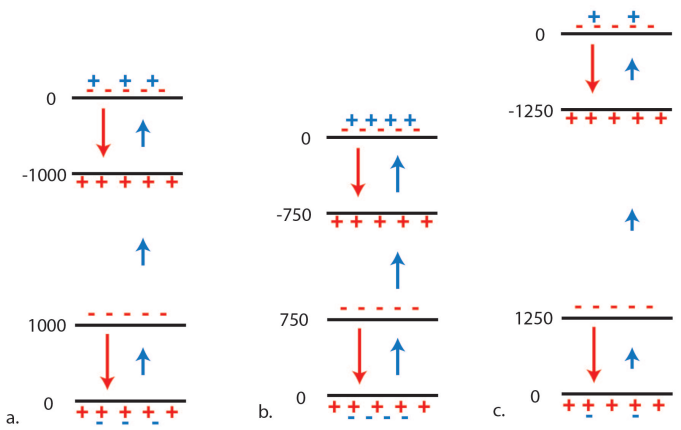

Figure D.2: Charge distribution and field (a) at rest (b) when compressed (c) when extended

E Efficiency of an electrolysis actuator

In this appendix the maximum efficiency of an actuator that uses a DC signal to split water into hydrogen and oxygen is calculated. The total reaction for the electrolysis of water is

$$2\,H_2O \longrightarrow 2\,H_2 + O_2$$

The minimum potential required for the electrolysis of water, at 25 °C and 1 bar, is about 1.2 V. The reaction requires 4 electrons (Chaplin, 2017) and produces 3 gas molecules. The amount of charge required therefore is

$$q = \frac{4}{3} n N_A e \tag{E.1}$$

where N_A is the constant of Avogadro, e is the charge of an electron and n is the number of moles of gas being produced. The amount of energy required therefore is

$$\begin{aligned} W_{\text{in}} &= qU \\ &= \frac{4}{3} n N_A e U \end{aligned} \tag{E.2}$$

where W_{in} is the required energy and U is the electrode potential of the reaction. Now suppose that the actuator is used to exert a constant pressure p on a piston, until a certain volume of gas V is produced, see figure E.1. In case the pressure is much higher than the atmospheric pressure, the amount of work that is produced by the actuator is

$$\begin{aligned} W_{\text{out}} &= \int_0^V P dV \\ &= PV \end{aligned} \tag{E.3}$$

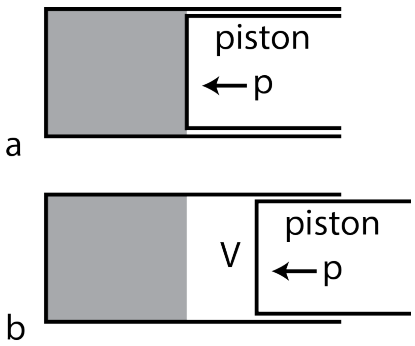

Figure E.1: A piston

In this situation the amount of work that can be produced per mole of gas follows from the ideal gas law

$$\begin{aligned} W_{\text{out}} &= PV \\ &= nRT \end{aligned} \tag{E.4}$$

Where R is the common gas constant and T is the absolute temperature. In this case the efficiency of the actuator at 298 K would be

$$\begin{aligned} \eta &= \frac{W_{\text{out}}}{W_{\text{in}}} \\ &= \frac{4}{3}\frac{RT}{N_A eU} \\ &= 2.9 \cdot 10^{-2} \end{aligned} \tag{E.5}$$

F Combined electrode-dielectric stiffness

Since the dielectric that will be used has a Poisson ratio close to 0.5, the electrodes will have to expand when the actuator contracts. This will have an influence on the stiffness of the dielectric. Here this influence will be derived in case of a square sheet actuator. The derivation will be done on a unit cell of the actuator, see figure F.1.

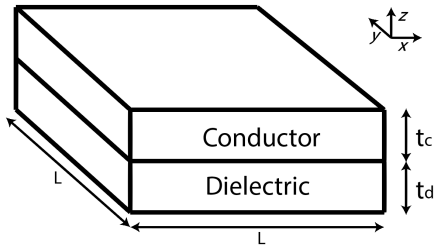

Figure F.1: A unit cell of the square sheet actuator

It is assumed that the used material is incompressible, meaning that the Poisson's ratio in every direction is equal to $\frac{1}{2}$. In this case the elasticity matrix describing both materials is:

$$\begin{bmatrix} \epsilon_{xx} \\ \epsilon_{yy} \\ \epsilon_{zz} \\ 2\epsilon_{xy} \\ 2\epsilon_{xz} \\ 2\epsilon_{yz} \end{bmatrix} = \begin{bmatrix} \frac{1}{E_x} & -\frac{1}{2E_y} & -\frac{1}{2E_z} & 0 & 0 & 0 \\ -\frac{1}{2E_x} & \frac{1}{E_y} & -\frac{1}{2E_z} & 0 & 0 & 0 \\ -\frac{1}{2E_x} & -\frac{1}{2E_y} & \frac{1}{E_z} & 0 & 0 & 0 \\ 0 & 0 & 0 & \frac{1}{G_{xy}} & 0 & 0 \\ 0 & 0 & 0 & 0 & \frac{1}{G_{xz}} & 0 \\ 0 & 0 & 0 & 0 & 0 & \frac{1}{G_{yz}} \end{bmatrix} \begin{bmatrix} \sigma_{xx} \\ \sigma_{yy} \\ \sigma_{zz} \\ \sigma_{xy} \\ \sigma_{xz} \\ \sigma_{yz} \end{bmatrix} \tag{F.1}$$

where:

- ϵ_{uu} is the strain in the u direction
- ϵ_{uv} is the shear strain on the plane perpendicular to u in the v direction
- E is the Young's modulus of the material
- G is the modulus of rigidity
- σ_{uu} is the stress in the u direction
- σ_{uv} is the shear stress on the plane perpendicular to u in the direction v

By using that no shear will be applied and that the situation is symmetric in the $x-$ and the $y-$directions ($\sigma_{xx} = \sigma_{yy}, \epsilon_{xx} = \epsilon_{yy}, E_x = E_y$) this matrix can be reduced to:

$$\begin{bmatrix} \epsilon_{xx} \\ \epsilon_{zz} \end{bmatrix} = \begin{bmatrix} \frac{1}{2E_x} & -\frac{1}{2E_z} \\ -\frac{1}{E_x} & \frac{1}{E_z} \end{bmatrix} \begin{bmatrix} \sigma_{xx} \\ \sigma_{zz} \end{bmatrix} \tag{F.2}$$

This equation will be used to describe the conductor and the dielectric. Furthermore it will be used that the electrode and the dielectric are connected in the $x-$direction (and due to the

symmetry also in the $y-$direction). Therefore the strains of the dielectric and the conductor have to be the same:

$$\epsilon_{xx,d} = \epsilon_{xx,c} \tag{F.3}$$

where $\epsilon_{xx,d}$ and $\epsilon_{xx,c}$ are respectively the strain in the $x-$direction of the dielectric and the conductor. Furthermore this connection implies the total force in that direction must be zero.

$$\sigma_{xx,c} t_c L + \sigma_{xx,d} t_d L = 0 \tag{F.4}$$

where $\sigma_{xx,d}$ is the stress in the conductor in the $x-$direction and t_c, t_d and L geometry parameters defined in figure F.1. The combination of F.2, F.3 and F.4 results in a set of 6 six equations with 8 unknowns (all σ's and ϵ's)

$$\begin{cases} \epsilon_{xx,d} = \frac{1}{2E_x}\sigma_{xx,d} - \frac{1}{2E_z}\sigma_{zz,d} \\ \epsilon_{zz,d} = -\frac{1}{E_x}\sigma_{xx,d} + \frac{1}{E_z}\sigma_{zz,d} \\ \epsilon_{xx,c} = \frac{1}{2E_x}\sigma_{xx,c} - \frac{1}{2E_z}\sigma_{zz,c} \\ \epsilon_{zz,c} = -\frac{1}{E_x}\sigma_{xx,c} + \frac{1}{E_z}\sigma_{zz,c} \\ \epsilon_{xx,d} = \epsilon_{xx,c} \\ \sigma_{xx,c} t_c L + \sigma_{xx,d} t_d L = 0 \end{cases} \tag{F.5}$$

This set of equations can be reduced to two equations. This is done using Wolfram Mathematica, by first eliminating $\sigma_{xx,c}$, $\sigma_{xx,d}$, $\epsilon_{xx,c}$ and $\epsilon_{xx,d}$ and then solving the resulting set of equations for $\epsilon_{zz,d}$ and $\epsilon_{zz,c}$. This results in the following equations:

$$\epsilon_{zz,d} = \epsilon_{zz,c} = K_c \sigma_{zz,c} + K_d \sigma_{zz,d} \tag{F.6}$$

with:

$$\begin{aligned} K_c &= \frac{1}{E_{z,c}} \frac{1}{1 + \frac{E_{x,d} t_d}{E_{x,c} t_c}} \\ K_d &= \frac{1}{E_{z,d}} \frac{1}{1 + \frac{E_{x,c} t_c}{E_{x,d} t_d}} \end{aligned} \tag{F.7}$$

This equation can be used to derive the effective Young's modulus of the dielectric, defined as the strain due to a stress working only on the dielectric. Which can be used to calculated the strain of an unconstrained actuator, under influence of an electrostatic force.

$$\begin{aligned} Y'_d &= \frac{1}{K_c} \\ &= Y_{z,d}\left(1 + \frac{E_{x,c} t_c}{E_{x,d} t_d}\right) \end{aligned} \tag{F.8}$$

where $E_{z,d}$ is the Young's modulus of the dielectric in the $z-$direction, $E_{x,c}$ and $E_{x,d}$ are the Young's moduli in the $x-$direction of respectively the conductor and the dielectric and t_c and t_d are the thickness of the conductor and the dielectric.

Furthermore this equation can be used to calculate the effective Young's modulus of the total actuator, which is defined as the strain due to the a stress working on both the dielectric and

the conductor. This Young's modulus is useful for calculating the power density of the actuator or when using the actuator as a sensor as in Appendix J.

$$\begin{aligned} Y'_{\text{tot}} &= \frac{1}{K_c + K_d} \\ &= E_{z,c} E_{z,d} \frac{E_{x,c}\, t_c + E_{x,d}\, t_d}{E_{z,d} E_{x,c}\, t_c + E_{z,c} E_{x,d}\, t_d} \end{aligned} \tag{F.9}$$

G Stability analysis

According to Brochu and Pei (2010) dielectric elastomer actuators may become in-stable when a high electric field is applied. In this section the point of instability for homogeneous linear elastic dielectric and electrodes will be derived. This is not necessarily representative for a real actuator which may not be linear and may be viscoelastic instead of elastic.

In case of a purely linear incompressible elastic dielectric the external force exerted by the dielectric is.

$$\begin{aligned} F_{\mathrm{m}} &= \frac{Y_{\mathrm{d}}^{'} A}{d}(d-d_0) \\ &= \frac{Y_{\mathrm{d}}^{'} V}{d^2}(d-d_0) \end{aligned} \tag{G.1}$$

Where $Y_{\mathrm{d}}^{'}$ is the effective Young's modulus of the dielectric (see Appendix F), A is the area of the dielectric, d is the thickness of the dielectric, V is the volume of the incompressible dielectric and d_0 is the thickness of the dielectric. See Figure G.1 for a drawing of the situation.

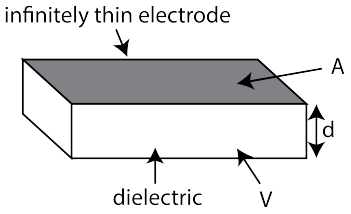

Figure G.1: A drawing of the situation

In this case the electrostatic Maxwell Stress on the dielectric is

$$\begin{aligned} F_{\mathrm{e}} &= \frac{1}{2}\frac{\epsilon_0 \epsilon_r A U^2}{d^2} \\ &= \frac{1}{2}\frac{\epsilon_0 \epsilon_r U^2 V}{d^3} \end{aligned} \tag{G.2}$$

Where ϵ_0 is the vacuum permittivity, ϵ_r is the relative permittivity of the dielectric and U is the applied voltage. Balancing the forces of equation G.1 and G.2 results in the following equilibrium position

$$\begin{aligned} F_{\mathrm{m}} + F_{\mathrm{e}} = 0 \rightarrow \\ d_{\mathrm{eq}} = \frac{1}{2}d_0 + \frac{1}{2}\sqrt{d_0^2 - 2\frac{\epsilon_0 \epsilon_r U^2}{Y_{\mathrm{d}}^{'}}} \end{aligned} \tag{G.3}$$

Furthermore the effective spring constant due to the Maxwell stress and the stiffness of the dielectric is

$$k = -\frac{Y_{\mathrm{d}}^{'} V}{d^3}(d-2d_0) - \frac{3}{2}\frac{\epsilon_0 \epsilon_r U^2 V}{d^4} \tag{G.4}$$

The point of instability can be found at the point where the effective spring constant is equal to zero:

$$k = 0 \rightarrow d_{\text{inst}} = d_0 - \sqrt{d_0^2 - \frac{3}{2}\frac{\epsilon_0 \epsilon_r U^2}{Y_{\text{d}}^{'}}} \tag{G.5}$$

The voltage for which an unloaded actuator is expected to become instable, can be found by looking at the point where the equilibrium position (equation G.3) is equal to the point of instability (equation G.5).

$$U_{\text{max}} = \pm\sqrt{\frac{1}{2}\frac{d_0^2 Y_{\text{d}}^{'}}{\epsilon_0 \epsilon_r}} \tag{G.6}$$

At this voltage the thickness of the actuator is

$$d = \frac{1}{2} d_0 \tag{G.7}$$

Therefore it can be concluded that in case of a homogeneous linear incompressible elastic dielectric with infinitely thin electrodes, the maximum strain that can be achieved before an unconstrained actuator becomes in-stable is 50 %.

H Dynamic analysis of a cantilever beam

In this section the dynamic behaviour of a composite cantilever will be determined.

H.1 Neutral axis

To calculate the dynamic behaviour of the cantilever first of all the neutral axis of the cantilever will have to be calculated. The position of the neutral axis can be calculated by using that the total moment working on the cross-section must be equal to zero (Gramoll, 2017).

$$E_1 y_1 A_1 + E_2 y_2 A_2 + E_3 y_3 A_3 = 0 \tag{H.1}$$

where A_i is the area of the cross-section i, E_i is the Young's modulus of cross-section i and y_i is the position of the center of cross-section i relative to the neutral axis. For all cross-sections this position depends only on the location of the neutral axis and the geometry.

$$\begin{aligned} y_1 &= \frac{t_1}{2} - y_0 \\ y_2 &= t_1 + \frac{t_2}{2} - y_0 \\ y_3 &= t_1 + t_2 + \frac{t_3}{2} - y_0 \end{aligned} \tag{H.2}$$

When these equations are combined with the previous equation, an equation from which the distance between the neutral axis and the bottom of the cantilever can be calculated is obtained.

$$y_0 = \frac{1}{2} \frac{A_1 E_1 t_1 + A_2 E_2 (2t_1 + t_2) + A_3 E_3 (2t_1 + 2t_2 + t_3)}{A_1 E_1 + A_2 E_2 + A_3 E_3} \tag{H.3}$$

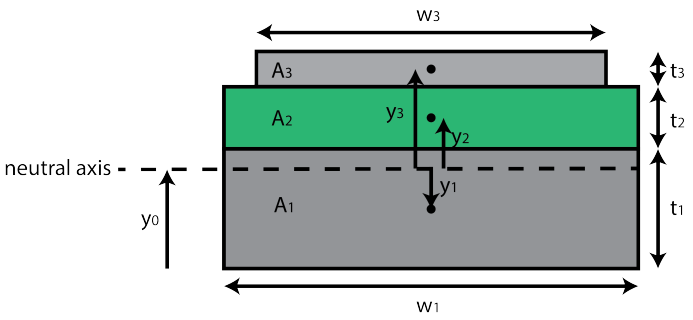

Figure H.1: A drawing of the cross-section of the cantilever

H.2 Differential equation

The differential equation of the system will be derived from the Lagrangian of the system (see Balachandran and Magrab (2009) section 9.2).

$$\mathscr{L} = \int_0^L \frac{1}{2} S \left(\frac{\partial^2 w(x,t)}{\partial x^2} \right)^2 + \lambda \left(\frac{\partial w(x,t)}{\partial t} \right)^2 dx \tag{H.4}$$

Where S is the total moment per curvature.

$$S = E_1 I_1 + E_2 I_2 + E_3 I_3 \tag{H.5}$$

With E_i the Young's modulus of material i and I the second moment of area of the material, relative to the neutral axis.

$$I_i = \int_{-\frac{t_i}{2}+y_i}^{\frac{t_i}{2}+y_i} \int_0^{w_i} y^2 \, dx \, dy = \frac{1}{12} w_i t_i^3 + t_i w_i y_i^2 \tag{H.6}$$

And λ is the mass per unit length of the beam

$$\lambda = A_1 \rho_1 + A_2 \rho_2 + A_3 \rho_3 \tag{H.7}$$

Where A_i is the cross-sectional area of material i and ρ_i is the density of material i. To derive a differential equation from the Lagrangian it will be used that the action of system is always constant Feynman et al. (1963b). The action of a system is defined as

$$S = \int_{t_1}^{t_2} \mathscr{L} \, dt \tag{H.8}$$

The conditions under which the action is constant can be calculated using calculus of variations. According to Balachandran and Magrab (2009) the action of the system is constant in case the following conditions are met. The displacement and the rotation at the fixed end of the cantilever are zero, the sum of the forces and the moments on the free end of the cantilever are zero and

$$S \frac{\partial^4 w(x,t)}{\partial x^4} + \lambda \frac{\partial^2 w(x)}{\partial t^2} = f(x,t) \text{ for } 0 < x < L \tag{H.9}$$

Where $f(x,t)$ is the externally applied force density.

H.3 Solution in case of no externally applied forces

In case there is no externally applied force density, so no damping or external excitation, equation H.9 simplifies to.

$$S \frac{\partial^4 w(x,t)}{\partial x^4} + \lambda \frac{\partial^2 w(x,t)}{\partial t^2} = 0 \text{ for } 0 < x < L \tag{H.10}$$

With:

$$\begin{aligned} w(0,t) &= 0 \\ \left.\frac{\partial w(x,t)}{\partial x}\right|_{x=0} &= 0 \\ S \left.\frac{\partial^2 w(x,t)}{\partial x^2}\right|_{x=L} &= 0 \\ S \left.\frac{\partial^3 w(x,t)}{\partial x^3}\right|_{x=L} &= 0 \end{aligned} \tag{H.11}$$

To solve this equation the separation of variables approach will be used (Whitney, 1999). This approach starts by doing the assumption that the solution consists of a part that depends only on time and a part that depends only on the position along the beam.

$$w(x,t) = X(x) f(t) \tag{H.12}$$

When this is equation is substituted in equation H.10, the result is

$$\frac{S}{\lambda X(x)} \frac{\partial^4 X(x)}{\partial x^4} = -\frac{1}{f(t)} \frac{\partial^2 f(t)}{\partial t^2} \tag{H.13}$$

Since the left part only depends on position and the right part only depends on time, both must be constant. Here this constant is chosen to be ω^2. For the time dependent part this results in the following relation.

$$\frac{\partial^2 f(t)}{\partial t^2} = -\omega^2 f(t) \tag{H.14}$$

Which can be solved by

$$f(t) = e^{-i\omega t} \tag{H.15}$$

For the position dependent part the differential equation is:

$$\frac{\partial^4 X(x)}{\partial x^4} = k^4 X(x) \tag{H.16}$$

with:

$$k^4 = \frac{\lambda\omega^2}{S} \tag{H.17}$$

This equation can be solved via the Laplace domain, using the rule for transforming differentiated signal into the Laplace domain (Weisstein, 2017b).

$$\mathscr{L}_t\left[f^{(n)}(t)\right](s) = s^n \mathscr{L}_t\left[f(t)\right] - s^{n-1} f(0) - s^{n-2} f'(0) - ... - f^{n-1}(0) \tag{H.18}$$

Using this rule the fourier transform of $X(x)$ can be calculated.

$$\hat{X}(s) = \frac{sC + D}{s^4 - k^4} \tag{H.19}$$

Where it is used that $X(0) = 0$ since there is a boundary condition $w(0,t) = 0$, that $\left.\frac{\partial X(x)}{\partial x}\right|_{x=0} = 0$ since there is a boundary condition $\left.\frac{\partial w(x,t)}{\partial x}\right|_{x=0} = 0$ and that C and D are defined as:

$$\begin{aligned} C &= \left.\frac{\partial^2 w}{\partial x^2}\right|_{x=0} \\ D &= \left.\frac{\partial^3 w}{\partial x^3}\right|_{x=0} \end{aligned} \tag{H.20}$$

The inverse transform of $\hat{X}(s)$ is calculated using Wolfram Mathematica.

$$X(x) = \frac{1}{2}\frac{C}{k^2}(\cosh(kx) - (\cos(kx)) + \frac{1}{2}\frac{D}{k^3}((\sinh(kx) - (\sin(kx)) \tag{H.21}$$

To get a relation for the oscillation frequency the remaining two boundary conditions from equation H.11 will be used.

$$\begin{aligned} \left.\frac{\partial^2 X(x)}{\partial x^2}\right|_{x=L} &= \frac{1}{2}C(\cosh(kL) + \cos(kL)) + \frac{1}{2}\frac{D}{k}(\sinh(kL) + \sin(kL)) = 0 \\ \left.\frac{\partial^3 X(x)}{\partial x^3}\right|_{x=L} &= \frac{1}{2}kC(\sinh(kL) - \sin(kL)) + \frac{1}{2}\frac{D}{k}(\cosh(kL) + \cos(kl)) = 0 \end{aligned} \tag{H.22}$$

By using that $\cos^2(kL) + \sin^2(kL) = 1$ and that $\cosh^2(kL) - \sinh^2 kL = 1$ this set of equations can be reduced to:

$$\cos(kL)\cosh(kL) = -1 \tag{H.23}$$

Which has it's firsts solutions for: (Whitney, 1999)

$$kL = \sqrt[4]{\frac{\lambda\omega^2}{S}}L = 1.875 \tag{H.24}$$

Therefore the lowest eigenfrequency of the cantilever is located at:

$$f_1 = \frac{1}{2\pi}\sqrt{1.875^4\frac{S}{\lambda L^4}} \tag{H.25}$$

H.4 Energy density

In this section the energy stored in bending the cantilever in a static situation will be calculated. This energy can be divided by the volume of the cantilever to obtain the work density of the actuator. The derivation will start with the the energy stored in bending the cantilever (Balachandran and Magrab (2009) section 9.2):

$$U = \int_0^L \frac{1}{2}S\left(\frac{\partial^2 w(x)}{\partial x^2}\right)^2 dx \tag{H.26}$$

where U is the energy stored in bending the beam and $w(x)$ is the deflection of the beam. In the static case the influence of the inertia on the beam is negligible. In this case the moment due to the Maxwell stress is the only moment working on the beam. The moment due to the Maxwell stress will be independent on the position on the beam, since Maxwell stress will be approximately independent on the position of the beam since the beam is very thin. Therefore in the static case the curvature of the beam will be constant and can be calculated using

$$\begin{aligned} w(x_{\text{laser}}) &= \int_0^{x_{\text{laser}}}\int_0^{x_{\text{laser}}} \rho\, dx dx \\ &= \frac{1}{2}\rho x_{\text{laser}}^2 \end{aligned} \tag{H.27}$$

where x_{laser} is the location where the deflection is measured and ρ is the curvature of the beam. By substituting this equation into Equation H.26, the following equation is obtained.

$$\begin{aligned} U &= \frac{1}{2}LS\rho^2 \\ &= 2\frac{w(x_{\text{laser}})^2 L}{x_{\text{laser}}^4} \end{aligned} \tag{H.28}$$

where x_{laser} is the location where the deflection is measured, $w(x_{\text{laser}})$ is the deflection at the point where the deflection is measured and L is the length of the cantilever.

I FEM simulation of Young's modulus measurement setup

In the measurement setup used to measure the Young's modulus in the $y-$direction, a rectangular piece of material is being stretched while being clamped at both ends. This will cause a stress in directions other than the direction the material is stretched in near where the sample is clamped. The effect of these stresses on the measured stiffness will be discussed in this appendix based on a FEM simulation made with Comsol.

I.1 Assumptions and Parameters

The simulation is performed on a block of material of 20x10x2 mm using the Solid Mechanics module in Comsol. To simulate the situation of clamped electrodes, one side of the beam is fixed and a displacement element is is applied to the other side. This displacement element consists of the displacement due to the stretching of the material and a displacement of zero in the other directions due to the fact that the electrodes are clamped at the end, see figure I.1.

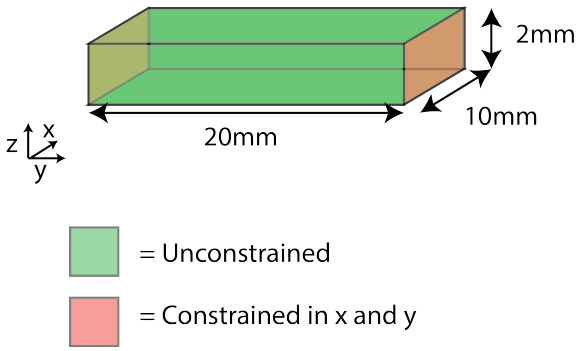

Figure I.1: A drawing of the simulated situation

The Young's modulus of the material is set to 2 MPa. The Poisson's ratio of the material is set to 0.4999, to simulate a nearly incompressible material.

I.2 Results

The stress distribution in the beam at a strain of 10 % is plotted in figure I.2. To calculate the average pressure applied to the beam, the stress in the $y-$direction is integrated over the constrained side of the beam. The average pressure and the pressure expected in case there was a uniforms stress in the material (see equation 5.3.1) is plotted in figure I.3. The average stress divided by the strain of the beam is 2.028 MPa for all the simulated strains .

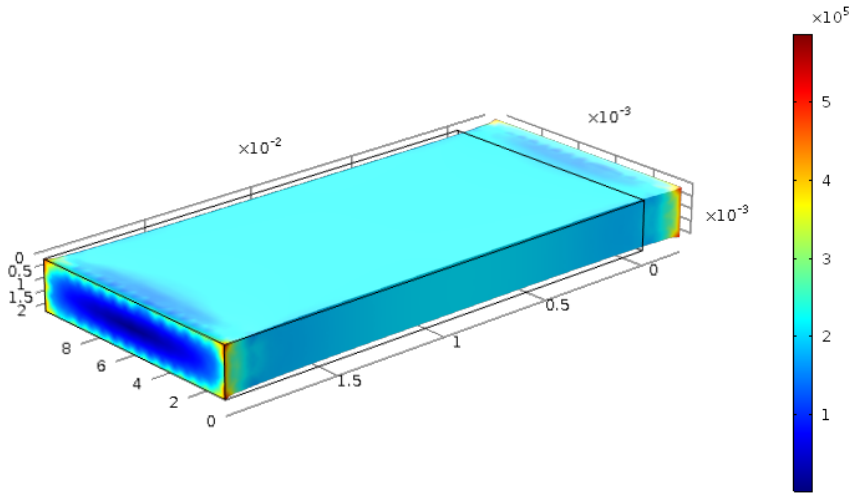

Figure I.2: The Von Mises stress (in Pa) in the beam at a strain of 10 %

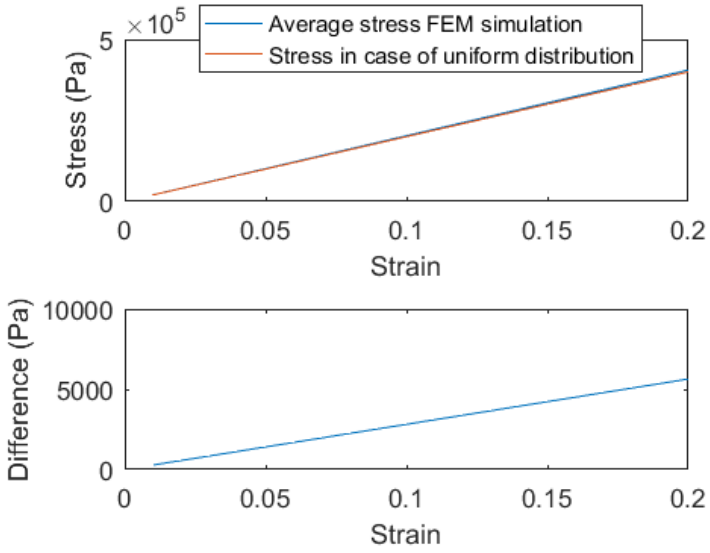

Figure I.3: Average stress in the $y-$direction and the stress in case of a uniform stress distribution

I.3 Conclusion

The FEM simulation performed in this section shows that the deviation of the effective Young's modulus from the real Young's modulus due to stresses in the $x-$ and $z-$direction is 1.4 % for a completely constrained sample. In practice the sample will not be fully constrained and therefore the deviation is expected to be less than 1.4 % and therefore will be neglected.

J Capacitive force sensor paper

3D Printed Flexible Capacitive Force Sensor with a Simple Micro-Controller Based Readout

Martijn Schouten, Remco Sanders and Gijs Krijnen
Robotics And Mechatronics group
University of Twente
Enschede, The Netherlands
m.schouten-1@alumnus.utwente.nl

***Abstract* - This paper describes the development of a proof of principle of a flexible force sensor and the corresponding readout circuit. The flexible force sensor consists of a parallel plate capacitor that is 3D printed using regular and conductive thermoplastic poly-urethane (TPU). The capacitance change due to an applied sinusoidal force is measured using an LCR meter. A proof of principle, using an oscillatory readout circuit consisting of only an operational amplifier and a frequency-counter based on an Arduino Nano, is provided. This indicates the possibility to implement low-cost capactive sensors into 3D printed objects, which is especially interesting for customised robotic and prosthetic applications.**

Keywords - Capacitive Sensors; Elastomer; TPU, 3D printing; Force sensor; Fused Deposition Modeling

I. Introduction

3D printed sensors can easily be customised and therefore might find use in custom products in for example medical or sports applications. Also since complexity is cheap in additive manufacturing, it may become economically interesting to use the technique to fabricate complex robotic systems. Due to todays availability of flexible filaments, dielectric as well as electrically conductive, it now becomes possible to 3D print flexible sensors of all kinds, e.g. for soft robotic applications.

In relation to this work Saari et al. earlier described a 3D printed force sensor that used an elastomer as dielectric and stiff electrodes fabricated from copper wires embedded during printing [1]. Another 3D printed capacitive sensor that used wires as electrodes has been fabricated by Shemelya et al. [2]. However, 3D printed flexible capacitive sensors have not been presented in literature yet.

A. Sensing principle

The force sensors described in this work are based on the measurement of the change in capacitance in between two flexible conductors, see Fig. 1. The change in capacitance arises due to the fact that the material is flexible and therefore will be easily deformed when a force is applied.

The capacitance of the sensor can be approximated by two parallel plates with a flexible dielectric in between. Since the distance between the plates is much smaller than the dimensions of the electrodes ($6.4\,\mathrm{mm}$ x $36\,\mathrm{mm}$ versus $0.2\,\mathrm{mm}$), the capacitance can be calculated using the parallel plate approximation. Data of generic thermoplastic polyurethanes

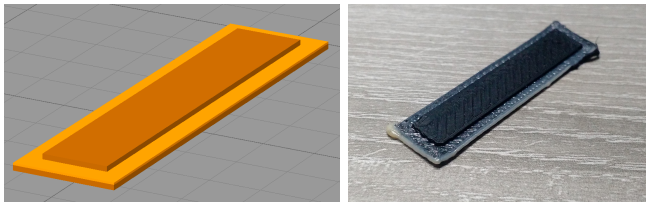

Fig. 1. Left: a CAD drawing of the proposed sensor used to print the sensor. Right: a picture of the actual sensor

suggest that the Poisson's ratio of polyurethane is close to 0.5 [3]. Therefore when the dielectric is compressed the area of the electrodes increases, such that the total volume (V) of polyurethane will roughly stay the same, leading to:

$$C = \frac{\epsilon_r \epsilon_0 A}{d} = \frac{\epsilon_r \epsilon_0 V}{d^2} \tag{1}$$

where A is the area of the plates, d is the distance in between the plates, ϵ_r is the relative dielectric constant of the dielectric, ϵ_0 is vacuum permittivity and C is the capacitance of the sensor. For small changes around an initial area A_0 and an initial thickness d_0 the change in capacitance is found from the partial derivative of C with respect to d:

$$\Delta C = \left.\frac{\partial C}{\partial d}\right|_{d \to d_0} \Delta d = -2\frac{\epsilon_r \epsilon_0 A_0}{d_0^2}\Delta d \tag{2}$$

Note that the change in capacitance for this in-compressible dielectric is twice as large as for a compressible dielectric, since the area of the capacitor plates also changes. In the situation where the material is used in its linear range, the following equation can be used

$$\Delta d = -\frac{F d_0}{A_0 E'} \tag{3}$$

Where E' is the effective Young's modulus of the material in this situation where it is placed in between two stiffer electrodes and F is the compressive force that is applied. When (3) is combined with (2), a relation for the expected capacitance change is obtained.

$$\Delta C = \frac{2\epsilon_r \epsilon_0}{d_0 E'} F \tag{4}$$

Therefore in the linear regime there is no dependence of the capacitance change on the capacitor area. At last, since both the

dielectric constant and thickness of the material are not known accurately, using (1) a convenient expression is obtained:

$$\frac{\Delta C}{C} = \frac{2}{AE'}F \tag{5}$$

II. Methodology

A. Sensor fabrication

The sensors are printed using a Flashforge Creater Pro printer that is equipped with a Flexion extruder from Diabase Engineering, in order to be able to print flexible filaments. The dielectric consists of Flexion X60 Ultra-Flexible Filament by MakeShaper. The electrodes are made from 85-700+ PI-ETPU filament kindly supplied by Palmiga Innovations.

Both materials are printed with a 100% infill at a layer height of $100\,\mu\mathrm{m}$. An image of the CAD model used to print the sensors can be found in Fig. 1. In this image light orange indicates X60 and dark orange PI-ETPU.

The thickness of respectively the bottom electrode, the dielectric and the top electrode are $500\,\mu\mathrm{m}$, $200\,\mu\mathrm{m}$ and $500\,\mu\mathrm{m}$. The size of the top electrode in the CAD file is 36 x $6.4\,\mathrm{mm}$ and the size of the bottom electrode is 40 x $10\,\mathrm{mm}$

B. Measurement setup

The sensor is mounted in a sample holder which is laser cut out of Delrin, see Fig. 2 for a drawing and Fig. 3 for a picture of the measurement setup. The sensor is tested by applying a well defined force using a linear actuator (SMAC LCA25-050-15F) and monitoring the capacitance. The actuator is configured to load the sensor with a combination of a constant plus a sinusoidal force since no negative forces can be applied with this setup and it has to be kept in place.

C. Sensor read-out

The fabricated sensors have been interrogated in two ways: by an LCR meter for accurate characterisation and by an Arduino based read-out to demonstrate the possibility for a low-cost sensor-interface.

1) Read-out by LCR meter: The sensor was characterised using an HP4842a LCR meter operating at a frequency of $25\,\mathrm{kHz}$ and a voltage of $1\,\mathrm{V}$. It was configured for a 4 wire measurement and therefore is connected to the sample using 4 shielded cables. The cores of the two cables of the high and the two cables of the low side are connected near the measurement setup. The grounds of all four cables are also connected near the measurement setup. The capacitance measured by the LCR meter when only the cables are connected is less than $1\,\mathrm{pF}$.

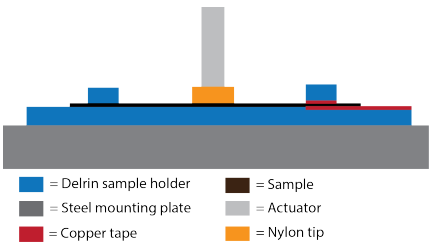

Fig. 2. A schematic representation of the measurement setup

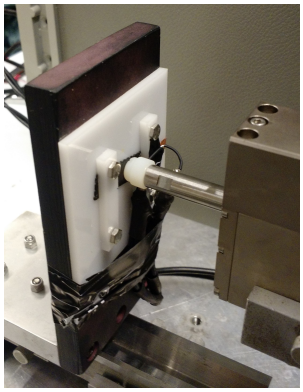

Fig. 3. The measurement setup

2) Oscillator and frequency counter: As a proof of principle a readout circuit has been built using an Astable Op-amp multi vibrator circuit (Fig. 4). The oscillation frequency of this oscillator can be calculated using the following equation [4]:

$$f_0 = \frac{1}{2R_1 C \ln\left(\frac{1+\beta}{1-\beta}\right)} \text{ with } \beta = \frac{R_3}{R_2 + R_3} \tag{6}$$

Combining (5) and (6) it can be shown that in the ideal case of no parasitic capacitances the fractional resonance frequency change is given by:

$$\frac{\Delta f_0}{f_0} = -\frac{2}{AE'}F \tag{7}$$

hence giving a linear relation between relative oscillation frequency and force.

The oscillation frequency of the multivibrator is determined by using an Arduino Nano, which contains an Atmega328 from Atmel. One of the Atmega328's 8-bit counter's is programmed such that it uses the multivibrator's output signal as a clock. Every $400\,\mu\mathrm{s}$ the oscillation frequency is calculated based on the number of periods that were observed by the 8-bit counter. The capacitance of 50 calculations ($20\,\mathrm{ms}$) is averaged in order to filter out as much $50\,\mathrm{Hz}$ noise as possible.

III. Results

A. Basic sensor characteristics

The resistance between the bottom and the top electrode was measured to be $80\,\mathrm{M\Omega}$. The resistance from one side of the bottom electrode to the other end showed $10\,\mathrm{k\Omega}$. The resistance

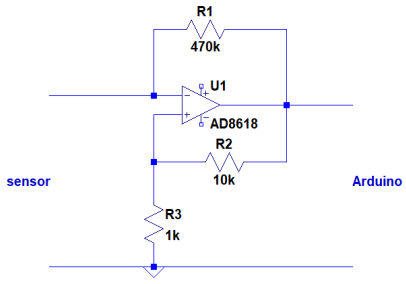

Fig. 4. The Astable Op-amp multivibrator

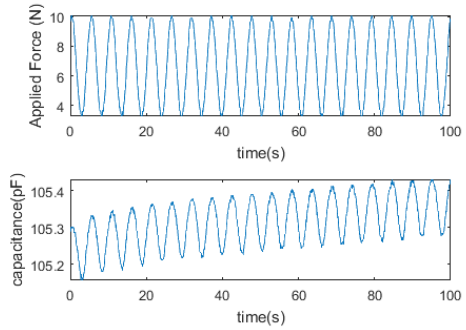

Fig. 5. Sinusoidal force excitation (top) and sensor response (bottom) as measured by an LCR meter

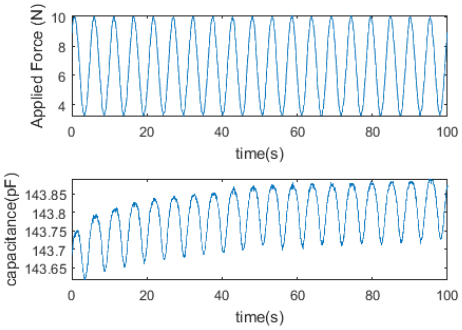

Fig. 7. Response of the sensor at a sinusoidal excitation, measured using the Arduino based readout circuit

of the top electrode was $20\,\mathrm{k\Omega}$.

B. Capacitive measurements

1) LCR meter: Fig. 5 shows the response of the LCR meter at a sinusoidal excitation of $0.2\,\mathrm{Hz}$. In Fig. 6 the capacitance of the sensor is plotted against the force applied to the sensor. The colour in this plot corresponds to the time axis in figure 5. The Signal-to-noise and distortion ratio (SINAD) of the measured capacitance is $19.7\,\mathrm{dB}$. The Signal-to-Noise Ratio (SNR), when excluding the drift by not taking into account signals below $0.05\,\mathrm{Hz}$, is $38\,\mathrm{dB}$.

2) Arduino based readout circuit: Fig. 7 shows the capacitance of the sensor as measured by the read-out circuit build with an Arduino and an op-amp when the sensor is excited with a sinusoidal force. An estimate of the parasitic capacitance of the readout circuit can be obtained by comparing the data in Fig. 7 and Fig. 5, since the parasitic capacitance of the LCR meter is negligible. This indicates a parasitic capacitance of $38\,\mathrm{pF}$. The SINAD of the measured capacitance is $12.8\,\mathrm{dB}$. The SNR, when excluding the drift by not taking into account signals below $0.05\,\mathrm{Hz}$, is $28\,\mathrm{dB}$.

IV. Discussion and Conclusion

The measured capacitance change is $160\,\mathrm{fF}$ at a change in force of $6.6\,\mathrm{N}$. When no pressure is applied the sensor has a capacitance of $105.22\,\mathrm{pF}$ for a top electrode area of $2.3\,\mathrm{cm}^2$. According to (5) these values correspond to an effective Young's modulus of $38\,\mathrm{MPa}$, which is high compared to an estimate of the Youngs modulus of X60 based on it's shore hardness of 60A [5], which is $3\,\mathrm{MPa}$ [6]. This high value could be caused by the restricted lateral expansion of the X60 due to the relative stiffness of the electrodes or by the anisotropy of the 3D printed material. If this is the case the sensitivity of the sensor might be increased by printing the dielectric using a lower infill percentage, in order to reduce the Poisson ratio of the dielectric and benefit from density modulation.

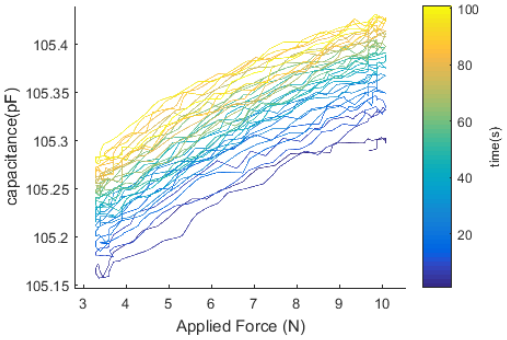

Fig. 6. The capacitance plotted against the applied force

The results obtained using the LCR meter also show that the sensors drift. This drift might at least partially be explained by the creep of the material as a result of the DC-offset in the force.

The micro-controller based readout circuit has a smaller SINAD and SNR than the LCR meter. However the observed noise suggests that sub Newton forces may be measured. To improve the read-out signal the parasitic capacitance may be reduced and a commercial capacitance to digital converter chip might be used. Finally it should be noted that a possible effect of the resistance of the electrodes on the measured capacitance can not yet be ruled out.

In conclusion we have shown a 3D printed flexible capacitive force sensor with cost-effective read-out sensor that may have a high potential for use in soft robotic and prosthetic devices. Due to its flexibility and the ease by which it can be made in large surfaces it may possibly be applied as artificial tactile skin in soft robotics.

References

[1] M. Saari, B. Xia, B. Cox, P. S. Krueger, A. L. Cohen, and E. Richer, "Fabrication and Analysis of a Composite 3D Printed Capacitive Force Sensor," *3D Printing and Additive Manufacturing*, vol. 3, no. 3, pp. 136–141, September 2016.

[2] C. Shemelya, F. Cedillos, E. Aguilera, D. Espalin, D. Muse, R. Wicker, and E. MacDonald, "Encapsulated copper wire and copper mesh capacitive sensing for 3-d printing applications," *IEEE Sensors Journal*, vol. 15, no. 2, pp. 1280–1286, Feb 2015.

[3] H. Qi and M. Boyce, "Stressstrain behavior of thermoplastic polyurethanes," *Mechanics of Materials*, vol. 37, no. 8, pp. 817 – 839, 2005.

[4] (2017). [Online]. Available: http://www.electronics-tutorials.ws/opamp/op-amp-multivibrator.html

[5] (2017). [Online]. Available: https://flexionextruder.com/shop/x60-ultra-flexible-filament-black/

[6] (2017). [Online]. Available: http://www.dowcorning.com/content/publishedlit/11-3716-01_durometer-hardness-for-silicones.pdf

K Print settings

K.1 Conductors

Table K.1: Used print settings for Blackmagic conductive TPU

Layer height	100 µm
Print temperature	210 °C
Nozzle diameter	0.8 mm
Extrusion multiplier	4
Extrusion width	1.92 mm
Fan speed	90 %
Default print speed	2000 mm s^{-1}
Flexion Cam-roller setting	2

Table K.2: Used print settings for PI-ETPU 85-700+ and PI-ETPU 95-250

Layer height	100 µm
Print temperature	210 °C
Nozzle diameter	0.8 mm
Extrusion multiplier	1.25
Extrusion width	0.7 mm
Fan speed	90 %
Default print speed	2000 mm s^{-1}
Flexion Cam-roller setting	2

Table K.3: Used print settings for Electrifi

Layer height	100 µm
Print temperature	140-160 °C
Nozzle diameter	0.8 mm
Extrusion multiplier	1.3
Extrusion width	0.8 mm
Fan speed	100 %
Default print speed	2000 mm s^{-1}
Flexion Cam-roller setting	2

Table K.4: Used print settings for Proto Pasta Conductive Filament

Layer height	50 µm
Print temperature	210 °C
Nozzle diameter	0.8 mm
Extrusion multiplier	1.20
Extrusion width	0.7 mm
Fan speed	100 %
Default print speed	2000 mm s^{-1}
Flexion Cam-roller setting	4

K.2 Dielectrics

Table K.5: Used print settings for Ninjaflex

Layer Height	50 µm	100 µm
Print temperature	230 °C	230 °C
Nozzle diameter	0.6 mm	0.6 mm
Extrusion multiplier	1.24	1.3
Extrusion width	0.72 mm	0.55 mm
Fan speed	90 %	90 %
Default print speed	2000 mm s^{-1}	2000 mm s^{-1}
Flexion Cam-roller setting	2	2

Table K.6: Used print settings for X60

Layer Height	100 µm
Print temperature	220 °C
Nozzle diameter	0.6 mm
Extrusion multiplier	1.3
Extrusion width	0.55 mm
Fan speed	100 %
Default print speed	2000 mm s^{-1}
Flexion Cam-roller setting	1

Table K.7: Used print settings for LAY-FOMM

Layer Height	12.5 µm	50 µm	100 µm
Print temperature	225 °C	225 °C	225 °C
Nozzle diameter	0.6 mm	0.6 mm	0.6 mm
Extrusion multiplier	1.1	1.0	1.3
Extrusion width	0.5 mm	0.5 mm	0.55 mm
Fan speed	100 %	100 %	100 %
Default print speed	1000 mm s^{-1}	2000 mm s^{-1}	2000 mm s^{-1}
Flexion Cam-roller setting	2	2	2

Table K.8: Used print settings for GEL-LAY

Layer Height	100 µm
Print temperature	225 °C
Nozzle diameter	0.6 mm
Extrusion multiplier	1.3
Extrusion width	0.65 mm
Fan speed	100 %
Default print speed	2000 mm s^{-1}
Flexion Cam-roller setting	2

L Impedance spectra

L.1 X60 without PC

L.1.1 Impedance Spectroscopy X60 without DC offset

The spectrum of the X60 sample has been measured 10 times. The result of these measurements can be found in figure L.1. The result of the Kronig-Kramer check on the last frequency sweep is shown in Figure L.4.

The parameters resulting from the fit using estimate and boundary conditions as in Table L.2 can be found in Table L.1. The fitted spectrum is plotted together with the measured spectrum in figure L.2, the error between both spectra is plotted in Figure L.3.

The electrode resistance (R1) is not taken into account since it is expected to be very small since steel plates are used. Furthermore the parallel resistance (R4) is not used since no electronic conductance is expected. The Warburg impedance is left out since it was found to be much smaller than the resistance due to charge transfer. The geometry independent parameters derived from these determined equivalent circuit elements can be found in table L.3.

Table L.1: Fitted Parameters

Parameter	Physical Meaning	Value	Error
C1	Geometrical capacitance	200 pF	0.716%
R2	Ionic resistance	3.6 kΩ	0.0233%
Q	Double layer impedance	80.1 $p\Omega^{-1}rad^{-n}s^{n}$	0.000477%
n	Double layer impedance	959 m	0.111%
R3	Resistance due to charge transfer	62.4 MΩ	10%

Table L.2: Estimates and boundaries

Symbol	Estimate	Lower Boundary	Upper Boundary
C1	200 pF	100 pF	400 pF
R2	1 MΩ	100 Ω	100 MΩ
Q	300 $n\Omega^{-1}rad^{-n}s^{n}$	1 $p\Omega^{-1}rad^{-n}s^{n}$	100 $\mu\Omega^{-1}rad^{-n}s^{n}$
n	800 m	300 m	1
R3	10 MΩ	100 Ω	1 GΩ

Table L.3: Geometry independent parameters

Symbol	Physical Meaning	Value
ϵ_r	Dielectric Constant	4.79
σ	Ionic conductivity	1.31 $m\Omega\,m^{-1}$
$z j_0$	Exchange Current density	404 $pA\,m^{-2}$
λ	Debye Length	868 µm
I	Ionic strength	7.35 $pmol\,m^{-3}$

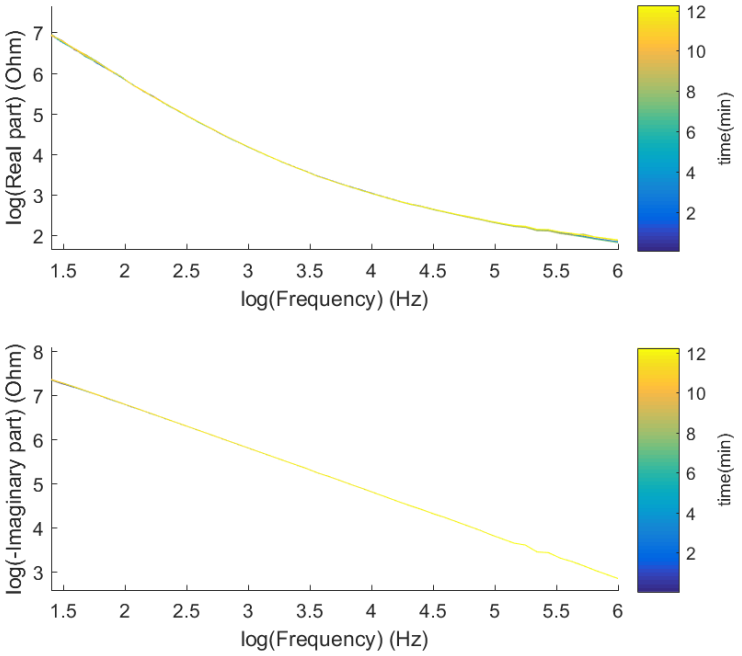

Figure L.1: Drift in the measured spectrum on X60 without offset and PC

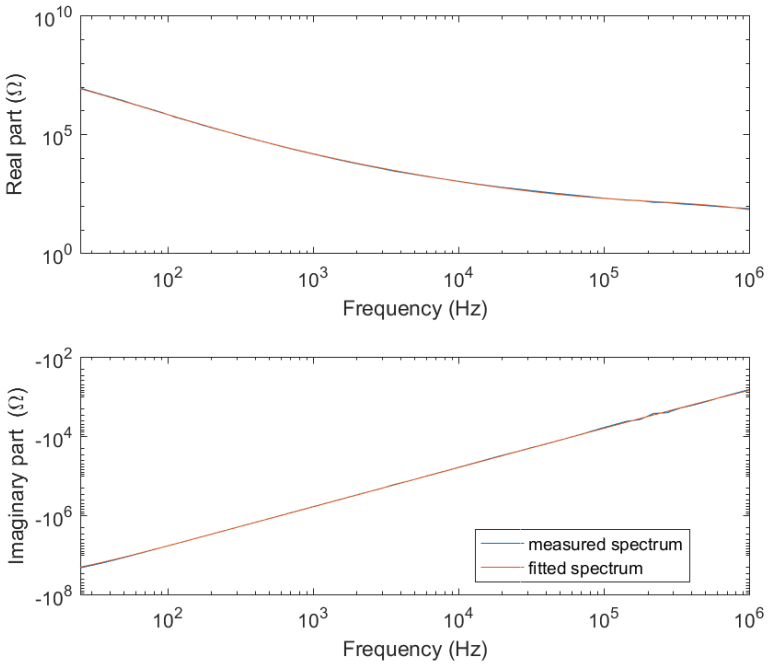

Figure L.2: Last spectrum measured on X60 without offset and PC and the spectrum fitted to it

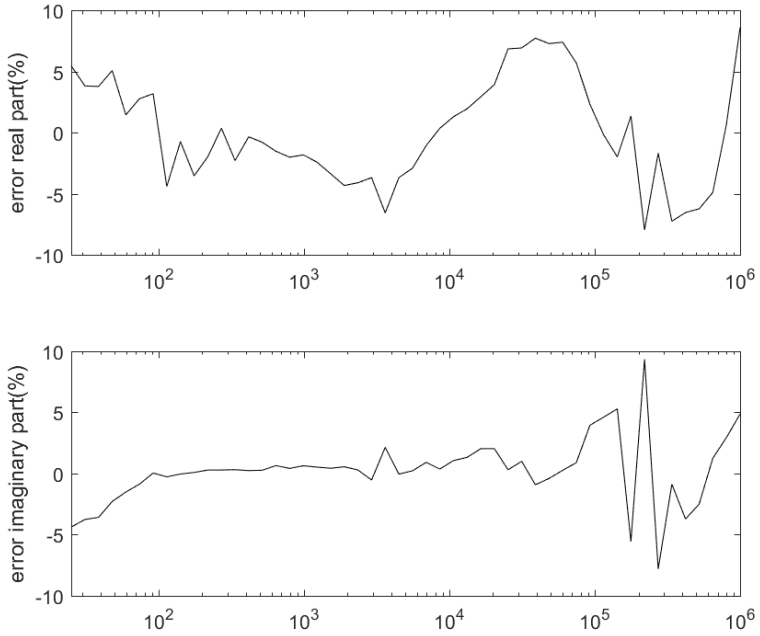

Figure L.3: Error in between the measured and fitted spectrum of X60 without offset and PC

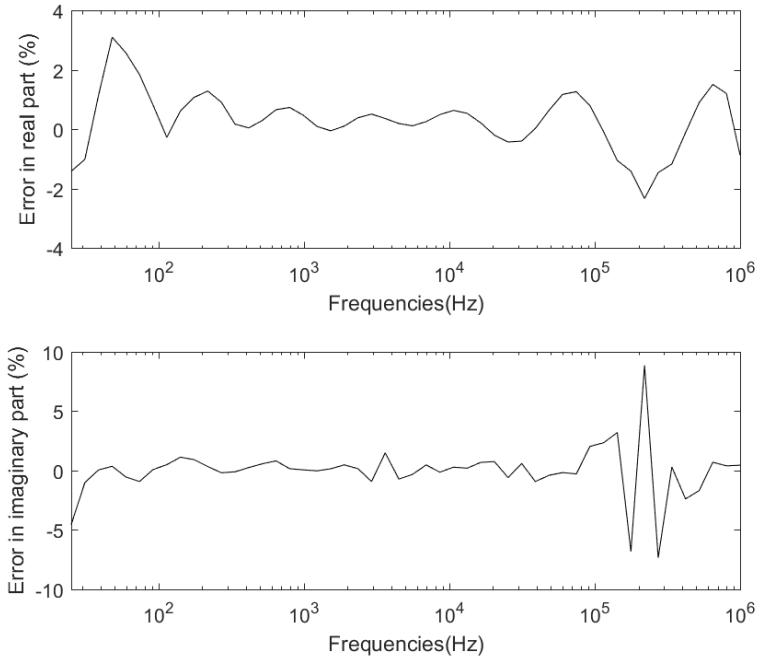

Figure L.4: KKcheck on the last measured spectrum on X60 without offset and PC

L.1.2 Impedance Spectroscopy X60 with DC offset

The spectrum of X60 is also measured in case a DC offset of 10 V is added to the applied signal. The spectrum was measured 5 times, see Figure L.5. The result of the Kronig-Kramer check on the last frequency sweep is shown in Figure L.8.

The parameters resulting from the fit using estimate and boundary conditions as in Table L.5 can be found in Table L.4.The fitted spectrum is plotted together with the measured spectrum in figure L.2, the error between both spectra is plotted in Figure L.3.

Again the electrode resistance (R1) is not taken into account since it is expected to be very small since steel plates are used. Furthermore the parallel resistance (R4) is not used since no electronic conductance is expected. The Warburg impedance is left out since it was found to be much smaller than the resistance due to charge transfer. The geometry independent parameters derived from these determined equivalent circuit elements can be found in table L.6

Table L.4: Fitted Parameters

Parameter	Physical Meaning	Value	Error
C1	Geometrical capacitance	233 pF	0.692%
R2	Ionic resistance	3.68 kΩ	0.0227%
Q	Double layer impedance	88 $p\Omega^{-1}rad^{-n}s^{n}$	0.000455%
n	Double layer impedance	950 m	0.12%
R3	Resistance due to charge transfer	48.1 MΩ	7.1%

Table L.5: Estimates and boundaries

Symbol	Estimate	Lower Boundary	Upper Boundary
C1	200 pF	100 pF	400 pF
R2	1 MΩ	100 Ω	100 MΩ
Q	300 $n\Omega^{-1}rad^{-n}s^{n}$	1 $p\Omega^{-1}rad^{-n}s^{n}$	100 $\mu\Omega^{-1}rad^{-n}s^{n}$
n	800 m	300 m	1
R3	10 MΩ	100 Ω	1 GΩ

Table L.6: Geometry independent parameters

Symbol	Physical Meaning	Value
ϵ_r	Dielectric Constant	5.59
σ	Ionic conductivity	1.28 $m\Omega\,m^{-1}$
zj_0	Exchange Current density	525 $pA\,m^{-2}$
λ	Debye Length	881 µm
I	Ionic strength	8.34 $pmol\,m^{-3}$

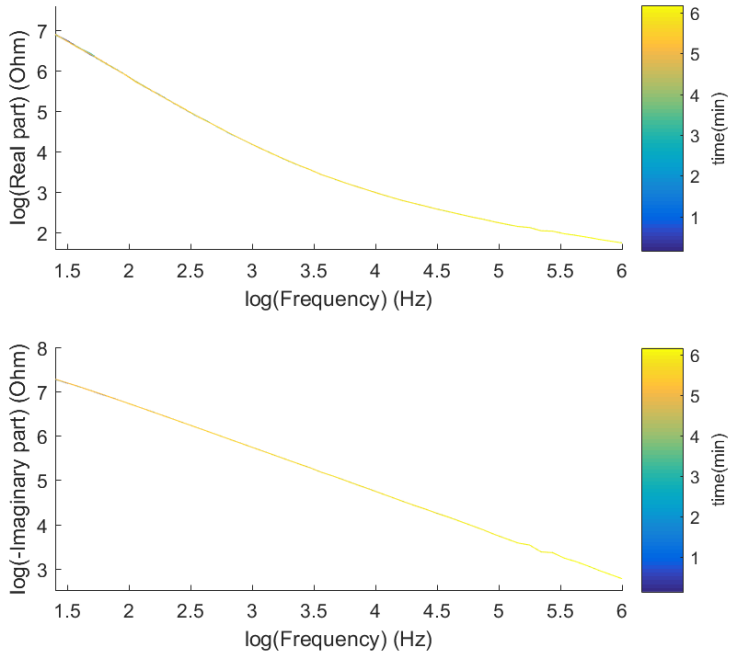

Figure L.5: Drift in the measured spectrum on X60 with offset and without PC

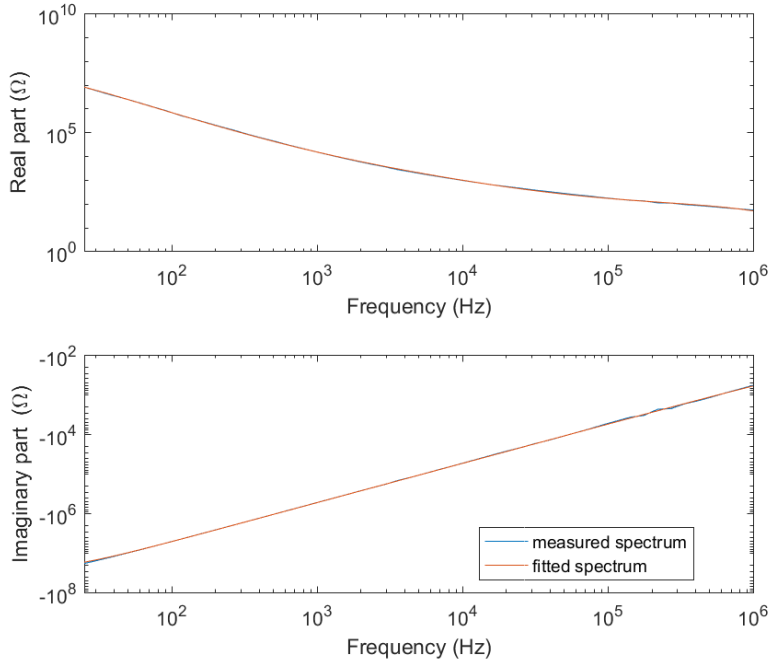

Figure L.6: Last spectrum measured on X60 with offset and PC and the spectrum fitted to it

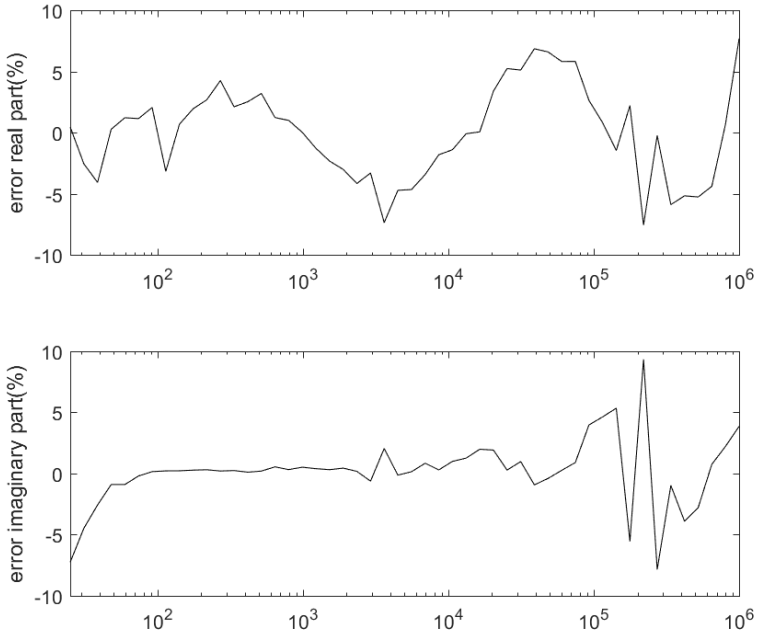

Figure L.7: Error in between the measured and fitted spectrum of X60 with offset and PC

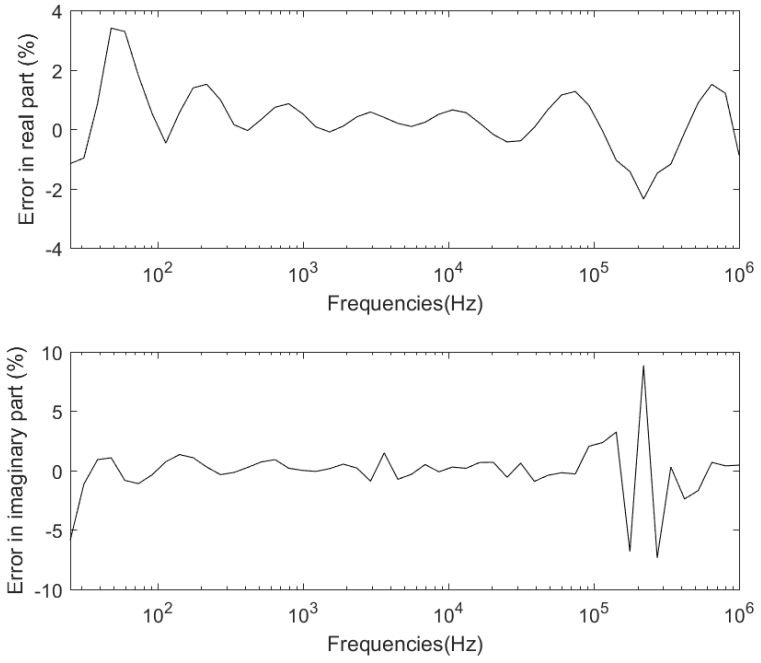

Figure L.8: KKcheck on the last measured spectrum on X60 with offset and PC

L.2 X60 with PC

L.2.1 Impedance Spectroscopy X60 plasticised with PC without DC offset

The spectrum of the X60 sample that has been plasticised using Propylene Carbonate has been measured 10 times. The result of these measurements can be found in figure L.9. The result of the Kronig-Kramer check on the last frequency sweep is shown in Figure L.12.

The parameters resulting from the fit using estimate and boundary conditions as in Table L.8 can be found in Table L.7. The fitted spectrum is plotted together with the measured spectrum in figure L.10, the error between both spectra is plotted in Figure L.11.

The electrode resistance (R1) is not taken into account since it is expected to be very small since steel plates are used. Furthermore the parallel resistance (R4) is not used since no electronic conductance is expected. The geometry independent parameters derived from these determined equivalent circuit elements can be found in table L.9.

Table L.7: Fitted Parameters

Parameter	Physical Meaning	Value	Error
C1	Geometrical capacitance	1.01 nF	1.11%
R2	Ionic resistance	1 kΩ	33.5%
Q	Double layer impedance	$4.35\,\mathrm{n\Omega^{-1}rad^{-n}s^{n}}$	0.0311%
n	Double layer impedance	789 m	2.23%
R3	Resistance due to charge transfer	3.47 kΩ	3.35%
W	Diffusion	$3.28\,\mathrm{k\Omega rad^{-\frac{1}{2}}s^{-\frac{1}{2}}}$	2.98%

Table L.8: Estimates and boundaries

Symbol	Estimate	Lower Boundary	Upper Boundary
C1	1.3 nF	100 pF	2 nF
R2	1 kΩ	1 kΩ	100 MΩ
Q	$3\,\mathrm{\mu\Omega^{-1}rad^{-n}s^{n}}$	$1\,\mathrm{n\Omega^{-1}rad^{-n}s^{n}}$	$1\,\mathrm{m\Omega^{-1}rad^{-n}s^{n}}$
n	800 m	200 m	1
R3	10 kΩ	100 Ω	100 MΩ
W	$2\,\mathrm{k\Omega rad^{-\frac{1}{2}}s^{-\frac{1}{2}}}$	$100\,\mathrm{\Omega rad^{-\frac{1}{2}}s^{-\frac{1}{2}}}$	$100\,\mathrm{M\Omega rad^{-\frac{1}{2}}s^{-\frac{1}{2}}}$

Table L.9: Geometry independent parameters

Symbol	Physical Meaning	Value
ϵ_r	Dielectric Constant	28
σ	Ionic conductivity	$4.05\,\mathrm{m\Omega\,m^{-1}}$
zj_0	Exchange Current density	$7.29\,\mathrm{\mu A\,m^{-2}}$
λ	Debye Length	37.6 µm
I	Ionic strength	$23\,\mathrm{nmol\,m^{-3}}$

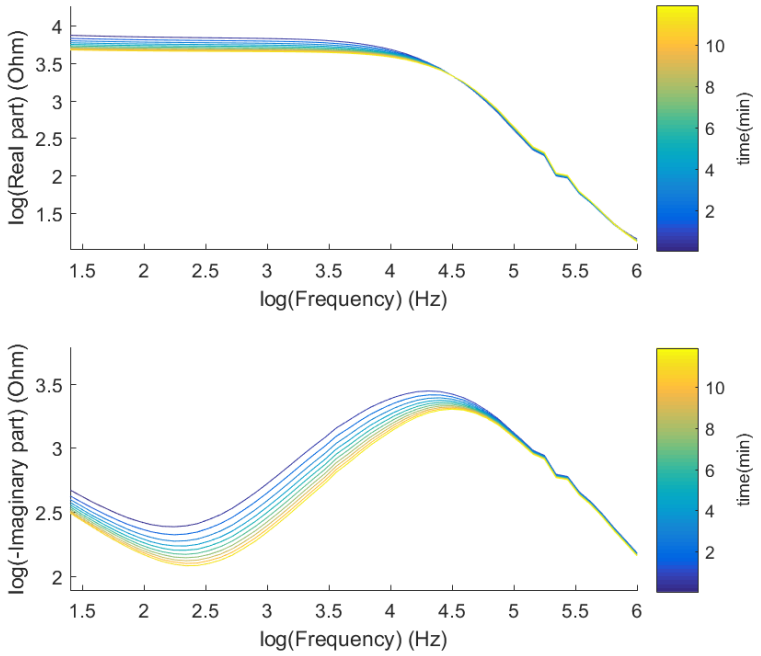

Figure L.9: Drift in the measured spectrum on X60 without offset and PC

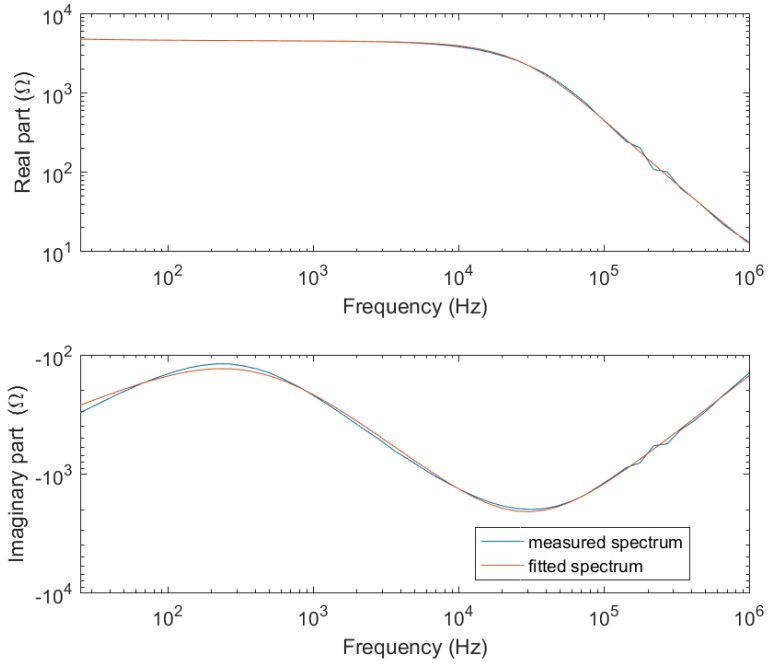

Figure L.10: Last spectrum measured on X60 without offset and PC and the spectrum fitted to it

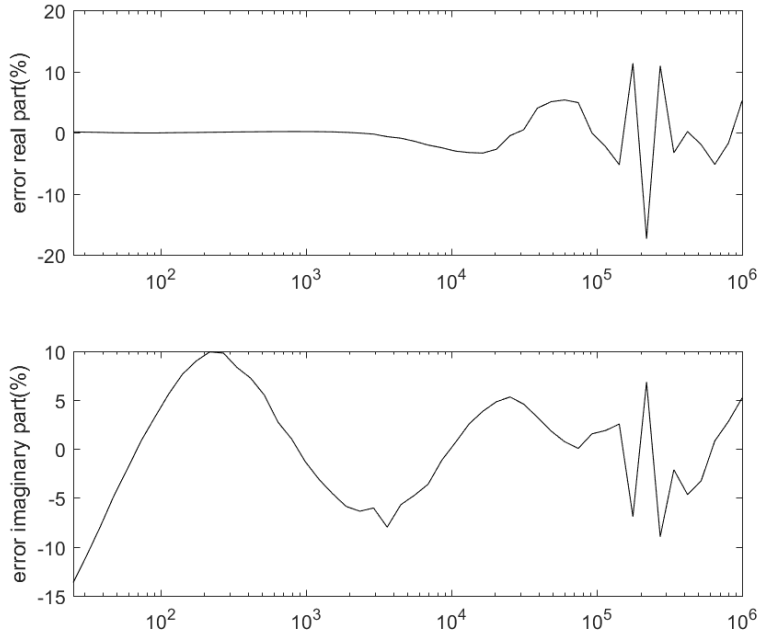

Figure L.11: Error in between the measured and fitted spectrum of X60 without offset and PC

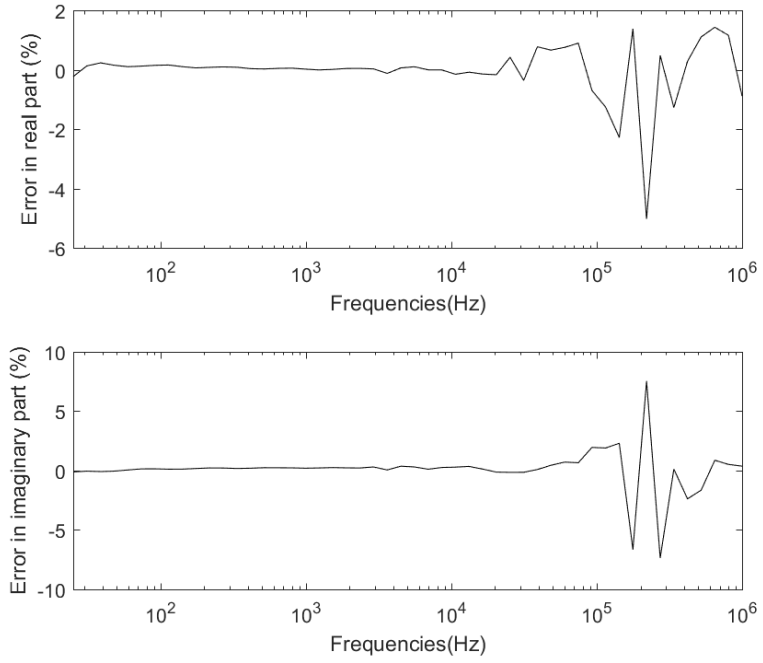

Figure L.12: KKcheck on the last measured spectrum on X60 without offset and PC

L.2.2 Impedance Spectroscopy X60 plasticised with PC with DC offset

The spectrum is also measured in case a DC offset of 10 V is added to the applied signal. The spectrum was measured 20 times, see Figure L.13. The result of the Kronig-Kramer check on the last frequency sweep is shown in Figure L.16.

The parameters resulting from the fit using estimate and boundary conditions as in Table L.11 can be found in Table L.10.The fitted spectrum is plotted together with the measured spectrum in figure L.10, the error between both spectra is plotted in Figure L.11.

Again the electrode resistance (R1) is not taken into account since it is expected to be very small since steel plates are used. Furthermore the parallel resistance (R4) is not used since no electronic conductance is expected. The geometry independent parameters derived from these determined equivalent circuit elements can be found in table L.12

Table L.10: Fitted Parameters

Parameter	Physical Meaning	Value	Error
C1	Geometrical capacitance	1.1 nF	1.5%
R2	Ionic resistance	3.14 kΩ	42.5%
Q	Double layer impedance	$4.05\,\mathrm{n\Omega^{-1}rad^{-n}s^{n}}$	0.0589%
n	Double layer impedance	1×10^{3} m	7.73%
R3	Resistance due to charge transfer	220 kΩ	1.78%
W	Diffusion	$2.18\,\mathrm{M\Omega rad^{-\frac{1}{2}}s^{-\frac{1}{2}}}$	13.4%

Table L.11: Estimates and boundaries

Symbol	Estimate	Lower Boundary	Upper Boundary
C1	1.3 nF	100 pF	2 nF
R2	1 kΩ	1 kΩ	100 MΩ
Q	$3\,\mathrm{\mu\Omega^{-1}rad^{-n}s^{n}}$	$1\,\mathrm{n\Omega^{-1}rad^{-n}s^{n}}$	$1\,\mathrm{m\Omega^{-1}rad^{-n}s^{n}}$
n	800 m	200 m	1
R3	2 MΩ	100 Ω	10 MΩ
W	$2\,\mathrm{M\Omega rad^{-\frac{1}{2}}s^{-\frac{1}{2}}}$	$100\,\mathrm{\Omega rad^{-\frac{1}{2}}s^{-\frac{1}{2}}}$	$10\,\mathrm{M\Omega rad^{-\frac{1}{2}}s^{-\frac{1}{2}}}$

Table L.12: Geometry independent parameters

Symbol	Physical Meaning	Value
ϵ_r	Dielectric Constant	30.6
σ	Ionic conductivity	$1.29\,\mathrm{m\Omega\,m^{-1}}$
zj_0	Exchange Current density	$115\,\mathrm{nA\,m^{-2}}$
λ	Debye Length	136 µm
I	Ionic strength	$1.93\,\mathrm{nmol\,m^{-3}}$

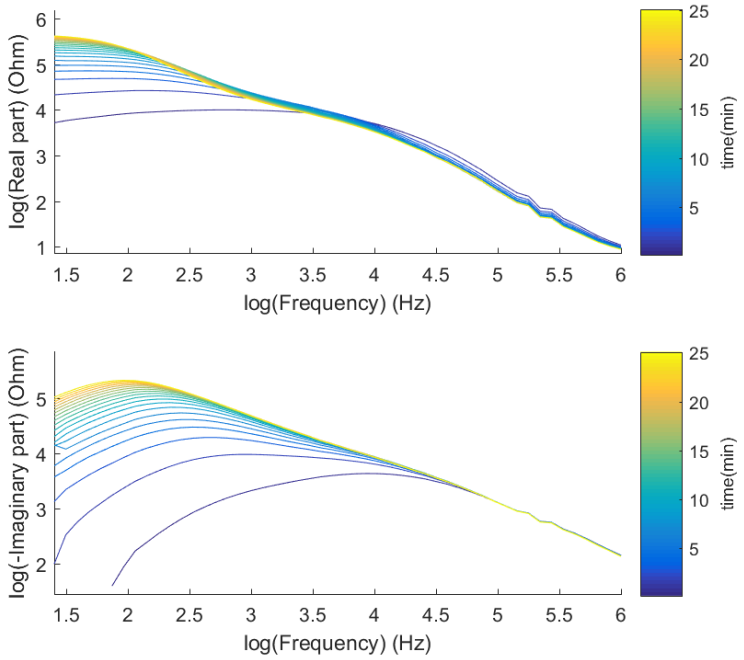

Figure L.13: Drift in the measured spectrum on X60 with offset and without PC

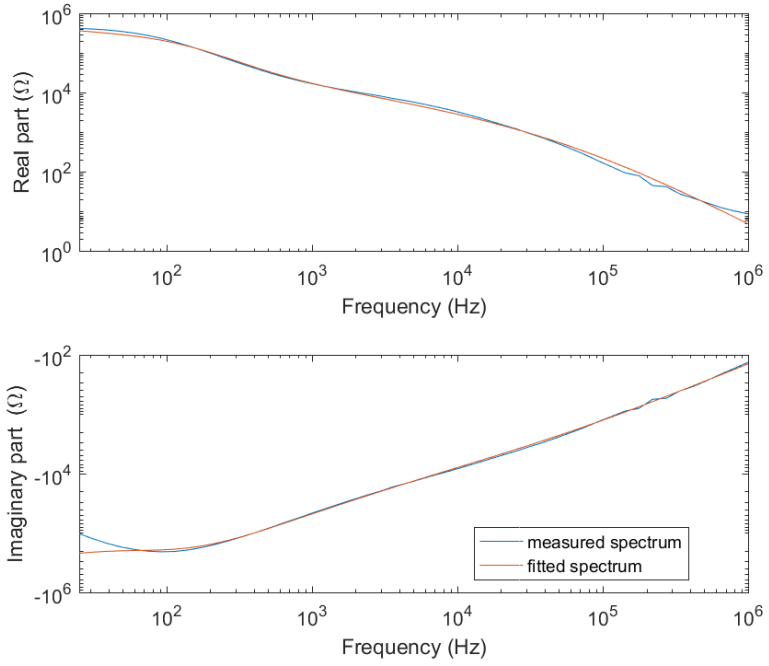

Figure L.14: Last spectrum measured on X60 with offset and PC and the spectrum fitted to it

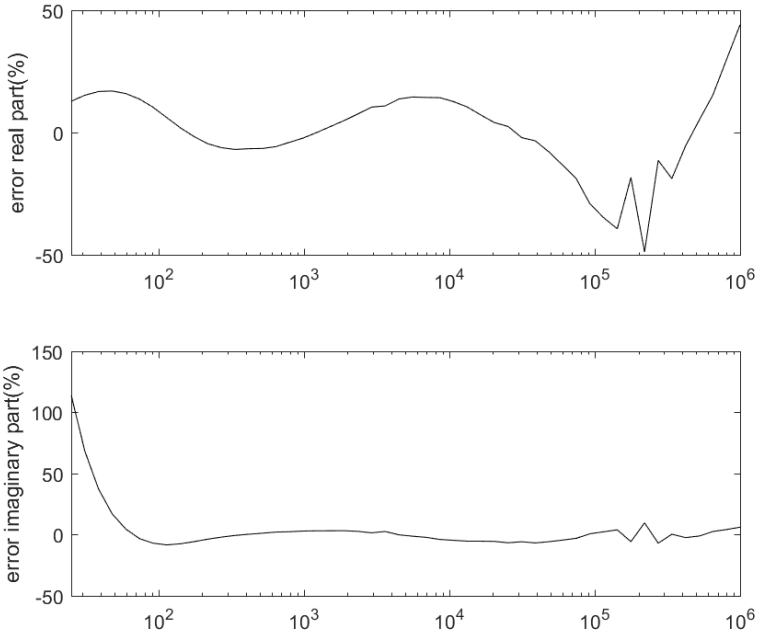

Figure L.15: Error in between the measured and fitted spectrum of X60 with offset and PC

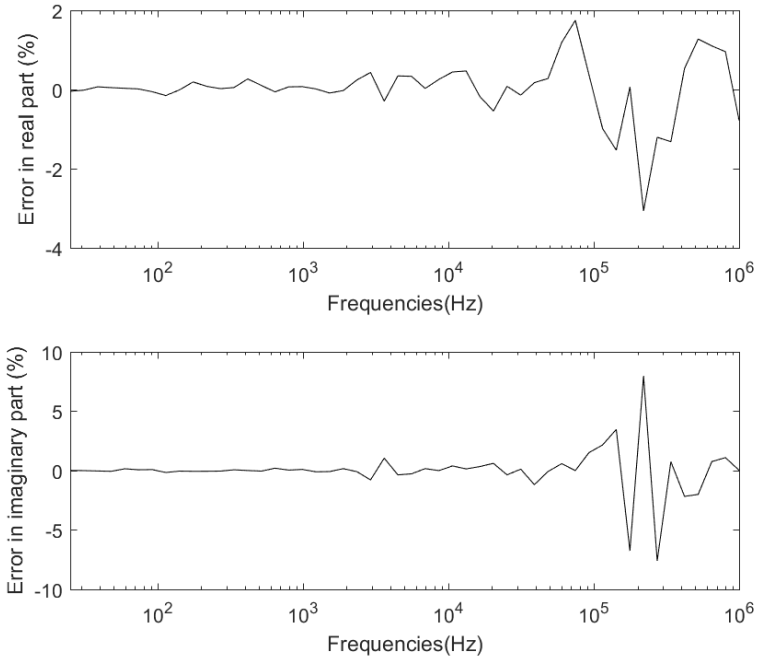

Figure L.16: KKcheck on the last measured spectrum on X60 with offset and PC

L.3 PI-ETPU 85-700+ without PC

L.3.1 Impedance Spectroscopy PI-ETPU 85-700+ without DC offset

The spectrum of the PI-ETPU sample has been measured 10 times. The result of these measurements can be found in figure L.17. The result of the Kronig-Kramer check on the last frequency sweep is shown in Figure L.20.

The parameters resulting from the fit using estimate and boundary conditions as in Table L.14 can be found in Table L.13. The fitted spectrum is plotted together with the measured spectrum in figure L.18, the error between both spectra is plotted in Figure L.19.

The electrode resistance (R1) is not taken into account since it is expected to be very small since steel plates are used. No ionic conductance and therefore also no double layer formation is expected and therefore not taking into account in the model. The geometry independent parameters derived from these determined equivalent circuit elements can be found in table L.15.

Table L.13: Fitted Parameters

Parameter	Physical Meaning	Value	Error
C1	Geometrical capacitance	5.07 nF	7.42%
R4	Electronic resistance	176 Ω	0.744%

Table L.14: Estimates and boundaries

Symbol	Estimate	Lower Boundary	Upper Boundary
C1	5 nF	100 pF	20 nF
R4	1 kΩ	10 Ω	10 kΩ

Table L.15: Geometry independent parameters

Symbol	Physical Meaning	Value
ϵ_r	Dielectric Constant	136
ρ	Electronic resistivity	743 Ω m

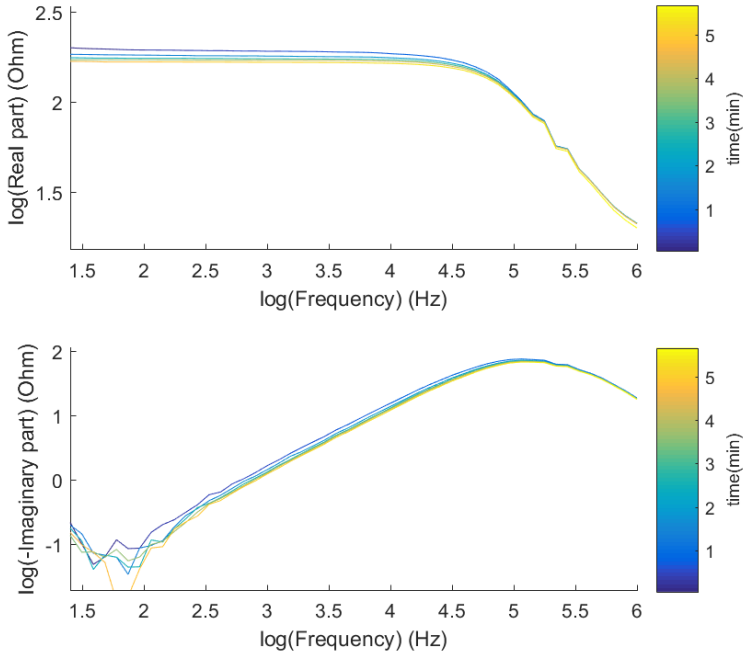

Figure L.17: Drift in the measured spectrum on PI-ETPU 85-700+ without offset and PC

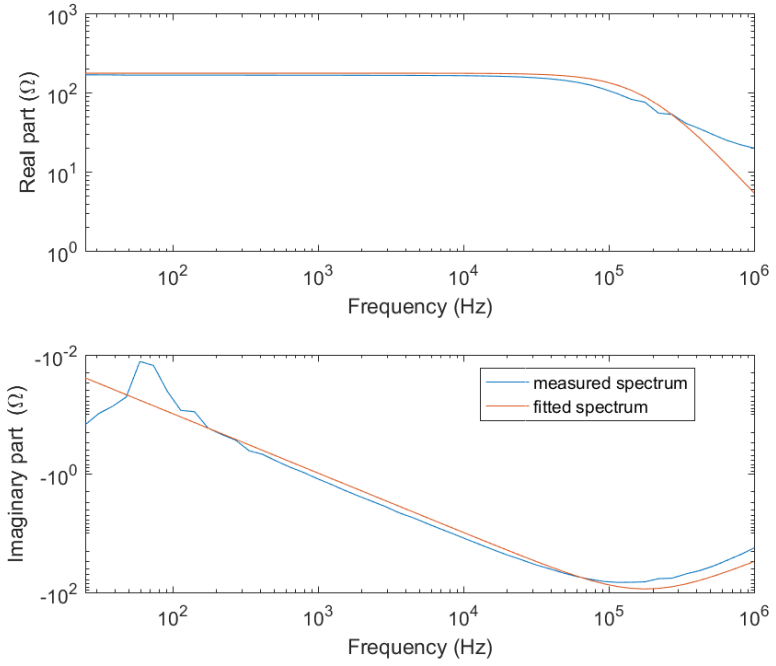

Figure L.18: Last spectrum measured on PI-ETPU 85-700+ without offset and PC and the spectrum fitted to it

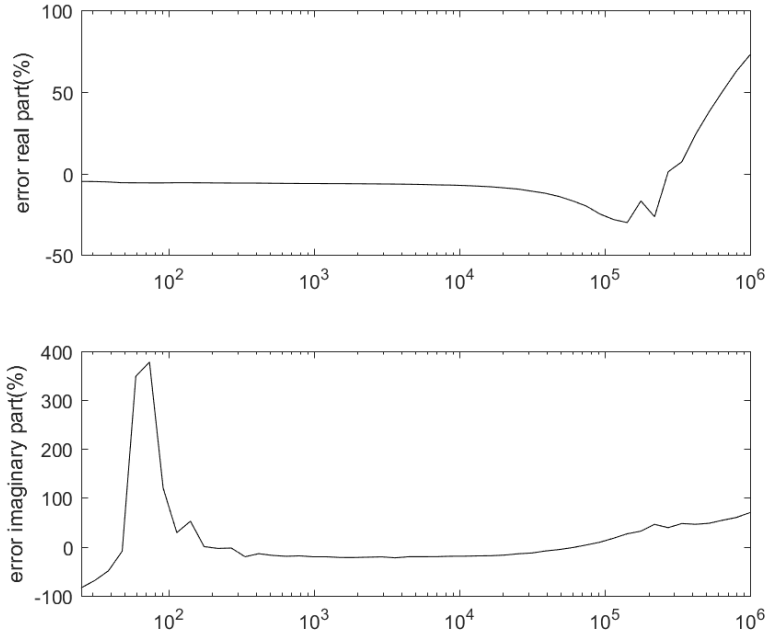

Figure L.19: Error in between the measured and fitted spectrum of PI-ETPU 85-700+ without offset and PC

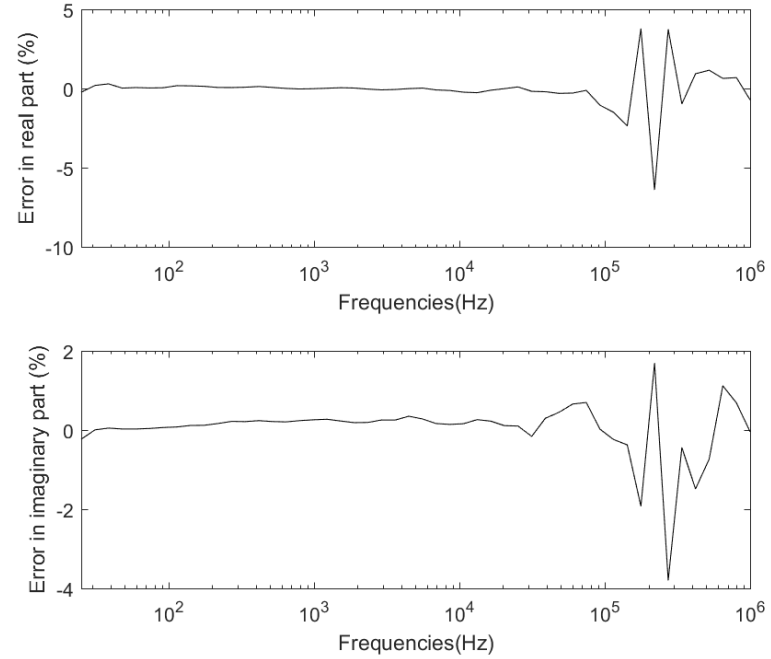

Figure L.20: KKcheck on the last measured spectrum on PI-ETPU 85-700+ without offset and PC

L.4 PI-ETPU 85-700+ with PC

L.4.1 Impedance Spectroscopy PI-ETPU 85-700+ plasticised with PC without DC offset

The spectrum of the PI-ETPU 85-700+ sample that has been plasticised using Propylene Carbonate has been measured 10 times. The result of these measurements can be found in figure L.21. The result of the Kronig-Kramer check on the last frequency sweep is shown in Figure L.24.

The parameters resulting from the fit using estimate and boundary conditions as in Table L.17 can be found in Table L.16. The fitted spectrum is plotted together with the measured spectrum in figure L.22, the error between both spectra is plotted in Figure L.23.

The electrode resistance (R1) is not taken into account since it is expected to be very small since steel plates are used. Furthermore the parallel resistance (R4) is not used since no electronic conductance is expected. The geometry independent parameters derived from these determined equivalent circuit elements can be found in table L.18.

Table L.16: Fitted Parameters

Parameter	Physical Meaning	Value	Error
C1	Geometrical capacitance	977 pF	16.2%
R2	Ionic resistance	69.3 Ω	125%
Q	Double layer impedance	$120\,\mathrm{n\Omega^{-1}rad^{-n}s^{n}}$	1.73%
n	Double layer impedance	576 m	5.03%
R3	Resistance due to charge transfer	26.4 kΩ	4.75%
W	Diffusion	$8.04\,\mathrm{k\Omega rad^{-\frac{1}{2}}s^{-\frac{1}{2}}}$	35%

Table L.17: Estimates and boundaries

Symbol	Estimate	Lower Boundary	Upper Boundary
C1	1.3 nF	100 pF	2 nF
R2	1 kΩ	1 Ω	100 MΩ
Q	$3\,\mathrm{\mu\Omega^{-1}rad^{-n}s^{n}}$	$1\,\mathrm{n\Omega^{-1}rad^{-n}s^{n}}$	$1\,\mathrm{m\Omega^{-1}rad^{-n}s^{n}}$
n	800 m	200 m	1
R3	20 kΩ	100 Ω	100 MΩ
W	$8\,\mathrm{k\Omega rad^{-\frac{1}{2}}s^{-\frac{1}{2}}}$	$100\,\mathrm{\Omega rad^{-\frac{1}{2}}s^{-\frac{1}{2}}}$	$100\,\mathrm{M\Omega rad^{-\frac{1}{2}}s^{-\frac{1}{2}}}$

Table L.18: Geometry independent parameters

Symbol	Physical Meaning	Value
ϵ_r	Dielectric Constant	27.2
σ	Ionic conductivity	$58.5\,\mathrm{m\Omega\,m^{-1}}$
zj_0	Exchange Current density	$958\,\mathrm{nA\,m^{-2}}$
λ	Debye Length	372 nm
I	Ionic strength	$228\,\mathrm{\mu mol\,m^{-3}}$

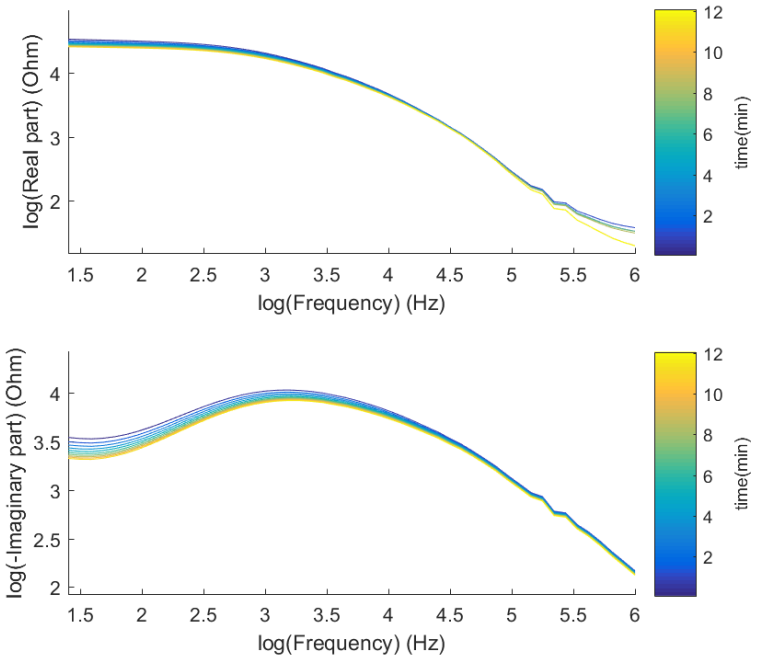

Figure L.21: Drift in the measured spectrum on PI-ETPU 85-700+ without offset and with PC

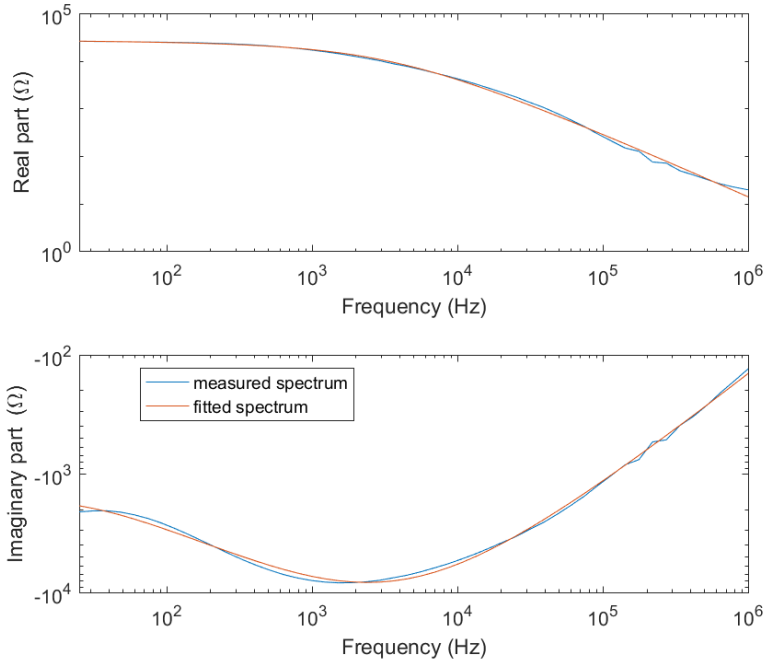

Figure L.22: Measurement on PI-ETPU 85-700+ without offset, with PC and the spectrum fitted to it

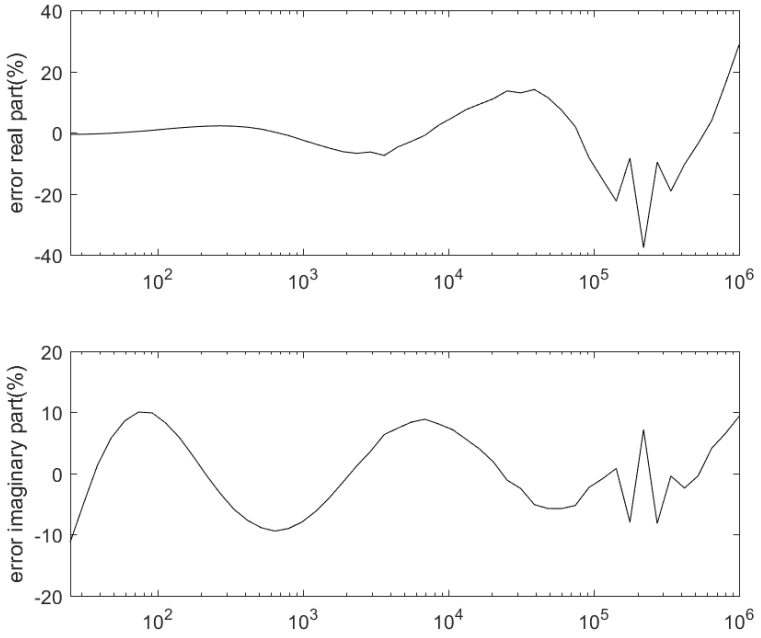

Figure L.23: Error in between the measured and fitted spectrum

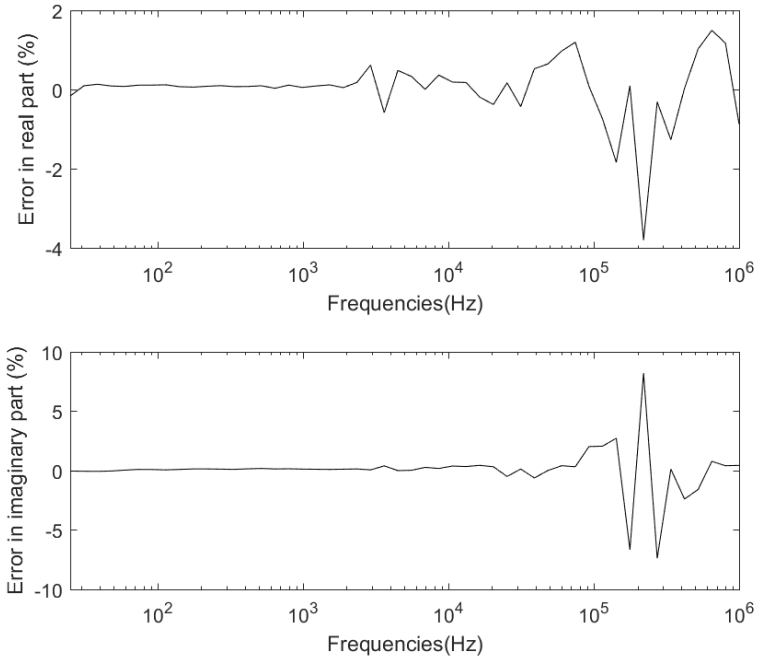

Figure L.24: KKcheck on the last measured spectrum on PI-ETPU 85-700+ without offset and with PC

L.4.2 Impedance Spectroscopy PI-ETPU 85-700+ plasticised with PC with DC offset

The spectrum is also measured in case a DC offset of 10 V is added to the applied signal. The spectrum was measured 20 times, see Figure L.25. The result of the Kronig-Kramer check on the last frequency sweep is shown in Figure L.28.

The parameters resulting from the fit using estimate and boundary conditions as in Table L.20 can be found in Table L.19.The fitted spectrum is plotted together with the measured spectrum in figure L.22, the error between both spectra is plotted in Figure L.23.

Again the electrode resistance (R1) is not taken into account since it is expected to be very small since steel plates are used. Furthermore the parallel resistance (R4) is not used since no electronic conductance is expected. The geometry independent parameters derived from these determined equivalent circuit elements can be found in table L.21

Table L.19: Fitted Parameters

Parameter	Physical Meaning	Value	Error
C1	Geometrical capacitance	1.09 nF	21.6%
R2	Ionic resistance	105 Ω	301%
Q	Double layer impedance	64.3 $n\Omega^{-1}rad^{-n}s^{n}$	167%
n	Double layer impedance	683 m	6.33%
R3	Resistance due to charge transfer	39.2 kΩ	0.0761%
W	Diffusion	1.62 $M\Omega rad^{-\frac{1}{2}}s^{-\frac{1}{2}}$	4.61%

Table L.20: Estimates and boundaries

Symbol	Estimate	Lower Boundary	Upper Boundary
C1	1.3 nF	100 pF	2 nF
R2	1 kΩ	100 mΩ	100 MΩ
Q	30 $n\Omega^{-1}rad^{-n}s^{n}$	1 $n\Omega^{-1}rad^{-n}s^{n}$	10 $\mu\Omega^{-1}rad^{-n}s^{n}$
n	1.5	200 m	1
R3	10 MΩ	10 Ω	20 MΩ
W	2 $M\Omega rad^{-\frac{1}{2}}s^{-\frac{1}{2}}$	10 $\Omega rad^{-\frac{1}{2}}s^{-\frac{1}{2}}$	10 $M\Omega rad^{-\frac{1}{2}}s^{-\frac{1}{2}}$

Table L.21: Geometry independent parameters

Symbol	Physical Meaning	Value
ϵ_r	Dielectric Constant	30.3
σ	Ionic conductivity	38.4 $m\Omega\,m^{-1}$
zj_0	Exchange Current density	645 $nA\,m^{-2}$
λ	Debye Length	1.49 µm
I	Ionic strength	15.8 $\mu mol\,m^{-3}$

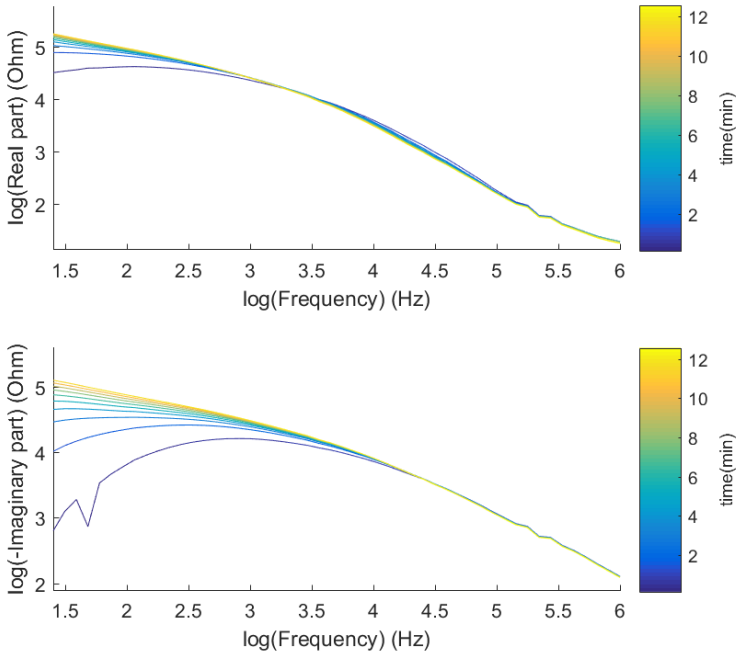

Figure L.25: Drift in the measured spectrum on PI-ETPU 85-700+ with offset and PC

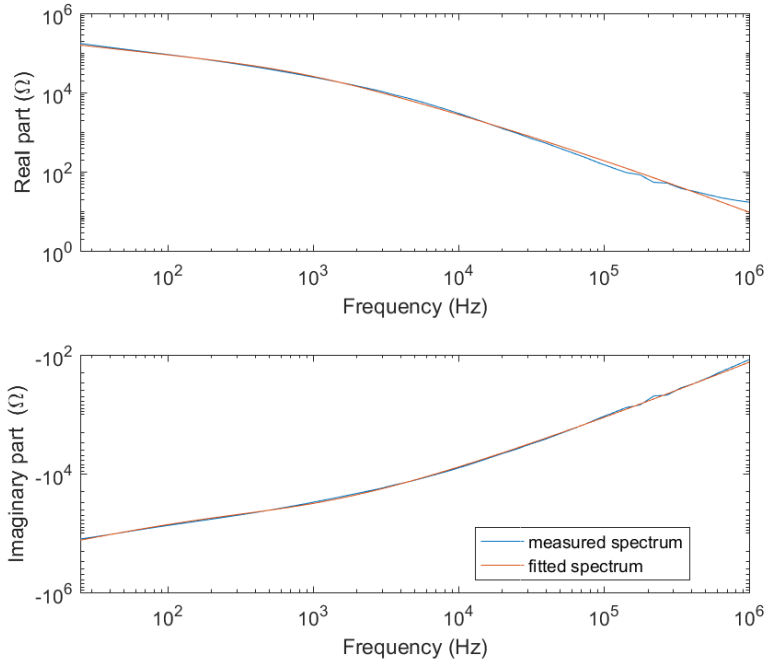

Figure L.26: Last spectrum measured on PI-ETPU 85-700+ with offset and PC and the spectrum fitted to it

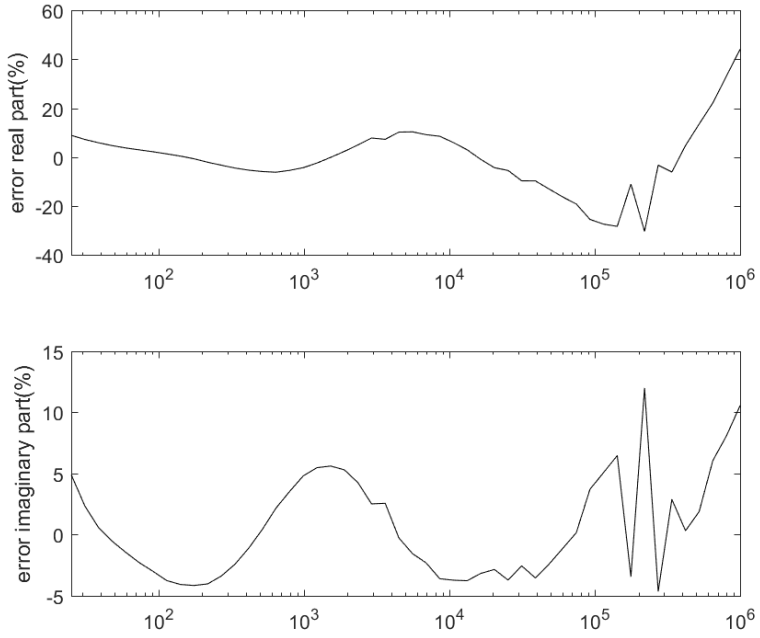

Figure L.27: Error in between the measured and fitted spectrum of PI-ETPU 85-700+ with offset and PC

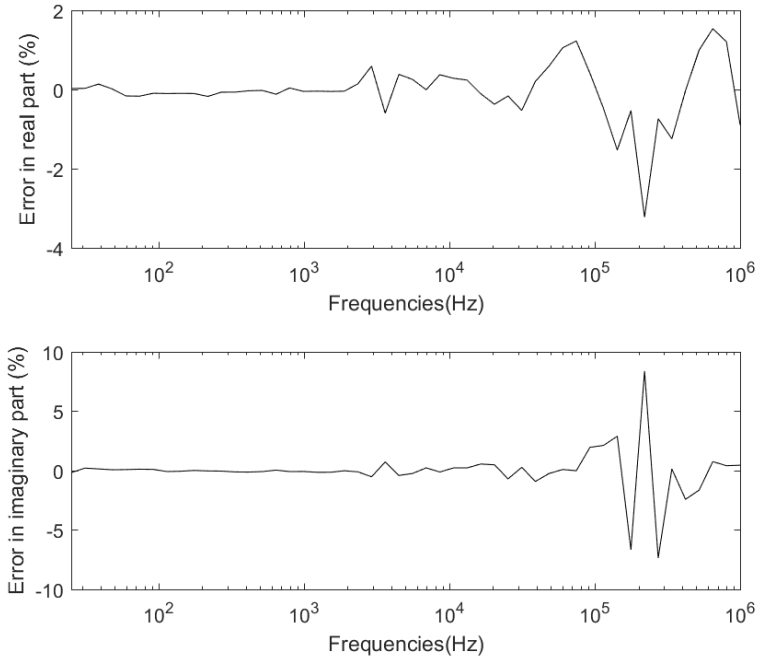

Figure L.28: KKcheck on the last measured spectrum on PI-ETPU 85-700+ with offset and PC

L.5 Ninjaflex without PC

L.5.1 Impedance Spectroscopy Ninjaflex without DC offset

The spectrum of the Ninjaflex sample has been measured 10 times. The result of these measurements can be found in figure L.29. The result of the Kronig-Kramer check on the last frequency sweep is shown in Figure L.32.

The parameters resulting from the fit using estimate and boundary conditions as in Table L.23 can be found in Table L.22. The fitted spectrum is plotted together with the measured spectrum in figure L.30, the error between both spectra is plotted in Figure L.31.

The electrode resistance (R1) is not taken into account since it is expected to be very small since steel plates are used. Furthermore the parallel resistance (R4) is not used since no electronic conductance is expected. The Warburg impedance is left out since it was found to be much smaller than the resistance due to charge transfer. The geometry independent parameters derived from these determined equivalent circuit elements can be found in table L.24.

Table L.22: Fitted Parameters

Parameter	Physical Meaning	Value	Error
C1	Geometrical capacitance	177 pF	1.2%
R2	Ionic resistance	10.7 kΩ	0.103%
Q	Double layer impedance	67.5 $p\Omega^{-1}rad^{-n}s^{n}$	0.000829%
n	Double layer impedance	937 m	0.28%
R3	Resistance due to charge transfer	242 MΩ	145%

Table L.23: Estimates and boundaries

Symbol	Estimate	Lower Boundary	Upper Boundary
C1	200 pF	100 pF	400 pF
R2	1 MΩ	100 Ω	100 MΩ
Q	300 $n\Omega^{-1}rad^{-n}s^{n}$	1 $p\Omega^{-1}rad^{-n}s^{n}$	100 $\mu\Omega^{-1}rad^{-n}s^{n}$
n	800 m	300 m	1
R3	10 MΩ	100 Ω	1 GΩ

Table L.24: Geometry independent parameters

Symbol	Physical Meaning	Value
ϵ_r	Dielectric Constant	4.85
σ	Ionic conductivity	386 $\mu\Omega\,m^{-1}$
zj_0	Exchange Current density	105 $pA\,m^{-2}$
λ	Debye Length	931 µm
I	Ionic strength	6.48 $pmol\,m^{-3}$

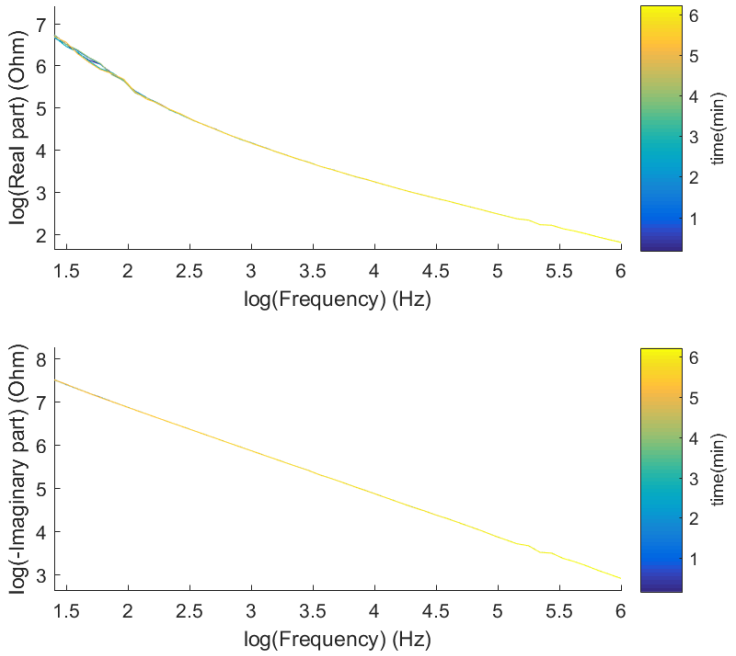

Figure L.29: Drift in the measured spectrum on Ninjaflex without offset and PC

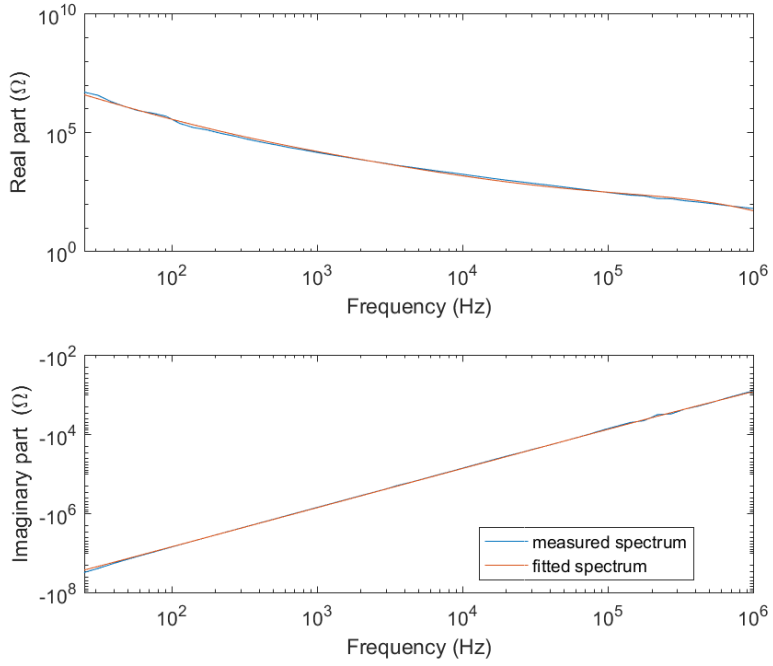

Figure L.30: Last spectrum measured on Ninjaflex without offset and PC and the spectrum fitted to it

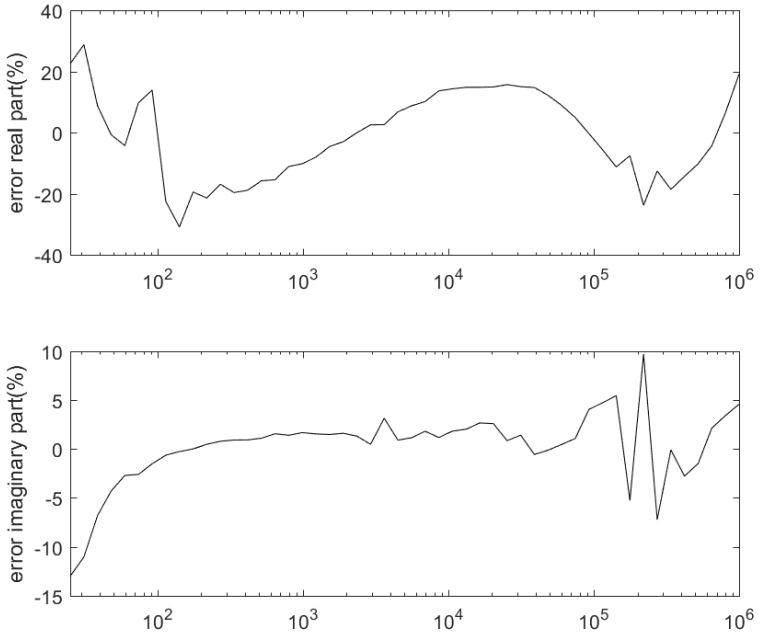

Figure L.31: Error in between the measured and fitted spectrum of Ninjaflex without offset and PC

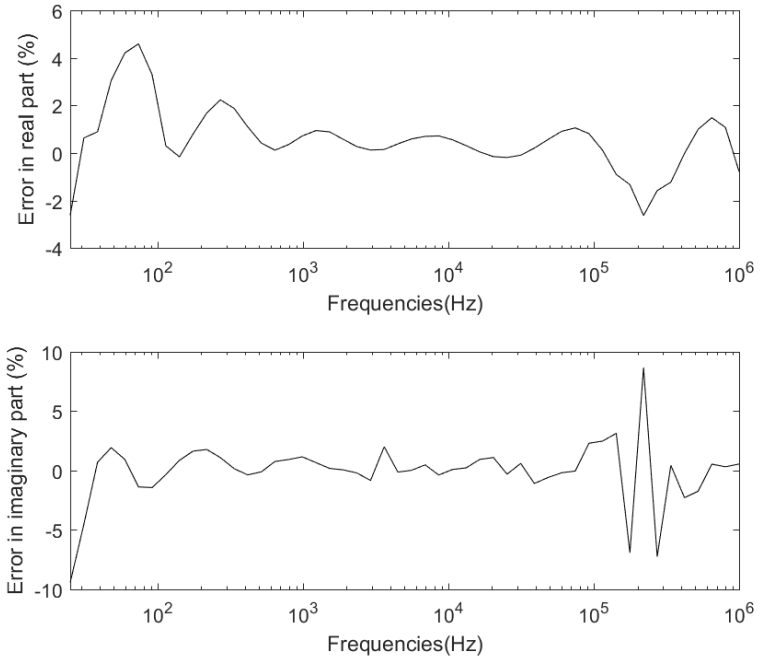

Figure L.32: KKcheck on the last measured spectrum on Ninjaflex without offset and PC

L.6 Ninjaflex with PC

L.6.1 Impedance Spectroscopy Ninjaflex plasticised with PC without DC offset

The spectrum of the Ninjaflex sample that has been plasticised using Propylene Carbonate has been measured 10 times. The result of these measurements can be found in figure L.33. The result of the Kronig-Kramer check on the last frequency sweep is shown in Figure L.36.

The parameters resulting from the fit using estimate and boundary conditions as in Table L.26 can be found in Table L.25. The fitted spectrum is plotted together with the measured spectrum in figure L.34, the error between both spectra is plotted in Figure L.35.

The electrode resistance (R1) is not taken into account since it is expected to be very small since steel plates are used. Furthermore the parallel resistance (R4) is not used since no electronic conductance is expected. The geometry independent parameters derived from these determined equivalent circuit elements can be found in table L.27.

Table L.25: Fitted Parameters

Parameter	Physical Meaning	Value	Error
C1	Geometrical capacitance	608 pF	1.23%
R2	Ionic resistance	1.01 kΩ	53.2%
Q	Double layer impedance	1.1 $n\Omega^{-1}rad^{-n}s^{n}$	0.00493%
n	Double layer impedance	839 m	1.4%
R3	Resistance due to charge transfer	15.8 kΩ	5.31%
W	Diffusion	6.81 $k\Omega rad^{-\frac{1}{2}}s^{-\frac{1}{2}}$	8.36%

Table L.26: Estimates and boundaries

Symbol	Estimate	Lower Boundary	Upper Boundary
C1	1.3 nF	100 pF	2 nF
R2	1 kΩ	1 kΩ	100 MΩ
Q	3 $\mu\Omega^{-1}rad^{-n}s^{n}$	1 $n\Omega^{-1}rad^{-n}s^{n}$	1 $m\Omega^{-1}rad^{-n}s^{n}$
n	800 m	200 m	1
R3	10 kΩ	100 Ω	100 MΩ
W	2 $k\Omega rad^{-\frac{1}{2}}s^{-\frac{1}{2}}$	100 $\Omega rad^{-\frac{1}{2}}s^{-\frac{1}{2}}$	100 $M\Omega rad^{-\frac{1}{2}}s^{-\frac{1}{2}}$

Table L.27: Geometry independent parameters

Symbol	Physical Meaning	Value
ϵ_r	Dielectric Constant	20
σ	Ionic conductivity	3.42 $m\Omega\,m^{-1}$
zj_0	Exchange Current density	1.6 $\mu A\,m^{-2}$
λ	Debye Length	139 µm
I	Ionic strength	1.2 $nmol\,m^{-3}$

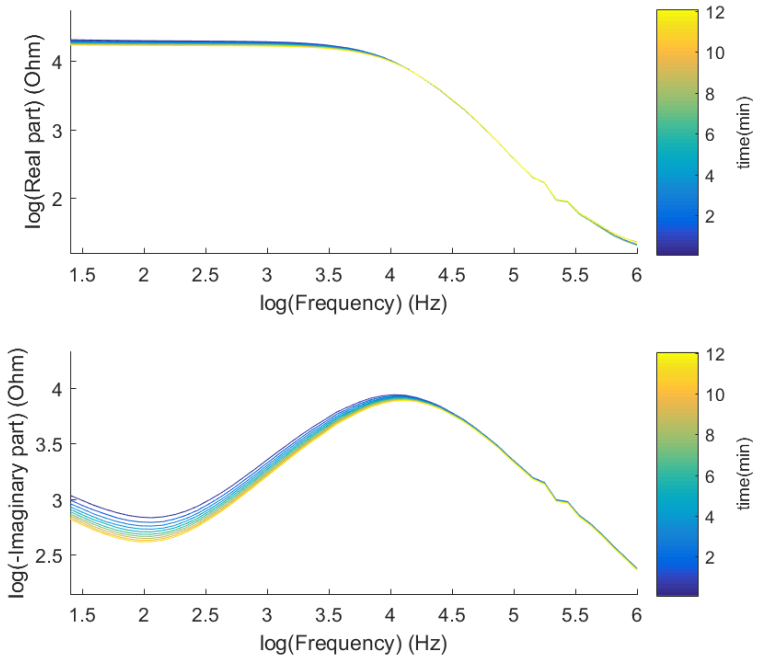

Figure L.33: Drift in the measured spectrum on Ninjaflex without offset and with PC

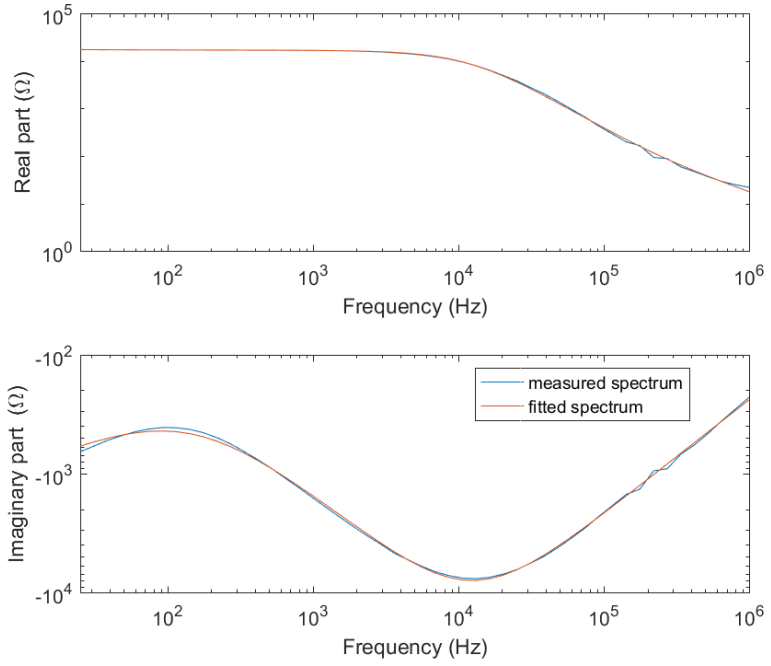

Figure L.34: Last spectrum measured on Ninjaflex without offset and with PC and the spectrum fitted to it

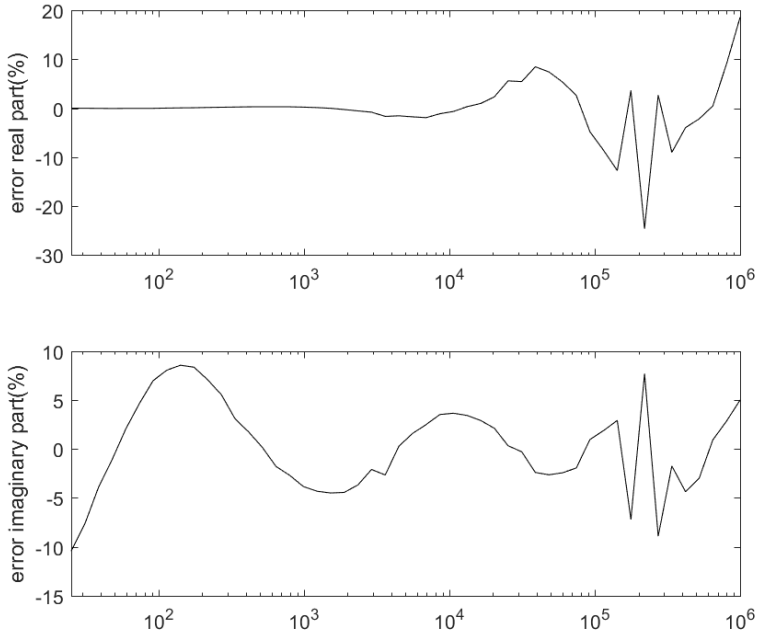

Figure L.35: Error in between the measured and fitted spectrum of Ninjaflex without offset and with PC

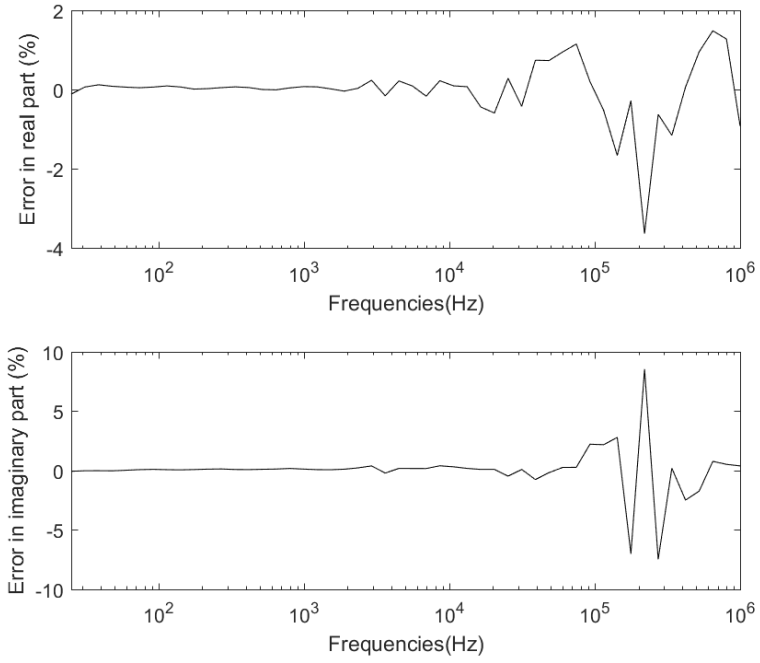

Figure L.36: KKcheck on the last measured spectrum on Ninjaflex without offset and with PC

L.6.2 Impedance Spectroscopy Ninjaflex plasticised with PC and DC offset

The spectrum is also measured in case a DC offset of 10 V is added to the applied signal. The spectrum was measured 20 times, see Figure L.37. The result of the Kronig-Kramer check on the last frequency sweep is shown in Figure L.40.

The parameters resulting from the fit using estimate and boundary conditions as in Table L.29 can be found in Table L.28.The fitted spectrum is plotted together with the measured spectrum in figure L.34, the error between both spectra is plotted in Figure L.35.

Again the electrode resistance (R1) is not taken into account since it is expected to be very small since steel plates are used. Furthermore the parallel resistance (R4) is not used since no electronic conductance is expected. The geometry independent parameters derived from these determined equivalent circuit elements can be found in table L.30

Table L.28: Fitted Parameters

Parameter	Physical Meaning	Value	Error
C1	Geometrical capacitance	642 pF	4.29%
R2	Ionic resistance	340 Ω	347%
Q	Double layer impedance	$25.9\,\mathrm{n\Omega^{-1}rad^{-n}s^{n}}$	0.249%
n	Double layer impedance	600 m	6.8%
R3	Resistance due to charge transfer	1.25 MΩ	35.2%
W	Diffusion	$116\,\Omega\mathrm{rad}^{-\frac{1}{2}}\mathrm{s}^{-\frac{1}{2}}$	130%

Table L.29: Estimates and boundaries

Symbol	Estimate	Lower Boundary	Upper Boundary
C1	1.3 nF	100 pF	2 nF
R2	1 kΩ	100 Ω	100 MΩ
Q	$3\,\mu\mathrm{\Omega^{-1}rad^{-n}s^{n}}$	$1\,\mathrm{n\Omega^{-1}rad^{-n}s^{n}}$	$1\,\mathrm{m\Omega^{-1}rad^{-n}s^{n}}$
n	800 m	200 m	1
R3	2 MΩ	100 Ω	10 MΩ
W	$2\,\mathrm{M\Omega rad}^{-\frac{1}{2}}\mathrm{s}^{-\frac{1}{2}}$	$100\,\Omega\mathrm{rad}^{-\frac{1}{2}}\mathrm{s}^{-\frac{1}{2}}$	$10\,\mathrm{M\Omega rad}^{-\frac{1}{2}}\mathrm{s}^{-\frac{1}{2}}$

Table L.30: Geometry independent parameters

Symbol	Physical Meaning	Value
ϵ_r	Dielectric Constant	21.1
σ	Ionic conductivity	$10.1\,\mathrm{m\Omega\,m^{-1}}$
zj_0	Exchange Current density	$20.2\,\mathrm{nA\,m^{-2}}$
λ	Debye Length	1.56 µm
I	Ionic strength	$10.1\,\mathrm{\mu mol\,m^{-3}}$

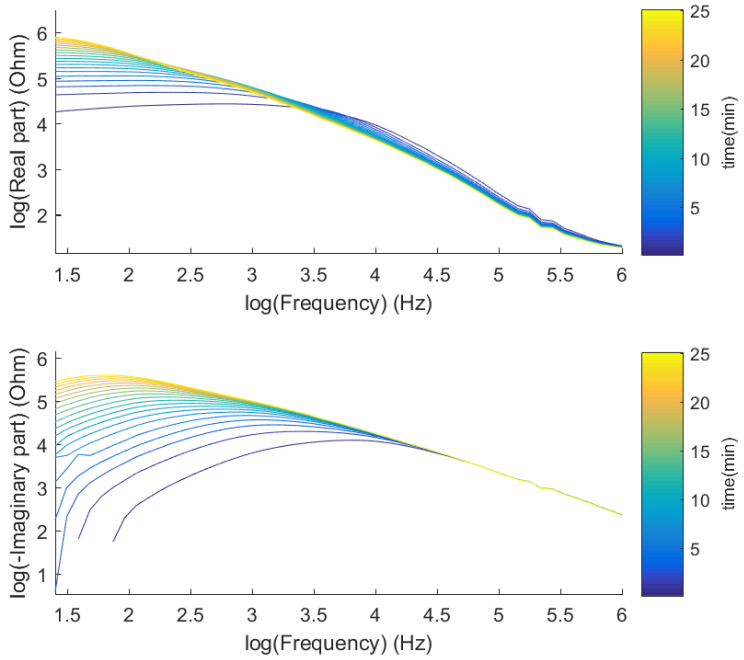

Figure L.37: Drift in the measured spectrum on Ninjaflex with offset and PC

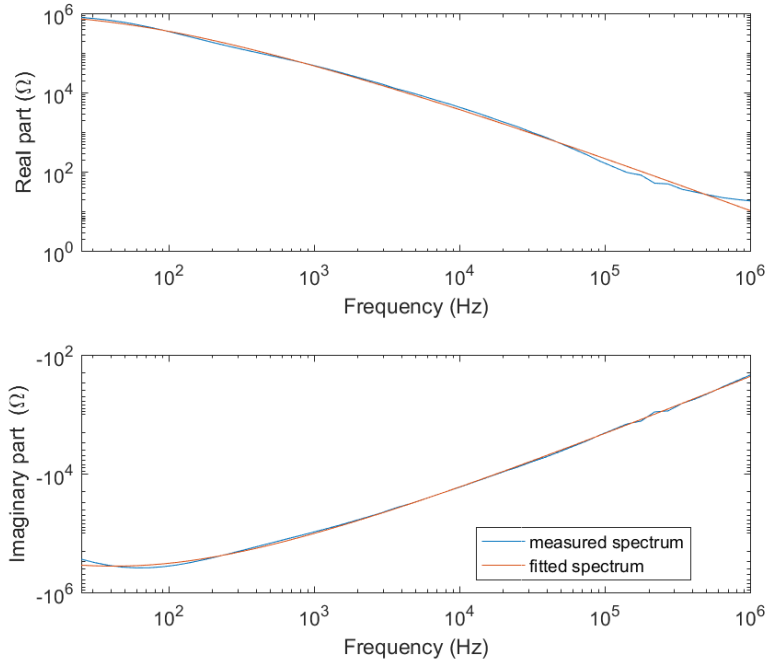

Figure L.38: Last spectrum measured on Ninjaflex with offset and PC and the spectrum fitted to it

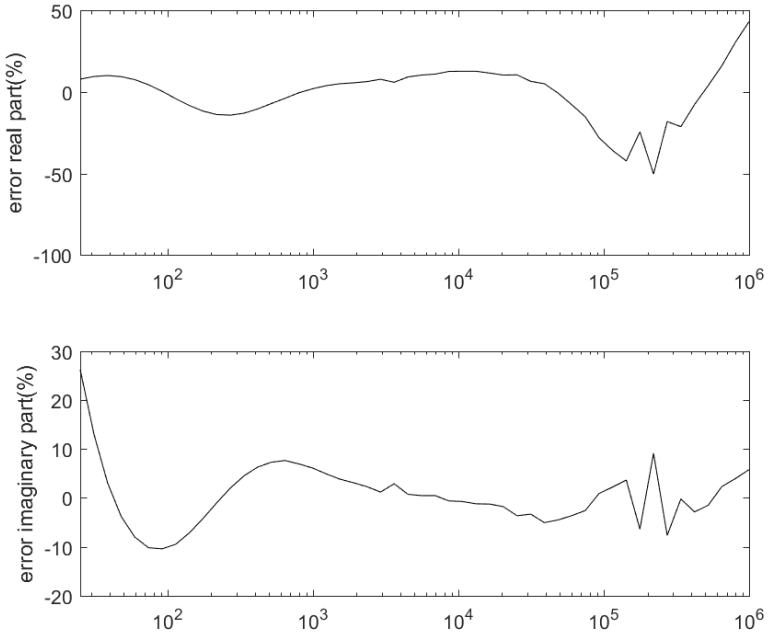

Figure L.39: Error in between the measured and fitted spectrum of Ninjaflex with offset and PC

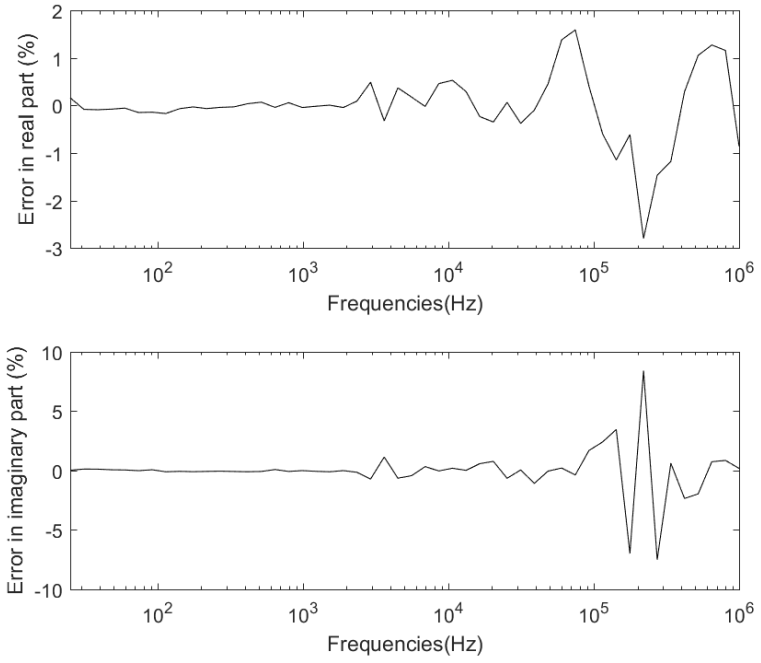

Figure L.40: KKcheck on the last measured spectrum on Ninjaflex with offset and PC